Metabolic and Electrophysiological Effects of Transcranial Photobiomodulation (PBM) and Multi-wavelength PBM

Tyrell Pruitt

Presented to the Faculty of the Graduate School of The University of Texas at Arlington in partial fulfillment

of the requirements for the Degree of

DOCTOR OF PHILOSOPHY

THE UNIVERSITY OF TEXAS AT ARLINGTON

May 2021

Acknowledgment

First, I would like to acknowledge my supervising professor Dr. Hanli Liu who has been constantly supportive and always challenging me to better my work. Without her expert guidance I would not have been nearly as successful in my graduate studies. She takes time out of her life to better teach her students and I hope I can one day be a leader even close to the same caliber.

Second, I would like to thank my committee Dr. Cho, Dr. Maldjian, Dr. Peng, and Dr. Alexandrakis for their time, support, and feedback.

I would also like to thank my parents who have always supported my dreams of becoming a scientist since I was a small boy and have given everything so that I can be in the position I am today. I would also like to thank my wonderful girlfriend Dr. Sara McMahan who has been my rock and provided more loving support than I could ever ask for. My best friend Dr. Nikhil Pandey has always been there for me as well providing more advice and laughs than I could ever list in detail.

During my time in Dr. Liu's lab I have had the great pleasure of working with some truly exceptional people who have always been there for each other. Dr. Wu, Dr. Xinlong Wang, Dr. Parisa Rabbani, Dr. Yudhajit Das, Dr. Olajide Babawale, Akhil Chaudhri, Dr. Nghi Troung, Dr. Liangchieh Ma, and Dr. Elizabeth Urqhart all deserve special mention for helping me along my journey as well as being good friends.

May 12, 2021

Abstract

Metabolic and Electrophysiological Effects of Transcranial Photobiomodulation (PBM) and Multi-wavelength PBM

Tyrell Pruitt

The University of Texas at Arlington, 2021

Supervising Professor: Dr. Hanli Liu

Photobiomodulation (PBM) with near infrared light may become a non-invasive, effective clinical tool after it is understood well for its mechanism of action. In my dissertation research, I have addressed three research questions as three aims to achieve.

Aim 1 was to investigate and demonstrate the reproducibility of the effects of transcranial PBM (tPBM) with 1064-nm laser delivered on the right forehead of separate groups of healthy humans measured using different experiment setups in separate sites and years. In Chapter 2, I reported sham-controlled, tPBM-induced concentration increases in oxygenated hemoglobin (Δ[HbO]) and oxidized cytochrome c oxidase (Δ[oxi-CCO]) in both young and older adults. Specifically, broadband near infrared spectroscopy (bb-NIRS) was utilized to record Δ[HbO] and Δ[oxi-CCO] in 15 young and 5 older healthy subjects before, during, and after 8-

min tPBM. Statistical analysis showed that no significant difference existed in Δ[HbO] and Δ[oxi-CCO] during and post tPBM for the young adults between my current study and a previous one taken three years prior at a different site. The two age groups also showed statistically identical increases in sham-controlled effects of tPBM. In short, this chapter demonstrates the robust reproducibility of tPBM being able to improve cerebral hemodynamics and metabolism of the human brain in vivo in both young and older adults.

In Aim 2, I investigated how 8-min, non-invasive tPBM with 1064-nm laser would modulate cerebral-electrophysiological signals and brain connectivity in the human cortex. In Chapter 3, I proposed a new hypothesis that right prefrontal tPBM enables to increase directional interactions of brain functional networks or so-called information flow (IFlow) mainly at alpha and beta frequencies across cortical regions. Data from 19 healthy humans were analyzed using the Granger-causality approach (i.e., eCONNECTOME, an open-source MATLAB package). With this computational tool, the sham-controlled, tPBM-induced changes in IFlow and respective locations were mapped onto the dipole and cortical space at the group level during and after tPBM. The analysis showed significant increases in IFlow in cortical regions surrounding the stimulation site during the first 4-min and last 3-min tPBM period, when compared to sham. Specifically, at alpha (7-13 Hz) and beta (13-30 Hz) bands, IFlow showed significant increases in the right frontal region near the tPBM site; at delta (0.1-4 Hz) and theta (4-7 Hz) bands, IFlow had significant increases during the first 4-min stimulation; at gamma (30-70 Hz) frequency, IFlow presented significant enhancements during the last 4-min and post stimulation. As for the first time, this study demonstrated that the cortical areas enhanced for their IFlow by right prefrontal tPBM were co-located with

the cortical pathways for learning and memory functions, shedding light on mechanistic association of tPBM-evoked cortical electrophysiological connectivity with improvement of human cognition.

Aim 3 was to investigate the tPBM-induced effects by different wavelengths, namely, at 1064, 852, and 808 nm for better reviewing and interpreting essential mechanisms of action involved in wavelength-dependent tPBM. Specifically, sham-controlled PBM effects with 1064-, 852-, 808-nm laser were measured from the forearm of 10 healthy adults using bb-NIRS with 2-min baseline, 8-min PBM, and 5-min recovery. After repeated measures ANOVA, compared to the responses under sham, while 1064-nm PBM showed consistent increases of Δ[HbO] and Δ[oxi-CCO], 852-nm PBM resulted in enhancement of Δ[HbO], Δ[HbT] but not Δ[oxi-CCO] and 808-nm PBM caused a delayed increase in only Δ[oxi-CCO]. Indeed, the newly-collected, hemodynamic and metabolic changes induced by PBM at these wavelengths are the first objective report in the field, providing the observation that cannot be well explained by the conventional PBM theory. To interpret the experimental results, accordingly, I proposed or hypothesized three semi-novel pathways by considering both CCO-oxidized and heat-regulated pathways concurrently activated by light. Given the limited number of human subjects, further investigation and validation for this model are needed and will be our future work.

Furthermore, it would be very beneficial if there exists a theoretical model that allows us to relate the PBM power or outcome with (1) optical properties of tissue, (2) light penetration

depth, (3) power density of light, and (4) aperture size of the light. In Chapter 5, we developed an analytical expression of light fluence as a function of such parameters based on diffusion theory, followed by laboratory validation using liquid tissue phantoms. Specifically, a tank of the 4-liter liquid phantom was made of an intralipid solution and black ink or horse blood. Fluence measurements were taken with variable laser power densities and aperture sizes. The analytical solution of fluence showed excellence to match the experimental observations using different power density and aperture size of the 1064-nm laser. We concluded that an analytical equation was successfully confirmed for its accuracy to predict, estimate or quantify optical fluence within tissue treated by PBM.

Chapter 0 Table of Contents

Table of Figures

Chapter 1 : Introduction

1.1 Significance and Background

tPBM study has been a topic of increasing interest in the neuromodulation community for some time, however the cellular and neuronal mechanisms behind tPBM's action are still largely unknown(de Freitas and Hamblin 2016) (Karu 2010) (Hamblin 2017) (Hamblin 2018) (Santana-Blank, Rodríguez-Santana et al. 2015). Bb-NIRS is a new and novel method of monitoring these mechanistic changes *in vivo* rather than in the petri dish. Recent advances in the field have allowed researchers to measure intracellular Cytochrome C Oxidase (CCO) oxidation in addition to oxygenated hemoglobin (HbO) and deoxygenated hemoglobin (Hb) using bb-NIRS technology (Wang, Tian et al. 2016) (Wang, Reddy et al. 2017) (Wang, Tian et al. 2017) (Bale, Mitra et al. 2016). This allows an indirect measurement of cellular respiration though CCO oxidation which can be equated to cellular energy production in the form of ATP. (Karu 2010) (Wong-Riley, Liang et al. 2005) (Lim, Sanders et al. 2008) What these cellular effects do to the nervous tissue of the brain as a whole has been measured using EEG to determine areas of altered electrical signaling in the cortex during tPBM stimulation. (Wang, Dmochowski et al. 2019) (Wang, Dmochowski et al. 2019) (Hamblin 2016) However, these signals are often very complex and power increases are often not seen in the areas expected like near the site of stimulation. In order to adequately perceive what is happening to the

brain during tPBM advanced algorithms such as Granger Causality are utilized to make previously unseen connections within the brain apparent during tPBM (Hesse, Möller et al. 2003) (Gow Jr, Segawa et al. 2008) (Nicolaou, Hourris et al. 2012) (Blinowska, Kuś et al. 2004) .

Although the existence and physical effects of tPBM are generally agreed upon, the chromophore related results published in our first paper were never replicated in vivo. The imaging of CCO via bb-NIRS is a well-tested methodology [(Hull, Nichols et al. 1998) (Bainbridge, Tachtsidis et al. 2014)], but at the time this study was conducted there was only one paper published using bb-NIRS to quantify chromophore changes induced by transcranial photobiomodulation by this lab's previous research article [(Wang, Tian et al. 2017)]. With nothing to compare this landmark paper to, the validity of the results would be suspected without further experimental replication. My Aim 1 not only replicated the results finding no significant differences between past and present conclusions, but also found that the results were consistent between old and young age groups. The findings of this study confirm that not only are the chromophore concentration changes by tPBM measurable across the general population regardless of age group, but that the effects are significantly consistent even when using a different spectrometer, experimental personnel, study population, etc.

1.2 Advanced processing algorithms for tPBM-EEG datasets

tPBM's effect on alpha and beta band power has been documented in previous publications, but the location of the power increases and their distance from the site of stimulation posed even more questions on how the stimulation led to power increases in these areas(Zomorrodi, Saltmarche et al. 2017) (Zomorrodi, Loheswaran et al. 2019) (Jahan, Nazari et al. 2019) (Zomorrodi, Loheswaran et al. 2019). To determine the areas of the brain communicating with one another and their function withing the brain during tPBM this study utilized an autoregressive model known as Granger causality to better determine connectivity from these EEG datasets(Kong, Lin et al. 2015) (De Tommaso, Stramaglia et al. 2013) (Tang, Sutherland et al. 2007). Granger causality also allows directionality to be applied to these connectivity values to determine if these connections are one-way or two-way phenomenon (Hesse, Möller et al. 2003) (Blinowska, Kuś et al. 2004) (Gow Jr, Keller et al. 2009).

1.3 Understanding the metabolic effects of PBM at multiple wavelengths

The current body of PBM studies includes a variety of different wavelengths of light used to induce PBM's effects. This lab focuses on 1064 nm PBM due to its hypothesized high penetration depth compared to other wavelengths, but 808

(Amaroli, Parker et al. 2015) (Amaroli, Ravera et al. 2016) (de Andrade, Bossini et al. 2017) (Amaroli, Ravera et al. 2019) and 850 nm (Kau, Kantarci et al. 2013) (Tatmatsu-Rocha, Tim et al. 2018) wavelengths are commonly used in the field as well due to their absorption properties in relation to CCO. To better understand the fluence properties of these wavelengths as they travel deeper into the body this study utilized *in vivo* measurement methods.

1.4 Specific Aims and Dissertation Outline

Although transcranial photobiomodulation (tPBM) is a widely published phenomenon with many qualitative studies performed on its mental impact, there are relatively few in depth mechanistic studies to determine the source of these effects. Also, tissue and cellular function can be indirectly assessed by oxy-hemoglobin (HbO), deoxy-hemoglobin (Hb), and cytochrome c oxidase (CCO) as the rate of oxygen consumption and ATP production are intrinsically linked to cellular activity. A recent pilot study with a small sample size has shown that tPBM is able to positively increase HbO and CCO activity, but if this effect is not consistent for the general population, then the usefulness of the tPBM stimulation for treatment in the future would be largely limited. Therefore, measuring the effects of tPBM quantitatively across a large population size and multiple demographics is necessary to prove the effectiveness of tPBM in a clinical setting in the future.

So, **the first aim of my dissertation** is to examine how measurement locations, times, and setups would affect the reliability and reproducibility of tPBM-induced changes in HbO, Hb, and CCO. The hypothesis is that changes in HbO, HHb, and CCO by tPBM will be consistent between measurement locations/conditions and between age groups.

Though broadband near infrared spectroscopy can accurately measure changes in blood oxygenation and cellular respiration, it cannot detect changes in neural activity on a macro level *in vivo.* Electroencephalography (EEG) is a powerful tool in performing this task as it can measure the electrical activity of the brain on a cortical level during tPBM. However, analyzing the brain oscillation powers of these signals can only convey changes in the neural network as a whole. By analyzing these signals using predictive models an inference can be made on the flow of information through the various functional regions of the brain. One such predictive model is Granger causality, which is a robust autoregressive model originally used to predict economic outcomes. As **my second aim**, I apply this model to tPBM EEG data and generate a reliable estimate of changes in information flow on the cortical level during light stimulation. My hypothesis is that tPBM significantly alter the flow of neural electrical information across the large-scale human scalp when compared to placebo.

In recent mechanistic studies, 1064-nm laser stimulation was used due to its previous success of improving human cognition. However, many other wavelengths of light are used in tPBM with little understanding of the mechanistic difference among them *in vivo*. **My third aim** is to examine and compare PBM-induced effects in HbO, HHb, and CCO with 808, 852, and 1064 nm lasers performed on the human arm. Valuable inferences can be obtained to determine the most effective wavelength for PBM, which would be practically useful to guide future clinical applications of tPBM. Also, light propagation parameters within tissue are calculated using a theoretical model and validated with experiments of liquid tissue phantoms.

Aim 1: Quantify and demonstrate the reliability and consistency of tPBM-induced effects in the human brain

1(a): To determine the reproducibility of tPBM-induced effects on 2 separate groups of young human subjects measured in separate sites and times with different equipment and settings.

1(b): To detect differences, if any, in tPBM-induced effects on young individuals vs. older (55+) individuals.

Aim 2: Determine information flow changes due to tPBM on large-scale human brain circuitry at the cortical level using Granger causality EEG analysis

2(a): To display the effectiveness of Granger causality on analyzing consistent EEG trends under tPBM vs. sham conditions

2(b): To determine the differences in information flow caused by sham-controlled tPBM in the human brain.

2(c): To determine relevance of the functional regions of the human brain connected during tPBM vs. sham.

Aim 3: Compare PBM-induced physiological changes caused by 808, 852, and 1064 nm lasers in the human arm measured in vivo

3(a): To perform PBM experiments from human forearms (n=15) using all three 808, 852, and 1064 nm lasers and quantify respective changes of HbO, HHb, and CCO;

3(b): To determine if the physiological effects by three wavelengths differ statistically from one another and to better understand the underlying cellular mechanisms

responsible for their action.

3(c): To quantify light propagation in tissue by developing a theoretical model and validating it with ex vivo experiments using liquid tissue phantoms. The quantified parameters for 1064-nm laser include light penetration depth, fluence at various depths, and radial fluence from the center of the beam.

Chapter 2 : Transcranial photobiomodulation (tPBM) with 1064-nm laser to improve cerebral metabolism of the human brain in vivo

Tyrell Pruitt, Xinlong Wang, Anqi Wu, Elisa Kallioniemi, Mustafa M. Husain, and Hanli Liu

(This chapter is a manuscript that was published in *Lasers in Surgery and Medicine*)

2.1 Introduction

Transcranial photobiomodulation (tPBM) is a non-invasive and non-thermal approach that uses low-power light at a near infrared (NIR) wavelength between 620-1100 nm to accelerate cellular functions in the human brain/tissue for cognitive benefits of normal aging (Rojas and Gonzalez-Lima 2011, Barrett and

Gonzalez-Lima 2013, Blanco, Maddox et al. 2017) and/or for clinical treatments of brain disorders and injuries (Cassano, Petrie et al. 2016, Hamblin 2016, Naeser, Martin et al. 2016, Naeser, Ho et al. 2019). The mechanism of tPBM is based on the photo-oxidation of cytochrome c oxidase (CCO), the terminal enzyme in the electron transport chain, which catalyzes the oxygen metabolism for cellular ATP production (Gonzalez-Lima, Valla et al. 1998, Rojas and Gonzalez-Lima 2011, De Freitas and Hamblin 2016). Specifically, the NIR light can convert reduced-state CCO into its oxidized state, as labeled "oxi-CCO" hereafter. Oxi-CCO is active in a series of redox reactions, reducing oxygen molecules into water and enhancing the proton gradient at the inner membrane of mitochondria. This photo-oxidation process of CCO accelerates the utilization of oxygen within mitochondria and the production of intracellular ATP (Rojas and Gonzalez-Lima 2011, Gonzalez-Lima, Barksdale et al. 2014). Accordingly, cells and neurons that have a high concentration of mitochondria will be facilitated to be more active in their mitochondrial oxygen metabolism and thus their functional activities, leading to enhancement of synaptic connections (Khakh, Gittermann et al. 2003, Kawauchi, Sato et al. 2008, Huang, Gupta et al. 2012).

Recently, this tPBM mechanism of action was supported by objective measures of tPBM-induced increases in concentrations of cerebral oxygenation and oxi-CCO in the human brain using non-invasive broadband near-infrared spectroscopy (bb-NIRS) by our group (Wang, Tian et al. 2017). While the results reported in the study were highly statistically significant, it was the only published report showing effects of tPBM on hemodynamic and metabolic upregulation in the human brain measured by bb-NIRS *in vivo*, with a small group of 11 young subjects. It is important to demonstrate the robust reproducibility for the findings to develop tPBM as a non-invasive neuromodulation tool for cognitive benefits in healthy adult and aging population as well as patients with neurological or psychiatric disorders.

In this study, we aimed to investigate (1) the validity of previous findings in Ref. (Wang, Tian et al. 2017) in two different subsets of young subjects at two study sites over a period of 3 years, and (2) age-related effects of tPBM by comparing sham-controlled increases of Δ[HbO] and Δ[oxi-CCO] between young and older adults. In this study, the same bb-NIRS experimental setup, protocol, and procedures were performed on a group of young (n=15) and older (n=5) participants, but with different experimental operators at a different experimental site with respect to the previous study. Student t-tests was used to assess the reproducibility of the findings between the two sets of young adults

and between the two age groups. The results indicated high reproducibility of tPBM effects detected by bb-NIRS in the young-adult groups. For the older adults, the sham-controlled increases in Δ[HbO] and Δ[oxi-CCO] were identical in both age groups. These results indicate great potential of neuroplastic effects of tPBM in future applications.

2.2 Methods

2.2.1 Participants

20 healthy normal subjects (11 females and 9 males) were recruited from University of Texas Southwestern Medical Center at Dallas (UTSW), the Southern Methodist University (SMU), and the University of Texas at Arlington (UTA). For this study, the actual measurements took place at the UTSW campus. There were 15 adults (7 females and 8 males; age=26.7±2.7 years) in the young-adult group (younger than 60 years) and 5 (4 females and 1 male; age=68.2±4.8 years) in the older-adult (older than 60 years) group. The inclusion/exclusion criteria were the same as those in Wang et al. (Wang, Tian et al. 2016). All subjects had no prior diagnosis or history of neurological conditions and were instructed to keep caffeine and nicotine consumption to a minimum (a cup) prior to the experiment. The study protocol was reviewed and approved by the Institutional

Review Board (IRB) of both UTA and UTSW as well as complied with all applicable federal and NIH guidelines. Written informed consent was obtained from each participant prior to the experiments. All the participants were asked to come back on two non-consecutive days to undergo either sham or tPBM in a randomized order. Data from 11 young participants (5 females and 6 males; age= 31.0±13.7 years) recruited in the previous study were also used for examining the reproducibility of tPBM effects on cerebral metabolism and hemodynamics of the human brain in vivo (Wang, Tian et al. 2017). There was no overlap between the participants in the two studies.

2.2.2 Experiments

2.2.2.1 1064-nm tPBM

Both tPBM and sham experiments were administered using the same continuous-wave 1064-nm laser (Cell Gen Therapeutics LLC, Dallas, TX; Model CG-5000) with respect to the previous study (Wang, Tian et al. 2017). It is FDA-cleared for pain relief, such as muscle, nerve, and joint pain. The laser device was set to a calibrated power of 3.5 W to deliver tPBM on each participant's forehead and was set to a minimum operating power of 0.1 W for the sham experiments. During the sham experiments, the laser aperture was blocked by

a thick black tape to prevent 1064-nm light from reaching the participant's forehead. Both tPBM and sham experiments were conducted through a hand-held aperture at 2 cm away from the forehead scalp/skin without any physical contact, following the common suggested procedure (Barrett and Gonzalez-Lima 2013). Light from the aperture was well collimated and the illumination area on the human brain was 13.6 cm^2, giving rise to a constant power density of 3.4 W/13.6 cm^2 = 0.25 W/cm^2.

2.2.2.2 bb-NIRS

The same bb-NIRS system was utilized as in our previous report (Wang, Tian et al. 2017). Briefly, this system consists of a tungsten halogen lamp (Model 3900, Illumination Technologies Inc., East Syracuse, NY) as the broadband light source (covering 400-1500 nm light) and a back-thinned cool-down CCD spectrometer (QE-Pro, Ocean Optics Inc.) as the detector. The white light emitted from the light source was delivered on to the human forehead through a fiber optic bundle (see Fig. 1). A portion of the light diffused through the human brain was collected by another fiber bundle 3 cm away from the source bundle, latter of which directed the detected light into the CCD spectrometer. Time dependent spectral (740–900 nm) intensities before, during, and after tPBM or sham

delivery were recorded and used to quantify concentration changes of oxygenated hemoglobin (Δ[HbO]) and oxidized cytochrome c oxidase Δ[oxi-CCO] based on the modified Beer-Lambert law, as described in Ref. (Wang, Tian et al. 2016).

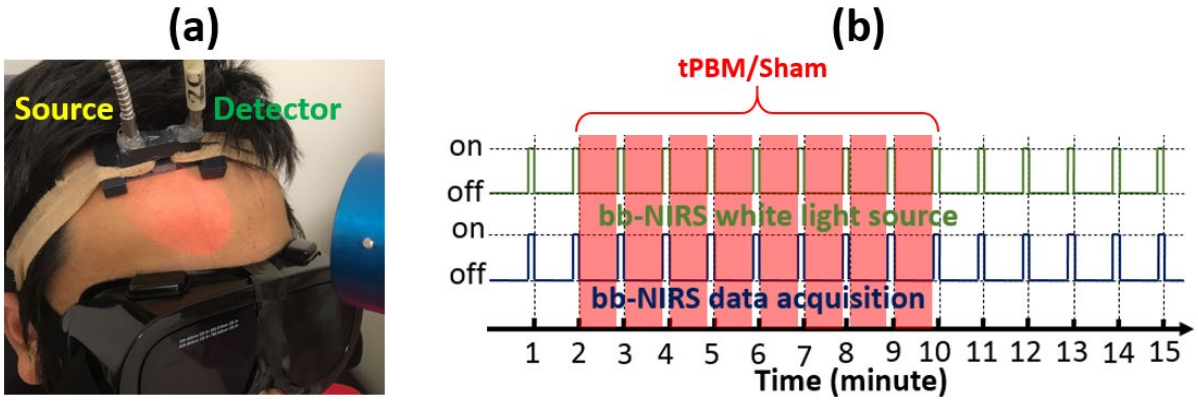

Figure 1 *(a) A picture of experimental setup showing (1) two fiber bundles for tPBM/ sham light delivery (source) and detection (detector) on a human forehead and (2) circular area on the forehead under 4-cm-diameter laser illumination. Note that the laser aperture shown is more than 2 cm away from the forehead to show a clear illumination spot/ area. (b) Experimental protocol of interleaved measurements.*

2.2.2.3 Experimental Protocol

Both tPBM and sham experiments were conducted in a dark locked room without any reflective surfaces. When the laser system was in use, a warning sign was placed on the door to further dissuade individuals from entering. Protective goggles were worn by all the individuals in the lab room to ensure eye safety for

both the participants and operators. Participants were also asked to keep their eyes closed during the entire experiment procedures to further reduce the possibility of eye injury as well as to maintain blind between the sham versus tPBM conditions. Participants had no information on which condition they were given until they completed both of their visits to the lab. As soon as the participants entered the lab, they were asked to sit on an inclined chair comfortability. The protective goggles were worn over their eyes. The horizontally I-shaped bb-NIRS probe was then placed on subject's right forehead above the eyebrow and secured using an elastic bandage (see Fig. 1(a)). After the probe was attached comfortably on the scalp, the bb-NIRS system was switched on to show the stability of the spectral intensities to confirm artifact-free/motion-free time-dependent recordings under resting state.

2.2.2.4 Time-dependent Δ[HbO] and Δ[oxi-CCO]

The same interleaved experimental protocol was followed with respect to the previous study (Wang, Tian et al. 2017). Briefly, each experiment consisted of a 2-minute baseline, an 8-minute tPBM/sham light delivery, and a 5-minute recovery period, as shown in Fig. 1(b). At the end of each minute, tPBM/sham was paused for 5 seconds for bb-NIRS recording of the spectral intensities that diffused back from the human brain. In this way, 15 spectral data points were

obtained at the end of each experiment and further processed/quantified as time-dependent Δ[HbO] and Δ[oxi-CCO]. Among the 15 data points recorded from each participant in each experiment, the first two points recorded before the onset of tPBM/sham were regarded as baselines. They were used as references to quantify Δ[HbO] and Δ[oxi-CCO] for the following 13 data points during and after tPBM/sham, leading to 13 time-dependent Δ[HbO] or Δ[oxi-CCO] readings in μM for each experimental run. This time-dependent data process was repeated for each participant in both tPBM and sham experiments.

2.2.3 Statistical analysis for comparison of two studies

Data used for comparisons in this study included the datasets collected from 11 young adults at UTA in 2016 and the datasets collected from 15 young and 5 older adults at UTSW in 2019. We conducted three steps of statistical evaluations/comparisons over these data sets for assessing tPBM-induced effects on cerebral hemodynamic and metabolic activities: (1) comparison between two young-adult groups measured under different operating conditions (i.e., at different experimental sites with different operators from different participating subjects with a 3-year time interval); (2) comparison between two age groups measured under the same operating conditions; (3) comparison of tPBM-induced sham-controlled changes between two age groups measured

under the same operating conditions. Specifically, in Step I, two-sample t-tests were performed on time-dependent Δ[HbO] and Δ[oxi-CCO] values at each time point (over a total of 15 temporal points) taken from young adults between the current (n=15) and previous (n=11) studies. The comparisons between the two young-adult groups were analyzed per each time point under tPBM and sham conditions separately. Likewise, in Step II, two-sample t-tests were performed on time-dependent Δ[HbO] and Δ[oxi-CCO] values of the participants in two different age groups (n=15 for young and n=5 for older) measured under the identical operating conditions in this study. In Step III, sham-controlled changes of Δ[HbO] and Δ[oxi-CCO] were quantified by subtracting sham-derived (Δ[HbO] or Δ[oxi-CCO]) values from tPBM-derived (Δ[HbO] or Δ[oxi-CCO]) values at each of the 15 time points for both age groups separately, followed by two-sample t-tests to test age-related effects of tPBM. A two-tailed level of $0.01 < p < 0.05$ and $p < 0.05$ was chosen to be statistically significant in these tests.

2.3 Results

2.3.1 Comparisons of Δ[HbO] and Δ[oxi-CCO] between two young adult groups

The time-dependent cross-subject means as well as standard errors of Δ[HbO] and Δ[oxi-CCO] from the current and previous study (Wang, Tian et al. 2017) are plotted in Figs. 2(a) and 2(b), respectively. Based on two-tailed two-sample t-tests, there was no significant difference ($p > 0.05$) observed between these two groups for both Δ[HbO] and (b) Δ[oxi-CCO], indicating a high reproducibility of using bb-NIRS to measure tPBM effects on young human adults.

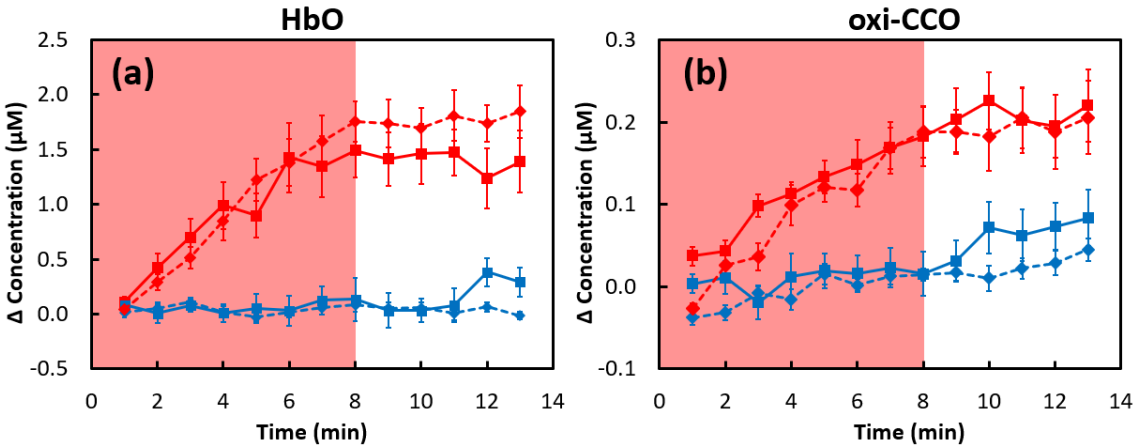

Figure 2 *Comparison of concentration changes of (a) Δ[HbO] and (b) Δ[oxi-CCO] measured from two groups of young adults in the current (solid lines; n=15) and previous (dashed lines; n=11) study. The red symbols and lines indicate the results from the tPBM experiment, while the blue symbols and lines indicate those from the sham experiment. The error bars are standard errors of mean. The shades indicate the time durations of tPBM/ sham illumination. Significant differences in tPBM and sham measurements between the two young-adult groups (solid lines: current study; dashed lines: previous study) are marked with "*", indicating p-value < 0.05.*

2.3.2 Comparisons of Δ[HbO] and Δ[oxi-CCO] between two age groups

Time-dependent Δ[HbO] and Δ[oxi-CCO] measured from 15 young adults and 5 older adults in this study are plotted in Figs. 3(a) and 3(b), respectively. While the time-dependent changes in Δ[HbO] between the two age groups showed very similar trends, significant differences were observed in Δ[oxi-CCO] between the two age groups. Specifically, for both the tPBM and sham experiments, the older group presents a significantly lower level of Δ[oxi-CCO] than the younger group.

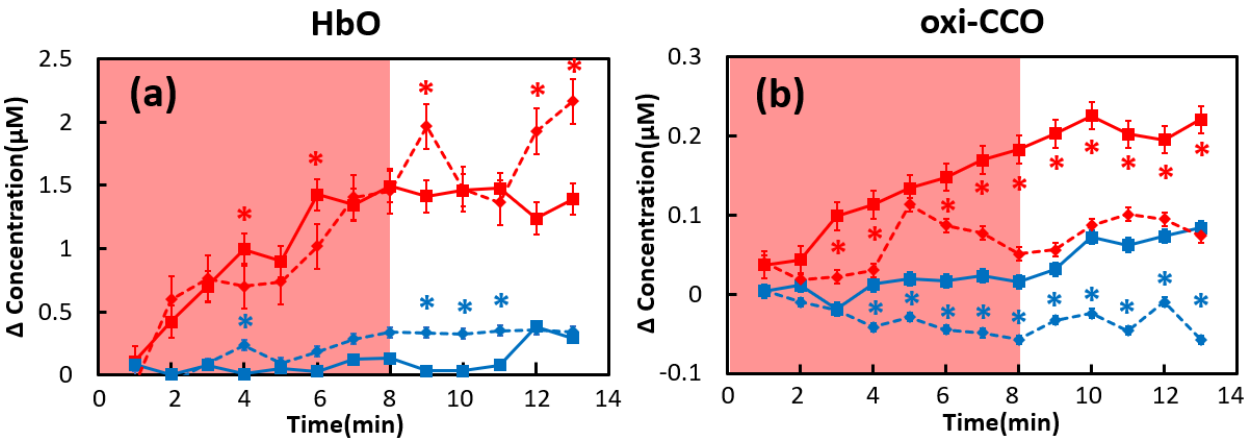

Figure 3 *Comparison of concentration changes of (a) Δ[HbO] and (b) Δ[oxi-CCO] measured in this study from a young adult group (solid lines; n=15) and an older adult group (dashed lines, n= 5). The red color represents the tPBM experiment, while blue color denotes sham experiment. The error bars are standard errors of mean. The shades indicate the time durations of tPBM/sham*

illumination. Significant differences in tPBM and sham measurements between two age groups (solid: young adults; dashed lines: older adults) are marked with "", indicating p-value < 0.05.*

2.3.3 Comparisons of net changes in Δ[HbO] and Δ[oxi-CCO] of between two age groups

To determine the relative effects of tPBM from two age groups, sham-controlled changes of Δ[HbO] and Δ[oxi-CCO] were quantified for each subject by obtaining net changes with respect to the results under the sham condition. The time-dependent, group-averaged net-changes of Δ[HbO] and Δ[oxi-CCO] from 15 young adults (red symbols and lines) and 5 older adults (blue symbols and lines) were plotted in Figs. 4(a) and 4(b), respectively. The two-tailed, two-sample t-tests revealed that there was no statistically significant difference between the two age groups for tPBM-induced Δ[HbO] and Δ[oxi-CCO] effects with respect to the sham experiments.

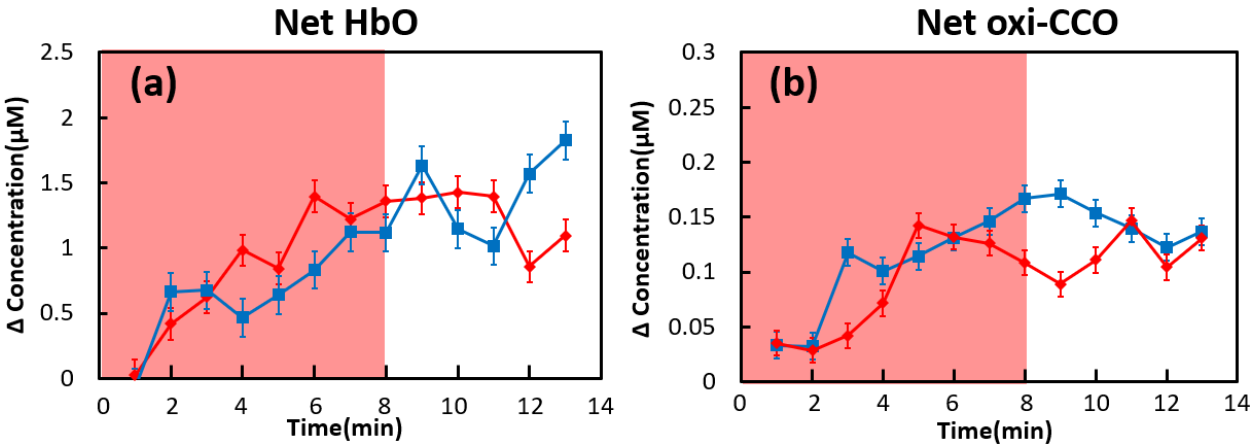

Figure 4 *Net-changes of (a) Δ[HbO] and (b) Δ[oxi-CCO] measured in this study from a young adult group (red symbols and lines; n=15) and an older adult group (blue symbols and lines; n= 5). The error bars are standard errors of mean. The shades indicate the time durations of tPBM/sham illumination. Significant differences between the two age groups are marked with "*", indicating p-value < 0.05.*

2.4 Discussion

2.4.1 Reproducible Hemodynamic and Metabolic Effects of tPBM in Young Adults

The photo-oxidation effects of PBM on CCO have been discussed for decades. More recently tPBM-induced behavioral improvements on human cognition (Rojas and Gonzalez-Lima 2011, Barrett and Gonzalez-Lima 2013, Blanco, Maddox et al. 2017) and mental illness (Cassano, Petrie et al. 2016, Hamblin

2016, Naeser, Martin et al. 2016, Naeser, Ho et al. 2019) have been reported.. Without objective measures of changes in the redox state of CCO in the human brain *in vivo*, it would be difficult to design effective tPBM protocols and intervention for safe, effective, and optimal photobiomodulation effects for future applications. To fulfill this goal, we recently applied bb-NIRS and non-invasively quantified the changes of tPBM-induced Δ[HbO] and Δ[oxi-CCO] in the brain of young human adults (Wang, Tian et al. 2017). Its conclusions helped to understand the mechanism of action of tPBM. However, any new development of methodology and scientific findings require reproducibility with reasonable sample size. Since the previous study was the first published report of tPBM effects on cerebral Δ[HbO] and Δ[oxi-CCO] measured by bb-NIRS and based on a small sample of 11 young controls, the reproducibility of the findings is important to be examined and statistically tested.

By applying statistical two-sample t-tests, we compared the young healthy subjects, 11 sets of data collected in year 2016 at UTA versus the 15 sets of data collected from a new group of young subjects in year 2019 using the same experimental setup at UTSW. As shown in Fig. 2, the cross-subject means of Δ[HbO] and Δ[oxi-CCO] from the two groups of young adults have no statistical difference under both tPBM and sham conditions, demonstrating the high reproducibility for the measured respective parameters. Specifically, at each of

temporal points, all the two-sample t-test comparisons reveal no significant difference between the measurements of the two sets of data.

2.4.2 Potential Beneficial Effects of tPBM on Older Adults

Aging is the major risk for many health conditions, such as Alzheimer's Disease, hypertension, and cardiovascular disease (Farkas and Luiten 2001, Lakatta and Levy 2003). One of the leading reason of aging is thought to be the accumulation of oxidative stress over time (Kadenbach, Ramzan et al. 2009). Oxidative stress can be caused by the natural generation of reactive oxygen species (ROS) during ATP production. The ROS hold an extra electron in their molecular structure, making them chemically reactive to damage cellular structures and thus causing cell death (Simon, Haj-Yehia et al. 2000). While a small amount of ROS plays a vital role in boosting cellular functions (Hill and Van Remmen 2014), oxidative stress occurs when the generation of ROS becomes faster than the speed that they can be removed by the natural cellular mechanisms (Leutner, Eckert et al. 2001). The healthy functioning of oxidized CCO is believed to efficiently convert ROS into a chemically steady state without the extra electron. Therefore, having a large concentration of [oxi-CCO] can inhibit the fast accumulation of cellular ROS, which protects the cellular environment (Collman, Devaraj et al. 2007). In

the case of aging, when CCO gradually decreases its function, less concentration of [oxi-CCO] exists within cells and/or neurons. Therefore, ROS will accumulate increasingly to induce oxidative stress (Musatov and Robinson 2012). Given the observation that tPBM was able to boost Δ[oxi-CCO] in an equal amount between young and older adults (Fig. 4), we speculate or expect that tPBM may be able to induce cognition-enhancing benefits on older brains. This speculation needs to be further investigated/tested in future research while several recent publications reported supporting evidence based on behavioral measures (Vargas, Barrett et al. 2017).

2.4.3 Limitations and Future Work

While this study has provided high reproducibility of tPBM being able to upregulate hemodynamic and metabolic activities measured in different group of young adults as compared with those reported in ref. (Wang, Tian et al. 2017), there are several limitations of the study that need to be future investigated. . First, the bb-NIRS system is very sensitive to motion artifacts during the 15-min measurements. The current setup requires the subjects to keep minimal motion and an experienced operator to collect stable and meaningful data. In future studies, an effective methodology for motion artifact detection/removal in the

bb-NIRS data should be developed to warrant the quality and accuracy of tPBM-induced effects. Second, we need to increase the sample size for the older adults in order to confirm the findings that tPBM induces the same amount of hemodynamic and metabolic increases with respect to the sham experiment regardless of age differences. Last, it is unclear how much the measured Δ[oxi-CCO] signal is affected by the human scalp where a certain concentration of mitochondria exists and their redox state of CCO should contribute to the detected signal on the forehead scalp. There is no clear answer to solve this problem yet. A potential solution could be a time-resolved bb-NIRS approach, allowing for layer-resolved quantification of Δ[oxi-CCO] to separate the signals coming from the superficial scalp layer and the cortical regions.

2.5 Conclusions

In this study, we were able to show high reproducibility of sham-controlled, tPBM-induced increases in cerebral Δ[HbO] and Δ[oxi-CCO] measured by bb-NIRS in a young adult group versus a different group reported in a previous study (Wang, Tian et al. 2017). The statistical analysis demonstrated no significant differences in tPBM-induced cerebral effects between these two sets of measurements taken from different young participants at two different sites (UTA, UTSW). We also demonstrated the agreement of net tPBM effects with

respect to the sham conditions on both young and older adults. These findings indicated the robust reproducibility or reliability of bb-NIRS in quantifying tPBM effects.

2.6 Disclosures

No conflicts of interest, financial or otherwise, are declared by all the authors.

2.7 Acknowledgements

This work was supported in part by the National Institute of Mental Health/National Institutes of Health under the BRAIN Initiative (RF1MH114285). We also acknowledge the support in part from the STARS program by the University of Texas System. The authors would like to thank Ms. Devarshi Desai for her assistance with human data collection.

Chapter 3 : Non-invasive transcranial photobiomodulation with 1064-nm laser stimulates information flow across the human cortex in vivo: an eCONNECTIME analysis

Tyrell Pruitt, Xinlong Wang, Hashini Wanirachichi, and Hanli Liu

(This chapter is a manuscript that will be submitted soon)

3.1 Introduction

Transcranial photobiomodulation (tPBM) is a non-invasive method of using light in the near-infrared (NIR) range (660 nm - 1100 nm) to enhance or stimulate cellular metabolism and hemodynamic oxygenation within the human brain, leading to behavioral benefits reported by many studies, including improvement of cognitive function in older adults (Chan, Lee et al. 2019) (Salehpour, Farajdokht et al. 2019) (Odinokov and Hamblin 2018) and treatments of brain disorders in clinical settings (Argenta, Ballman et al. 2017) (Hamblin 2018) (Hamblin 2016). The mechanism of action of tPBM has been based on the mitochondrial photo-oxidation of complex IV of the electron transport chain, also

known as cytochrome c oxidase (CCO), which catalyzes oxygen metabolism and thus accelerates the production of Adenosine triphosphate (ATP) (Karu 2010) (Oron, Ilic et al. 2007) (Liu, Liu et al. 2009). Absorption of NIR light by CCO in tissue can convert CCO in its reduced state into its oxidized state (oxi-CCO); the photo-oxidation of CCO enhances the proton gradient and then accelerates the production rate of intracellular ATP (de Freitas and Hamblin 2016) (Hamblin 2018) (Serrage, Heiskanen et al. 2019). The higher amount of ATP is formed by tPBM *in vivo*, the more activation of synaptic connections is expected in the brain tissue because of a high concentration of mitochondria in neurons (Wong-Riley, Liang et al. 2005) (Karu 2013) (Salehpour, Mahmoudi et al. 2018). This mechanism of action was supported by our recent studies using broadband NIR spectroscopy (bb-NIRS), which allowed for non-invasive, human measurement *in vivo* of tPBM-induced increases in cerebral oxygenation and oxi-CCO concentration (Wang, Tian et al. 2016) (Wang, Tian et al. 2017) (Pruitt, Wang et al. 2020).

On the other hand, our group also reported sham-controlled electroencephalography (EEG) based studies, demonstrating tPBM-induced power increases in electrophysiological activity at alpha (0.5-4 Hz) and beta (4-8 Hz) oscillations generated by tPBM on the human brain (Wang, Dmochowski et al. 2019) (Wanniarachchi, Wang et al. 2020), showing consistent trends with those published by (Zomorrodi, Loheswaran et al. 2019). While these findings

are significant, it is essential to understand where the scalp EEG signals or rhythm powers were altered by tPBM and where those signal changes came from and how those changes were communicated with different cortical regions. To better understand those questions, we made our new hypothesis: Right prefrontal tPBM enables increasing directional interactions of brain functional networks or so-called information flow (IFlow) mainly at alpha and beta frequencies across cortical regions. This study aimed to prove this hypothesis by using the Granger-causality approach to analyze the EEG data reported in our previous study (Wanniarachchi, Wang et al. 2020). Specifically, a highly specialized MATLAB toolbox, called eCONNECTOME, was used to map the areas of the brain communicating with one another by utilizing analysis methods known as directed transfer function (DTF) and adaptive direct transfer function (ADTF) (He, Dai et al. 2011) (Sohrabpour, Ye et al. 2016) (Dai, Zhang et al. 2012). These analysis methods are both a derivative of an autoregressive prediction method, known as Granger causality, which was initially used to predict economic trends but was found to be useful in analyzing causal relationships in many other applications (Hesse, Möller et al. 2003) (Gow Jr, Segawa et al. 2008) (Marinazzo, Liao et al. 2011).

3.2 Methods

3.2.1 Participants

A total of 19 healthy participants were recruited from the University of Texas at Arlington (UTA), where the measurements also took place. The inclusion/exclusion criteria were the same as those in our previous studies (Wang, Dmochowski et al. 2019). The study was approved by UTA's Institutional Review Board (IRB) and complied with all applicable FDA and NIH guidelines. Written informed consent was obtained before the experiment for all participants. Every participant was asked to take two experiments with either tPBM or sham stimulation in an order that was randomized for each participant, in two visits separated by 3-4 days to avoid pre-treatment effects.

3.2.2 EEG-tPBM experimental protocol

An FDA-cleared, 1064-nm, continuous-wave (CW) laser (Model CG-5000 Laser, Cell Gen Therapeutics LLC, Dallas, Texas) was used in this experiment per previous studies (Wang, Dmochowski et al. 2019) (Wanniarachchi, Wang et al. 2020). The laser produced a collimated beam with an illumination area of 13.6 cm^2. This study was sham-controlled, with participants receiving zero laser power stimulation through a covered aperture during sham protocol visits and

3.4 W of power during real tPBM visits. This laser power of 3.4 W resulted in a constant power density of 0.25 W/cm^2 (namely, 3.4 W/13.6 cm^2) being applied on each participant's forehead. Both researchers and participants wore protective goggles during both visits. Participants were instructed to keep their eyes closed during the entire experiment for added protection and proper blinding to which kind of stimulation they were receiving.

The experimental setup of this experiment is shown in Fig. 5, along with a schematic experimental design. EEG data were collected concurrently with tPBM using a 64-channel EEG instrument (ActiveTwo, Biosemi, the Netherlands) with an EEG cap having the international 10-10 configuration setting. tPBM was applied at 2 cm to the right side of the forehead near the Fp2 location of the global 10-10 electrode configuration. Experiments consisted of a 2-min baseline, an 8-min tPBM or sham stimulation, followed by a 3-min recovery period for a total experimental duration of 13 minutes. The experiments were performed for both the randomized sham and tPBM visits several days apart to avoid pre-treatment effects.

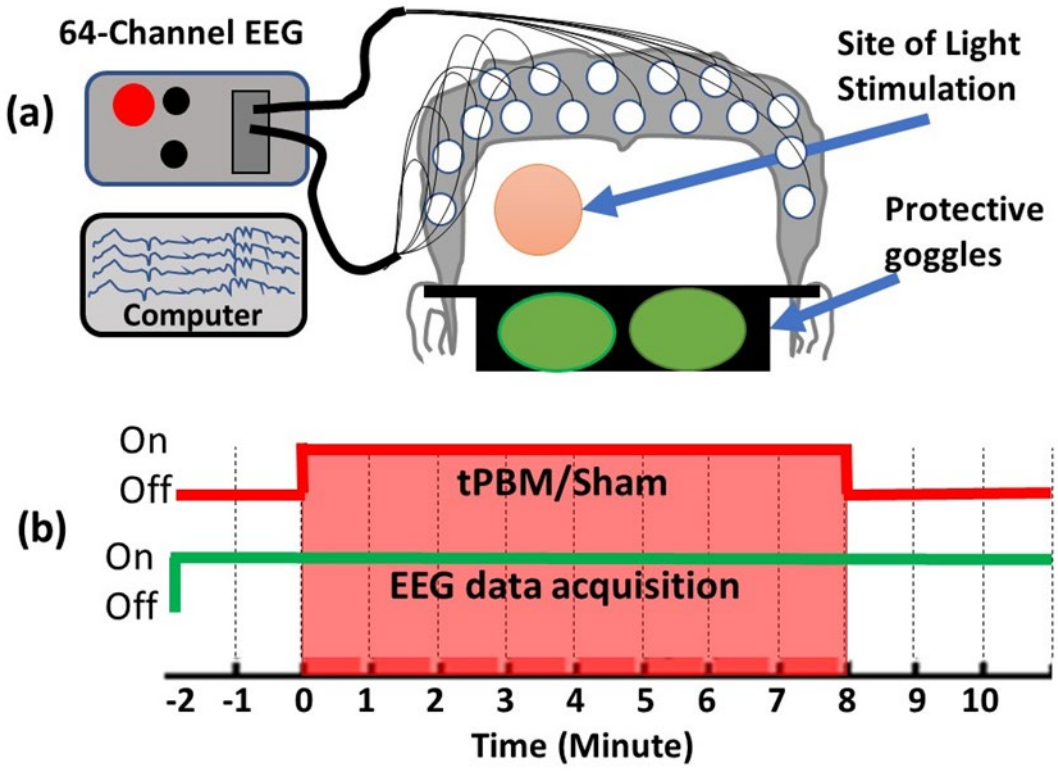

Figure 5 *Schematic of (a) EEG-tPBM experiment setup and (b) experimental protocol. In (a), the EEG system has 64 channels and connects the recording unit with the 64 electrodes on the cap. The tPBM site of the 1064-nm laser has a diameter of ~4.2 cm (pictured in orange). The laser power was set at 3.4 W or 250 mW/cm2 for proper stimulation. In (b), the experimental protocol consists of EEG data acquisition time (green line) and laser/sham stimulation time (pictured schematically with a solid red line and highlighted with red shading).*

3.2.3 EEG Data Analysis

Data analysis was performed in several steps on the collected raw EEG data, as outlined in Fig. 5.

3.2.3.1 Preprocessing and bandpass filtering

All EEG datasets were processed using the EEGLAB (Delorme and Makeig 2004) and eCONNECTOME toolboxes (He, Dai et al. 2011) (Sohrabpour, Ye et al. 2016) (Dai, Zhang et al. 2012) on the MATLAB platform. With EEGLAB, each raw time series was bandpass filtered between 0.1 and 70 Hz, followed by a notch filter to remove 60-Hz electrical line noise. Artifacts were identified visually and removed using independent component analysis via the "runica" function in EEGLAB. A mean reference was used for the 64 EEG channels. Next, the preprocessed data were also separately filtered into the five most commonly used EEG frequency bands: delta (0.5-4 Hz), theta (4-8 Hz), alpha (8-13 Hz), beta, (13-30 Hz), and gamma (30-70 Hz) frequency bands.

3.2.3.2 Baseline Processing

The 2-min baseline segments were extracted and averaged across all 19 participants for both sham (see Fig. 6) and tPBM experiments, followed by

respective quantifications of power spectral density (PSD) using the p-welch calculation method(Welch 1967) (Cooley, Lewis et al. 1969) (Welch 1987) for each of 64 channels. To examine whether the two baseline powers (of sham and tPBM) across 64 channels were statistically different, the group-level, spectral-averaged (0.5-70 Hz) EEG powers were compared using a two-sample t-test for each channel with an FDR corrected p-value threshold of $p<0.01$. When converting or reconstructing the preprocessed EEG data into the sensor/dipole and cortex/brain space, we used eCONNECTOME's baseline removal function to eliminate the remaining EEG data's baseline effect in the time series.

3.2.3.3 Granger Causality and its application (i.e., eCONNECTOME)

Granger causality was initially developed as a predictive autoregressive model commonly used in the economic sector to estimate future stock prices (Foresti 2006) (Rashid 2007) (Liang, Lin et al. 2013). However, due to its potential application for detecting causal signals in the EEG field, it was modified slightly to accommodate this purpose. In practice, an open-source MATLAB toolbox package called eCONNECTOME (He, Dai et al. 2011) (Sohrabpour, Ye et al. 2016) (Dai, Zhang et al. 2012) is available for us to perform Granger-

causality analysis and to understand/visualize electrophysiological causal relationships due to tPBM among different cortical regions. In our data processing, the baseline data were subtracted from those during the 8-min stimulation and 3-min recovery periods. The 64-channel, baseline-subtracted EEG time series were input into eCONNECTOME to calculate the modified version of Granger Causality known as Directed Transfer Function (DTF).

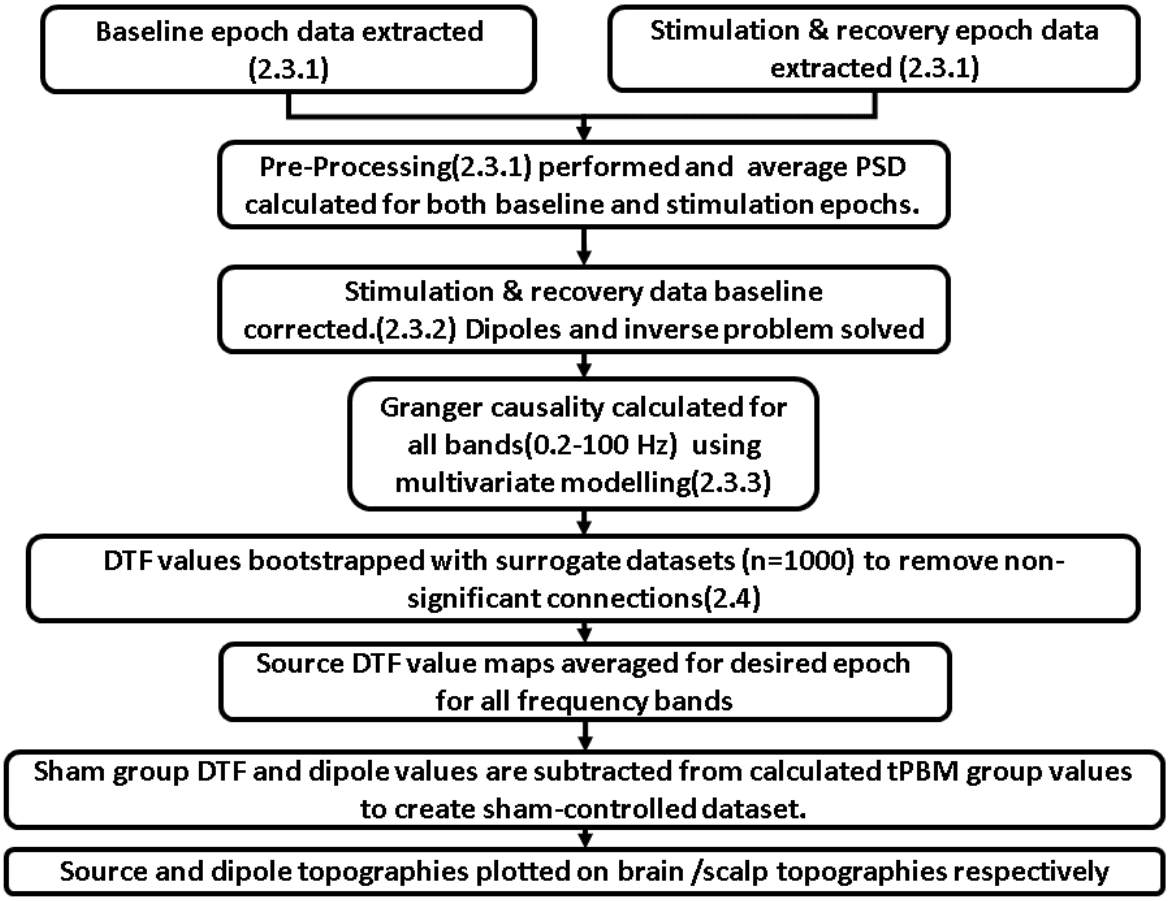

Figure 6 *Flowchart of EEG data analysis process from raw data to final subtracted topographies. Items within the blue square were repeated for all 19 subjects to create the group average for both tPBM and sham groups.*

3.2.3.4 Statistical analysis/bootstrapping

Processed datasets were set to a 95% confidence interval (p-value < 0.05) in a non-parametric bootstrapping process. The original time series for each calculation are converted to Fourier space, and random phases are shuffled

without changing magnitude. The surrogate datasets are then converted back into the time domain, and the process is repeated to generate 1000 phase shuffled surrogate datasets. These surrogate datasets are then converted to DTF values, and their distribution is analyzed where the null hypothesis is no connectivity exists between the two electrodes. DTF connectivity values meeting our confidence interval (p-value < 0.05) are retained.

After performing this bootstrapping analysis, only significant ($p < 0.05$) connections remained. A minimum threshold of 0.15 DTF value was used to isolate the top 4 connections present in the brain space during the 8 minutes of tPBM stimulation. The DTF value matrix for each subject (n=19) and condition for these 4 top significant connections were then subtracted between sham/tPBM groups and averaged using the sham subtracted values. The new sham subtracted average DTF values were plotted using eCONNECTOME's ROI connectivity imaging capabilities.

The non-sham subtracted DTF values were separated into delta (0.5-4 Hz), theta (4-8 Hz), alpha (8-13 Hz), beta (13-30 Hz), and gamma (30-70 Hz) frequency bands for each subject/condition. These band-separated DTF values were then converted via Fisher transform into *z*-values to return normality to the value distribution. Significance ($p<0.05$) between sham/tPBM conditions for each

frequency band was determined by performing a 1-sample test between the z-values for all subjects.

3.3 Results

3.3.1 Comparison of power spectral density between baselines of sham and tPBM stimulation

Power spectral density (PSD) analysis using the pwelch method of spectral analysis in EEGLAB shows no significant differences between the two baseline readings taken before the tPBM and sham stimulations using a two-sample t-test for each pair of the 64 channels over the group of 19 subjects. The group average spectral plots are presented in Figure 7(A), providing a visual representation of the similarities of the two groups' stimulation epochs. If there were significant differences between the two groups after FDR correction, they were represented by a black bar under the area. Comparing source space dipole information between sham and tPBM protocol measurement baselines (Fig. 7B) shows no significant difference between the 2 baseline periods. With this information we can safely assume there is a significant ($p < 0.05$) difference between the stimulation epochs in power and that baseline information flow remains largely the same before intervention by tPBM.

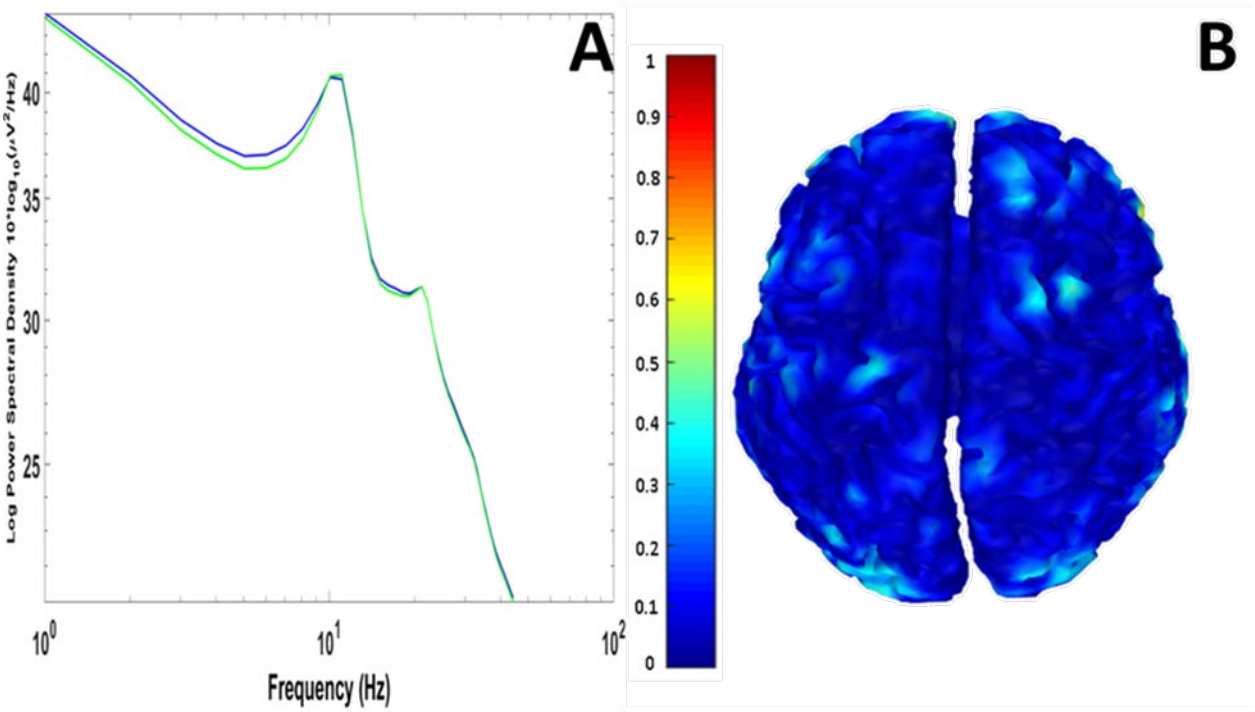

Figure 7 *Group-averaged (n=19) power spectral density of all 64 channels during baseline (A). The blue lines represent the sham stimulation group average, while the green lines represent the tPBM group average. FDR corrected significance($p<0.05$) for a frequency is indicated by a dark black bar underneath the x-axis. No significant difference exists between these two groups of PSDs for each channel in the sham and tPBM baseline groups. Normalized sham-subtracted source space visualization (B) presented on a scale of 0 (blue) to 1 (red) where 1 is maximal dipole activation in that time epoch.*

3.3.2 Comparison of power spectral density between stimulation periods of sham and tPBM stimulation

Power spectral density (PSD) analysis using the pwelch method of spectral analysis in EEGLAB shows no significant differences between the two baseline readings taken before the tPBM and sham stimulations using a two-sample t-test for each pair of the 64 channels over the group of 19 subjects. The group average spectral plots are presented in Figure 8(A), providing a visual representation of the similarities of the two groups' stimulation epochs. If there were significant differences between the two groups after FDR correction, they were represented by a black bar under the area. Comparing source space dipole information between sham and tPBM protocol measurement baselines (Fig. 8B) shows no significant difference between the 2 baseline periods. With this information we can safely assume there is a significant ($p < 0.05$) difference between the stimulation epochs in power and that baseline information flow remains largely the same before intervention by tPBM.

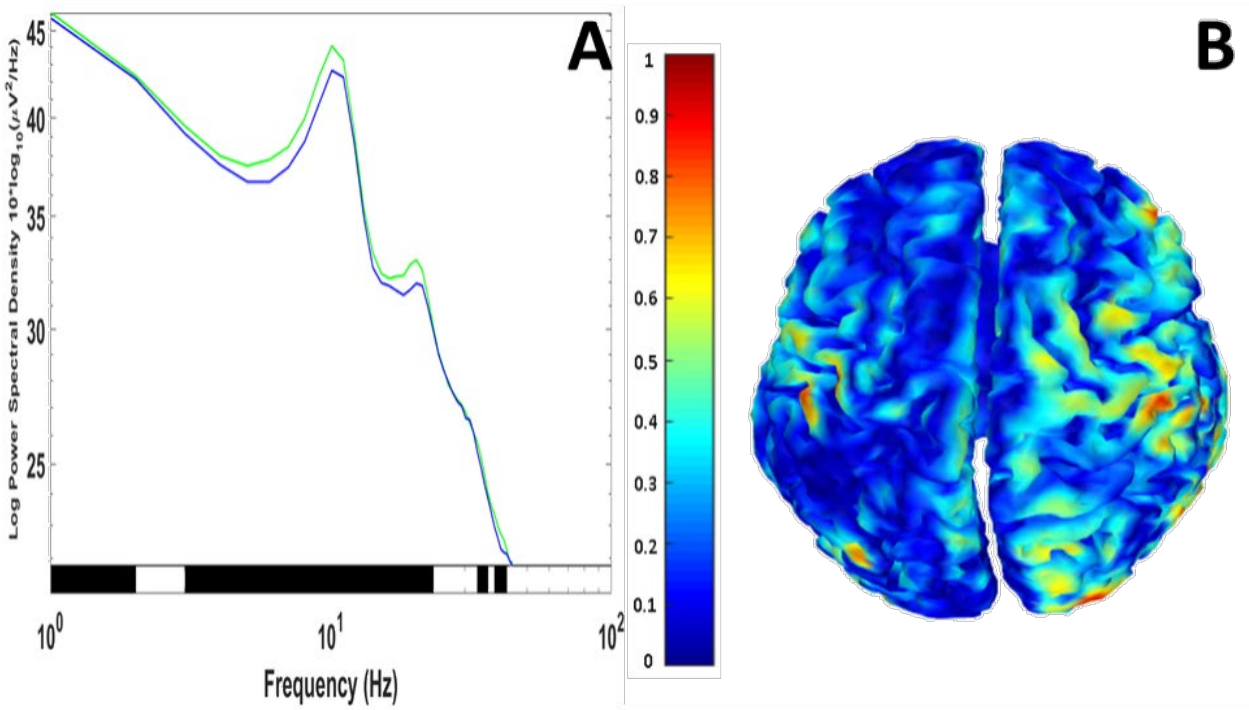

Figure 8 *Group-averaged (n=19) power spectral density of all 64 channels during the 8 minutes of stimulation (A). The blue lines represent the sham stimulation group average, while the green lines represent the tPBM stimulation group average. FDR corrected significance($p<0.05$) for a frequency is indicated by a dark black bar underneath the x-axis. Normalized sham-subtracted source space visualization (B) presented on a scale of 0 (blue) to 1 (red) where 1 is maximal dipole activation in that time epoch.*

3.3.3 Sham-subtracted tPBM source localization at all frequency bands

During the 1st 4-min tPBM (i.e., 0-4 min), sham-subtracted, tPBM-evoked alterations in IFlow in the sensor and cortical space at a broadband and 5 specific frequency bands are shown in Fig. 9(A), with a high probability of increased cortical IFLow near electrode Fp2, which is the site of stimulation. The sham-subtracted baseline region shows minimal significant alteration in information flow (shown on the right top corner). This active region stretches across the frontal area of both the right and left hemispheres of the brain and as far back as the right occipital region. For frequency-specific, alpha and beta bands show cortical IFlow in the right frontal area near Fp2. Delta and theta bands show an increase in IFlow during tPBM in the mid-brain and right occipital, but this effect does not carry over into the following 4-minute period. Gamma band does not show any significant activation during the first 4 minutes of tPBM stimulation.

During the 2nd 4-min tPBM (i.e., 4-8 min), sham-subtracted, tPBM-evoked alterations in IFlow in the sensor and cortical space at the broadband and 5 specific frequency bands are shown in Fig. 9(B), also with a high probability of increased IFlow near the site of stimulation (Fp2). This active region stretches across the frontal area of both the right and left hemispheres of the brain and as far back as the right occipital region. When divided into frequency bands, alpha and beta bands show increased cortical information flow

in the right frontal region near Fp2(Fig. 9 A3, A4, B3, B4). Delta and theta bands show significant increases in the mid frontal area during the first 4 minutes of tPBM(Fig.9 A1, A2) but not during the following 4 minutes or post-stimulation(Fig.9 B1, B2, C1, C2)

The following 3 minutes after tPBM stimulation show a marked increase in the beta frequency band in the midbrain region that is not present in any other time period measured (Fig.9 C5). Also, the temporal region gamma frequency band source is still partially present after tPBM stimulation has stopped (Fig.9 C5). Delta and theta frequency bands even show small amounts of information flow in the frontal and midbrain portions of the brain after stimulation (Fig.9 C2,4C3), although not as actively as the first 4 minutes of stimulation (Fig.9 A2, A3).

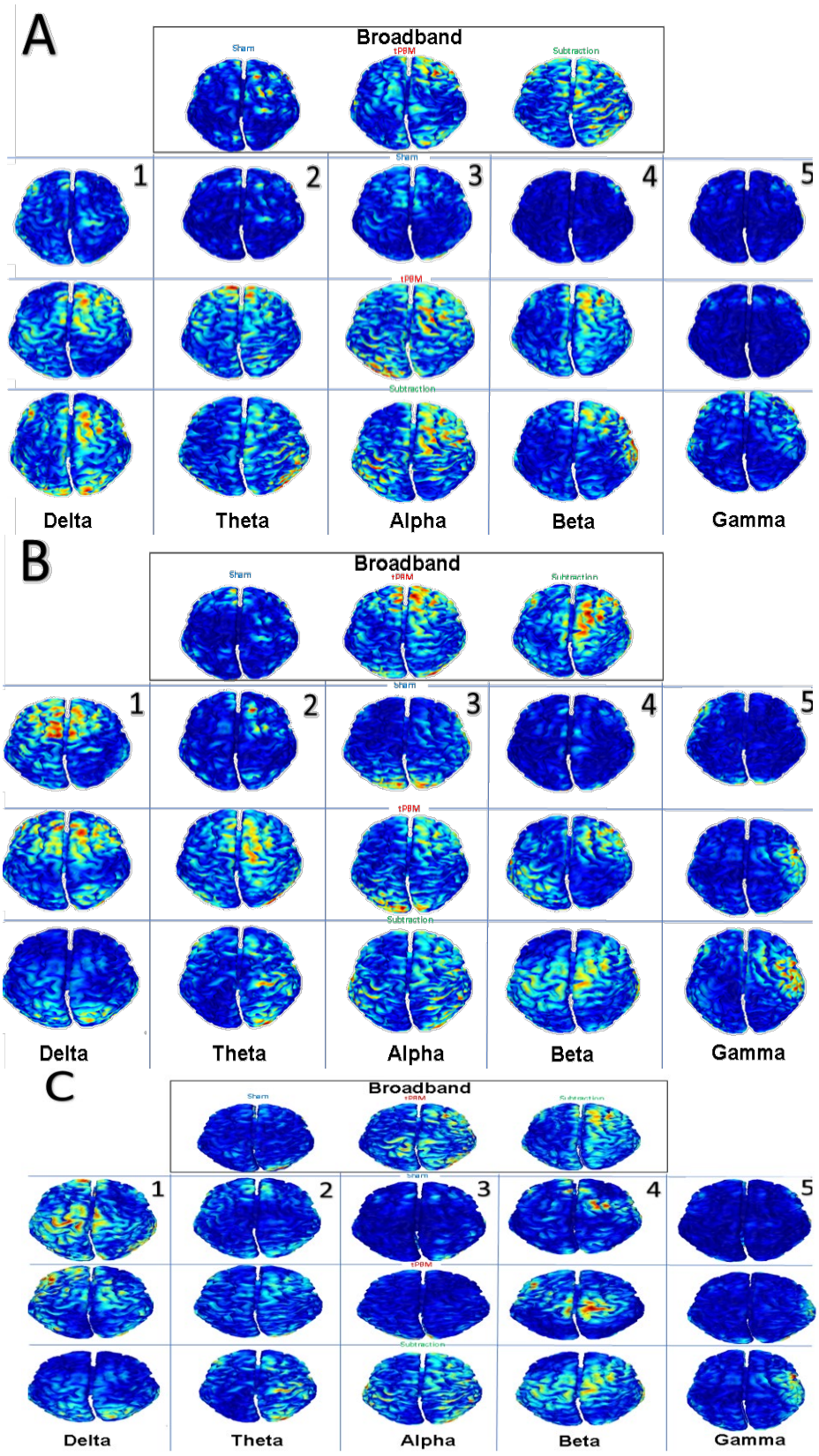
A
Broadband
Sham
tPBM
Subtraction
1
2
3
4
5
Delta
Theta
Alpha
Beta
Gamma
B
Broadband
Sham
tPBM
Subtraction
1
2
3
4
5
Delta
Theta
Alpha
Beta
Gamma
C
Broadband
Sham
tPBM
Subtraction
1
2
3
4
5
Delta
Theta
Alpha
Beta
Gamma

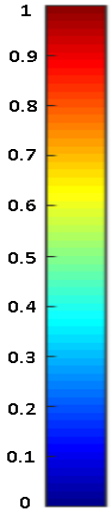
1
0.9
0.8
0.7
0.6
0.5
0.4
0.3
0.2
0.1
0

Figure 9. *Sham subtracted tPBM source localization dipole values for broadband, delta (0.1-4 Hz), theta (4-8 Hz), alpha (8-12 Hz), beta (12-30 Hz), and gamma (30-100 Hz) frequency bands for (A) the first 4-minutes of tPBM stimulation. (B) the second 4-minutes of tPBM stimulation and (C) the 3-minute segment post-stimulation Brain space source localization data is represented on a 3-dimensional brain model on a scale of 0 (blue) to 1 (red) where 1 represents maximal dipole activation in that time epoch.*

3.3.4 Directional IFlow changes during tPBM stimulation

After rejecting all non-significant values from ROI projections (Fig. 10A), all connections were thresholded to a minimum DTF value of 0.15 to find the top

4 connections that are not present during sham stimulation. These top 4 connections were found to be BA_9_46_R to MIL_R, MIL_R to BA_6_R, BA_6_L to BA_6_R, and finally BA_6_R to BA_19_R. These connections form a continuous pathway from BA_9_46_R, the tPBM stimulation site, to BA_19_R. This also indicates 5 regions of the brain where IFlow is altered compared to sham: BA_9_46_R, MIL_R, BA_6_R, BA_6_L, and BA_19_R.

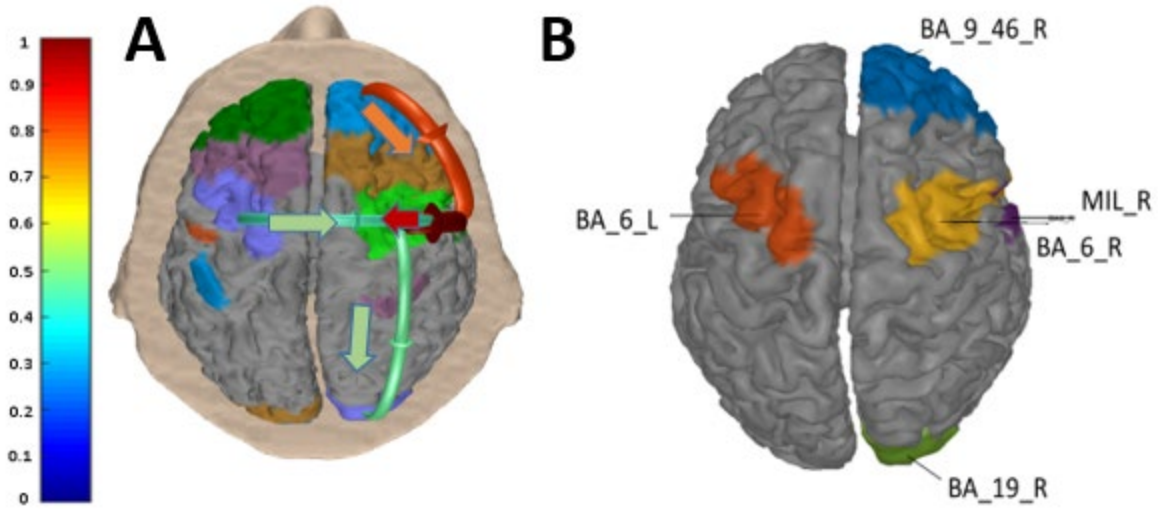

Figure 10 *Group-averaged (n=19) and sham subtracted brain-space representations of directional IFlow. Colored regions represent cortical regions of interest (ROIs), while lines represent DTF values ranging from 0.15(blue) to 1.0(red). The figure on the left(A) includes all regions found to have significant connections after bootstrapping, but only DTF values above the threshold of a DTF value of 0.15 are shown. The figure to the right (B) represents the 5 regions of interest with connections that exceed this threshold labeled with their appropriate Broadman area.*

3.3.5 Z-score based analysis of IFlow

Of the 5 frequency bands tested for their effect on IFlow, only alpha (8-12 Hz) and beta (12-30 Hz) frequency bands had significant alterations across all 4 significant ROI connections. Z-values after Fisher transformation to normalize the distribution of the data show significant alterations compared to sham groups. In these analyzed connections, tPBM group alpha and beta band z-values were always significantly higher than sham group z-values. Higher DTF and z-values indicate an increased amount of information flow between regions in that frequency band.

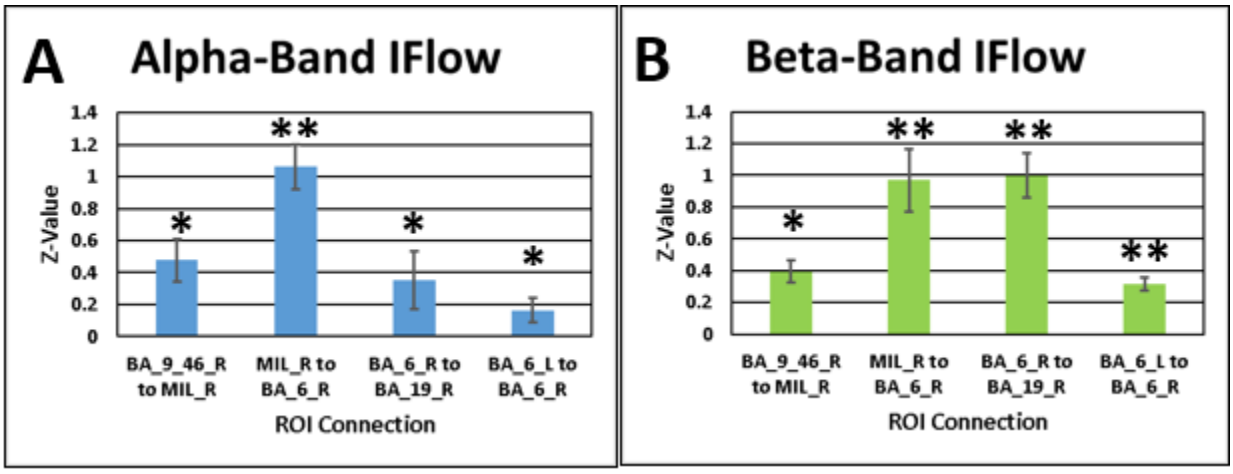

Figure 11 *Group-averaged (n=19) sham and tPBM Granger values after the Fisher transformation. Blue bars indicate sham group averages in their respective ROI groups, while orange bars show the tPBM group averages. Significance is indicated by "*" where "*" indicates (p*

*< 0.05) and "**" indicates (p < 0.01). The left figure (A) is representative of all IFlow in the alpha band (8-12 Hz), and the right figure(B) represents all IFlow in the beta band(12-30 Hz)*

3.4 Discussion

3.4.1 Alpha and beta band information flow increases in the region surrounding the site of stimulation during tPBM stimulation

The collected sham-subtracted tPBM data (Fig. 9 A,B) during stimulation shows an acute increase in information flow originating from the site of stimulation during tPBM. This corresponds to sensor space power increases in alpha and beta frequency bands seen in previous studies (Klimesch 1997) (Egner and Gruzelier 2004) (Klimesch, Doppelmayr et al. 1998) (Klostermann, Nikulin et al. 2007). These increases in information flow can also correspond to vital learning frequencies and pathways associated with visual learning (Ergenoglu, Demiralp et al. 2004) (Sauseng, Klimesch et al. 2005) (Kamiński, Brzezicka et al. 2012). The effects in the beta band persist even after stimulation has ceased (Fig. 9C), possibly indicating a more long-term effect on information pathways

3.4.2 Delta and theta band information flow increases during the first 4 minutes when compared to sham

Both delta and theta frequency band information flow increase during the first 4 minutes of stimulation compared to sham (Fig. 9B). However, this tPBM information flow increase does not remain consistent throughout the measurement. The sham group also experiences a delta and theta band information flow increase during the experiment's remaining 7 minutes. Delta and theta band are often associated with both sleep (Cajochen, Foy et al. 1999) (Anderson and Horne 2003) (Campbell, Darchia et al. 2011) and healing processes (Nuwer, Hovda et al. 2005) (Laibow, Stubblebine et al. 2002) (White 1999) in the brain. Hence, it is possible tPBM enhances the rate at which these processes occur in some way.

3.4.3 Gamma band information flow increases acutely after 4 minutes of tPBM stimulation

Gamma band cortical information flow is not altered during the initial 4 minutes of tPBM stimulation. Still, it is acutely activated in the right temporal region of

the brain for the remaining 4 minutes of stimulation as well as 3 minutes after stimulation has ceased (Fig. 9B,C). This type of acute gamma-band activation is often associated with hypothalamus activation(Carus-Cadavieco, Gorbati et al. 2017) (Talakoub, Paiva et al. 2017) (Von Euler and Söderberg 1957). Hypothalamus gamma frequency waves are thought to contribute in some way to memory consolidation(Kanta, Pare et al. 2019) (Headley and Paré 2013) (Zhang, Fell et al. 2018). This, combined with the alpha and theta activation mentioned previously, builds a strong case that tPBM enhances memory consolidation in some capacity.

3.4.4 Directional information flow increases from the site of tPBM stimulation and the right occipital region of interest

During the stimulation period, IFlow increases in 5 regions of interest (Fig. 5B) in 4 directional connections. These directional connections form a continuous connection between the site of stimulation, BA_9_46_R, and the right occipital region, BA_19_R. (Fig.10A) This type of directional information flow from frontal to parietal and occipital areas indicates visual perception-based learning. (Hillebrand, Tewarie et al. 2016) This type of information flow is contrary to standard resting-state patterns of occipital/parietal to frontal

pathways. (Hillebrand, Tewarie et al. 2016) (Michels, Muthuraman et al. 2013). This directional change compared to sham stimulated individuals indicates a strengthening of the perceptional learning-based pathways only during tPBM stimulation of the frontal region.

3.4.5 Alpha and beta frequency band information flow significantly increases between the top 5 regions of interest

After a frequency band-wise analysis of the connections between the top 5 cortical regions of interest was completed, it became apparent that alpha and beta bands were the predominant carriers of information during tPBM stimulation. In all top 4 connections, both alpha (Fig.11A) and beta (Fig.11B) frequency bands were significantly ($p < 0.05$) higher than the same ROI connections during sham stimulation. Alpha and beta band information flow has been found to reflect general neuroplasticity and learning ability in general. (Sauseng, Klimesch et al. 2005, Thatcher, Palmero-Soler et al. 2016) (Nakamura, Sadato et al. 1999). This suggests tPBM could be used as a general learning aid to reinforce these positive neural connections during an earning task.

3.4.6 Limitations and future work

Since this was the first source localization study for tPBM, it has a few limitations that can be addressed in future investigations. First, the system used was a low density 10-10 scalp electrode system that provides little special resolution. With a higher density EEG system or MEG, these cortical sources could be localized to a much smaller area in the brain due to their higher spatial resolution (Hedrich, Pellegrino et al. 2017) (Klamer, Elshahabi et al. 2015) (Petrov, Nador et al. 2014). Secondly, due to the need to stimulate the upper forehead directly without obstructions, the cap is slightly shifted around 2 cm up along the anterior-posterior midline, which could cause some slight distortion when solving the inverse problem and projecting into the brain space(Pascual-Marqui 1999) (Grech, Cassar et al. 2008). Thirdly, although we have conducted studies previously to rule out full thermal power activation(Wanniarachchi, Wang et al. 2020) (Wang, Dmochowski et al. 2019), we have not conducted the same experiment for alterations in information flow. This is a study that can be undertaken in the future, however, by performing the same analysis on thermal stimulation vs. sham.

3.5 Conclusions

This is the first tPBM source localization experiment reported to demonstrate that tPBM with a 1064-nm laser can significantly and broadly alter cortical information flow in multiple frequency bands. By projecting these scalp connectivity estimates into the brain space, we can now make more accurate inferences about the true origin of the signals our scalp electrodes detect during tPBM. Both alpha and beta band signals have a high probability of originating from the site of stimulation, Fp2, which has never been seen on the cortical level before during tPBM. The pattern of increased information flow also suggests that only a minimal amount of energy needs to be imparted by the laser to induce significant information flow changes. Using this technique on both new and previously collected tPBM data, we can glean more information than ever and possibly localize the exact cortical source of tPBM information flow in the future with access to equipment with higher spatial resolutions such as HD-EEG and MEG.

3.6 Disclosures

No conflicts of interest, financial or otherwise, are declared by all the authors.

3.7 Acknowledgements

This work was supported in part by the National Institute of Mental Health/National Institutes of Health under the BRAIN Initiative (RF1MH114285). We also acknowledge the support in part from the STARS program by the University of Texas System.

Chapter 4 : A comparison of up-regulation of cytochrome-c-oxidase and hemoglobin oxygenation induced by 808-nm, 852-nm, and 1064-nm laser photobiomodulation

Tyrell Pruitt, Xinlong Wang, and Hanli Liu

(This Chapter is a manuscript that will be submitted soon.)

In order to better understand the physiological effects of PBM on the body as a whole and determine the consequences caused by differing mitochondrial densities in muscle compared to neuronal tissue, this study used the arm, as a simpler biological model for the study, rather than the head. In this chapter it will be noticed that the chromophore concentration changes are significantly higher than those displayed in chapter 2. The reason for this difference in concentration is twofold. The first reason is the previously mentioned difference in mitochondrial density as muscle fibers contain a significantly higher number of mitochondria than

neuronal tissue [(Hoppeler and Fluck 2003) (Ernster and Nordenbrand 1967) (Kann and Kovács 2007)], causing PBM to have a greater effect on muscle tissue via CCO oxidation. Secondly, the bb-NIRS source detector spacing used for the head measurement in chapter 2 was 3 cm to ensure the cortex could be detected with the increased penetration depth [(Okada and Delpy 2003)]. However, this increasing source detector separation also leads to a decrease in signal to noise ratio [(Taga, Homae et al. 2007)]. This is why 2 cm was used for the arm measurement since no extra shielding layer exists for light to penetrate or reach muscle tissue. Both of these factors cause higher chromophore changes in arm measurements which may afford a higher sensitivity to detect subtle changes in chromophore concentration caused by the 3 wavelengths that may not have been easily detectable in the brain.

4.1 Introduction

Photobiomodulation (PBM) refers to the use of light to modulate cellular functions for physical or mental benefits. Photobiomodulation has many human applications such as improving the rate at which the body heals

[(Byrnes, Barna et al. 2004, Medrado, Soares et al. 2008, Arany 2016)] and increasing a subject's pain threshold [(de Andrade, Bossini et al. 2017, da Silva, Albertini et al. 2018, de Paula Gomes, Leal-Junior et al. 2018, de Sousa, Kawakubo et al. 2018)]. Lasers and light emitting diodes (LEDs) have been used successfully for therapeutic purposes, such as treating brain injuries like ischemic stroke [(Yang, Tucker et al. 2018, Argibay, Campos et al. 2019, Wang, Dong et al. 2019)] or improving the symptoms of depression [(Cassano, Petrie et al. 2018, Caldieraro and Cassano 2019, Salehpour, Farajdokht et al. 2019)]. PBM has proven itself in many placebo-controlled studies when applied to the forehead in healthy humans to benefit attentive behavior, working memory, and executive functions [(Berman, Halper et al. 2017, Chan, Lee et al. 2019, Mitrofanis and Henderson 2020)].

While the exact mechanism of PBM is not entirely certain, one of the prevailing theories is that a photon is absorbed by the copper subunit of the terminal enzyme in the electron transport chain cytochrome-c-oxidase (CCO)[(Wong-Riley, Liang et al. 2005, Poyton and Ball 2011, Karu 2013)], which enhances the ability of the mitochondria to catalyze the reduction of oxygen to produce ATP more efficiently[(Neves, Gonçalves et al. 2018, Chang, Lee et al. 2019, Rhee, Moon et al. 2019)]. As CCO's activity is increased oxygen

consumption also increases which leads to an increase in the rate of oxidative phosphorylation [(Hamblin 2017, Amaroli, Ravera et al. 2019)] as well as cellular oxygen metabolism [(Beltrame, Ferraresi et al. 2018, Pruitt, Wang et al. 2020)]. As neurons have an increased reliance on mitochondrial oxygen metabolism when compared to most other cell types, PBM has been shown to affect neuronal function to an increased degree [(Zomorrodi, Saltmarche et al. 2017, Salehpour, Mahmoudi et al. 2018, Wang, Dmochowski et al. 2019)].

Broadband near-infrared spectroscopy (bb-NIRS) has been used successfully in the past to monitor oxygenated [HbO] as well as deoxygenated [Hb] hemoglobin levels in human subjects [(Kashyap 2008, Anderson, Kainerstorfer et al. 2015)]. Recently bb-NIRS has even proven itself as a method of monitoring CCO oxidation levels in the human arm [(Wang, Soni et al. 2016, Wang, Tian et al. 2016)] and forehead [(Bainbridge, Tachtsidis et al. 2014, Pinti, Siddiqui et al. 2021) (Wang, Tian et al. 2017)] as well using a curve-fitting algorithm. We used this technology to monitor [HbO], [Hb], and [CCO] concentration changes in the human arm for this experiment to analyze the *in vivo* effects of various wavelengths of near-infrared lasers on each chromophore.

PBM is accomplished using a wide variety of laser or LED wavelengths, most commonly between 600-900 nm [(García-Delaney, Abad-Sánchez et al. 2017)] but also at the wavelength of 1064-nm [(McColloch, Liebman et al. 2020)]. However, these studies often lack overlapping experimental methodology making direct comparisons between each wavelength's efficacy impossible. We investigated the differences in chromophore concentration changes using 3 wavelengths of laser: 808-nm, 852-nm, and 1064-nm to better understand the differences in PBM for each. We used the human forearm rather than the forehead to reduce tissue heterogeneity and avoid complications caused by passing through the skull. This study applied sham-controlled PBM for all three wavelengths at the same power density while collecting bb-NIRS data in the same interleaved fashion to ensure optimal protocol homogeneousness between wavelengths to make accurate and novel comparisons between each possible.

4.2 Materials and methods

4.2.1 Participants

10 healthy normal subjects (6 males, 4 females) aged 21-40 were recruited from the local area of the University of Texas at Arlington and the Arlington area. Interested participants were screened for eligibility prior to acceptance into the study. Exclusion criteria were as follows: (1) diagnosed with any psychiatric disorders, (2) history of brain injury or neurological conditions, (3) currently taking any prescribed medicines or drugs (including nicotine or caffeine within 2 hours), (4) currently pregnant. Eligible participants underwent four separate experimental protocols (sham, 808-nm, 852-nm, and 1064-nm stimulation) at least 48-hours apart using a random number generator to determine which protocol the participant would be receiving for each visit to ensure no bias or cross-effects. The study was approved by the institutional review board (IRB) at the University of Texas at Arlington and complied with all applicable federal NIH guidelines. Prior to starting experimental protocols informed consent was obtained from each participant.

4.2.2 Instrumentation

Sham and 1064-nm treatments were administered with a continuous-wave 1064-nm laser system provided by Cell Gen Therapeutics LLC, Dallas, TX (Model CG-5000) which is FDA-cleared for use on humans for relief of pain caused by inflammation. However, during sham stimulation the laser was set

to minimum power (0.1 W) and a black 3D-printed cover was used to block all light from actually reaching the participant. 808-nm and 852-nm continuous-wave lasers were custom built for experimental use. All non-sham protocols had their respective lasers set to 250 mW/cm^2 power density to ensure differences in power density were not a factor in the measured bb-NIRS results. This power density was also experimentally confirmed before each measurement using a power meter.

A single channel bb-NIRS system was used to measure chromophore changes *in vivo* during all experimental protocols (Fig. 9 B). This system consisted of a tungsten halogen lamp (Model 3900, Illumination Technologies Inc., East Syracuse, NY) as the light source and a spectrometer (QE PRO) light detector set 2 cm apart via 3.5 mm optical fiber bundles in a 3D-printed probe holder. A shutter was used to allow the light source to stay on between data acquisition periods without possibly influencing results by illuminating the forearm with broadband light. During data acquisition periods the broadband light diffuses through the forearm tissues to the detector fiber bundle which was then acquired and presented as a spectrum via laptop computer. The 3D-printed probe holder was affixed to the participants arm via double-sided tape to prevent motion artifacts caused by slight movement of the subjects.

4.2.3 Experimental Setup

Experiments were conducted in a locked room with all reflective surfaces removed. No external windows were present to pollute the spectrum with background light as well. A warning sign indicating a laser was in use inside was also used to prevent individuals without goggles from entering. Protective goggles (900–1000 nm: 5+ , 1000–2400 nm: 7+ ; 2900–10600 nm: 7+) were worn by everyone present in the room at all times and participants were instructed to close their eyes during the experimental protocols, this was both for added protection and to ensure true blinding to the type of PBM stimulation being given on a particular day. The 3D-printed probe holder was placed on roughly the same location on each participant's arm every protocol visit and affixed there with double sided tape. (Fig. 12 a) Each experimental protocol visit consisted of a 2-minute baseline followed by 8 cycles of 55-second blocks with the laser on and a 5-second block of data acquisition. This was then followed by a 5-minute recovery measurement after laser/sham stimulation had ceased. (Fig. 12 b) Data acquisition was performed in the same 5-second before the next minute manner for baseline and recovery periods as well to ensure consistency. 15 total data points were collected for each subject, however, the first 2 processed datapoints are used as a referenced zero point for each measurement.

Participants received no information on what laser or sham protocol they would be receiving on any given protocol visit. Laser/sham equipment was always set up after the participant was instructed to close their eyes to ensure true blinding. Prior to each measurement laser power density was ensured to be 250 mW/cm^2 using a power meter prior to the first data point and transmitted power through each participant's arm was acquired after the final datapoint was acquired by placing the power meter under the participant's arm and briefly firing the laser. Participants' arms were placed 2 cm from the aperture and were positioned so that the total depth of the arm penetrated was 2 cm as well for all 3 wavelengths to ensure uniformity.

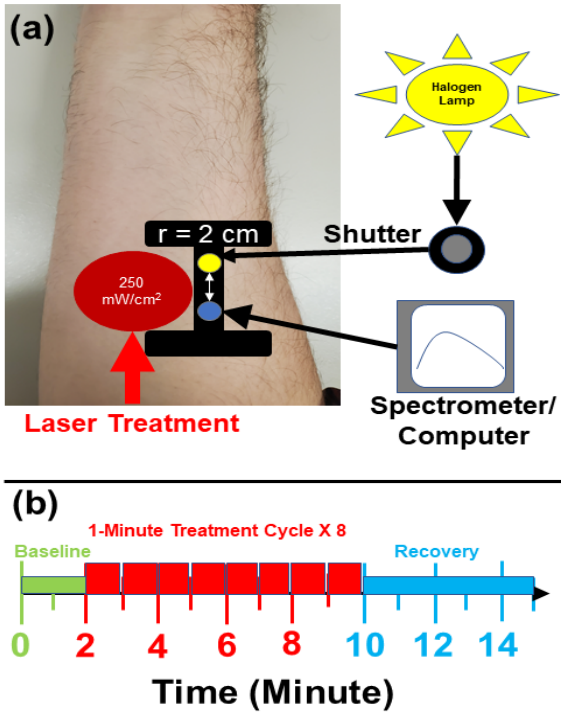

*Figure 12 Experimental Setup: **(a)** Configuration of the bb-NIRS probe holder (black I-shape). The I-shaped holder contains 2 optical fiber bundles with a center-to-center separation of 2 cm. One bundle (yellow) was connected to a tungsten halogen light source while the other bundle (blue) was connected to a QE Pro spectrometer attached to a laptop computer with a spectrum readout. The PBM laser stimulation was administered to the left side of the aperture at a power density of 250 mW/cm² (red circle). **(b)** Paradigm of the PBM/sham stimulation and interleaved bb-NIRS data collection. Each treatment protocol contains one 2-minute baseline (green), eight one-minute PBM/sham stimulation cycles (red) of 55 seconds laser on 5 seconds laser off for bb-NIRS data acquisition, and 5 minutes recovery time after the last PBM/sham cycle.*

4.2.4 Temperature and spectrum measurements

To ensure complete consistency between all laser wavelengths. Temperature measurements using an infrared thermometer were performed on a smaller group of subjects (n=4) to ensure temperature was not a factor in the differences seen between each laser. Stimulation and data collection were performed in the same interleaved fashion, but with only 1 baseline and 20 minutes of laser stimulation followed by 3 minutes of recovery. Spectrum consistency was also determined using a phantom block with the 3D-printed probe attached while each laser was on to ensure there were no abnormalities in each laser's spectral output.

4.2.5 Data Processing

The curve fitting algorithm previously reported in Wang et al [(Wang, Tian et al. 2016)] was used to perform chromophore extrapolation. Captured experimental spectrums were fitted between 750 and 900-nm to calculated [HbO], [Hb], and [CCO]. [HbT] was calculated afterward by adding calculated [HbO] concentration changes with calculated [Hb] concentration changes to determine the change in total hemoglobin concentration.

4.2.6 1064-nm data consistency

The previously acquired data reported in [Wang et. Al] was compared to the newly acquired 1064-nm data to ensure experimental repeatability. Although different spectrometer devices were used, the other experimental factors remain the same. This suggests that if this method of PBM stimulation and data collection were consistent the two sets of collected data should have very few significant differences.

4.2.7 Statistical Analysis

One-sample paired t-tests were used for temperature, transmitted power, and dataset comparisons to determine significant ($p<0.05$) differences between datasets and placebo. Time dependent repeated measurement ANOVA was performed on each protocol group (sham, 808-nm, 852-nm, and 1064-nm) time points to determine time-wise significance between groups. Timepoints that were 2 standard deviations from the mean were removed as outliers to remove measurement artifacts and preserve subjects due to the small number of subjects and inability to collect more data.

4.3 Results

4.3.1 Laser spectrum analysis

The spectral reading for each laser is presented below in Fig. 13. Each laser spectrum exhibits a very narrow band with the maximum peak at the appropriate wavelength (1064-nm, 852-nm, and 808-nm for their respective laser devices). This spectrum data suggests that most of the chromophore concentration changes seen in the bb-NIRS data are due to exclusively the desired wavelengths with no spectral crossover.

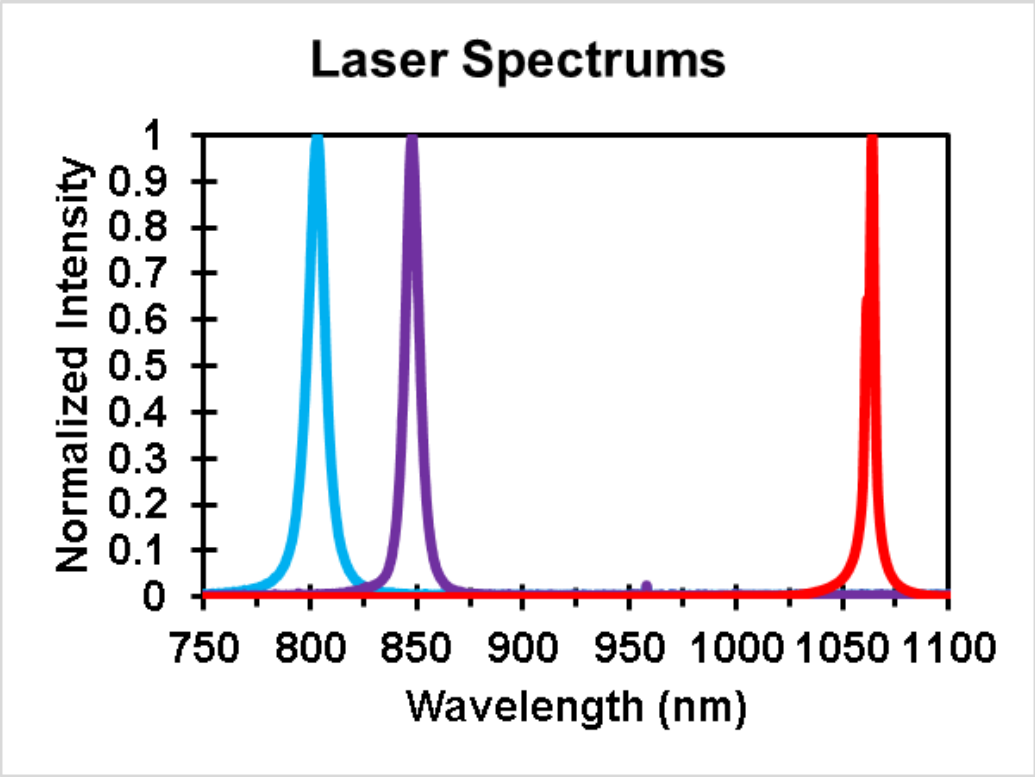

Figure 13 *Spectrum data captured from QE Pro for: 1064-nm (red), 852-nm (purple), and 808-nm (blue) in a solid phantom environment. Intensity value was acquired in photon counts and normalized to the maximum value of each acquired spectrum.*

4.3.2 Transmitted Power Analysis

The transmitted power through the group averaged individuals' arms before each measurement are presented below in figure 14. 1064-nm laser light transmits almost twice the amount of power through the participants' arms when compared to 852-nm and 808-nm laser light at the same 250 mW/cm

power density. There is no significant difference ($p < 0.05$) between 852-nm and 808-nm transmitted power, however.

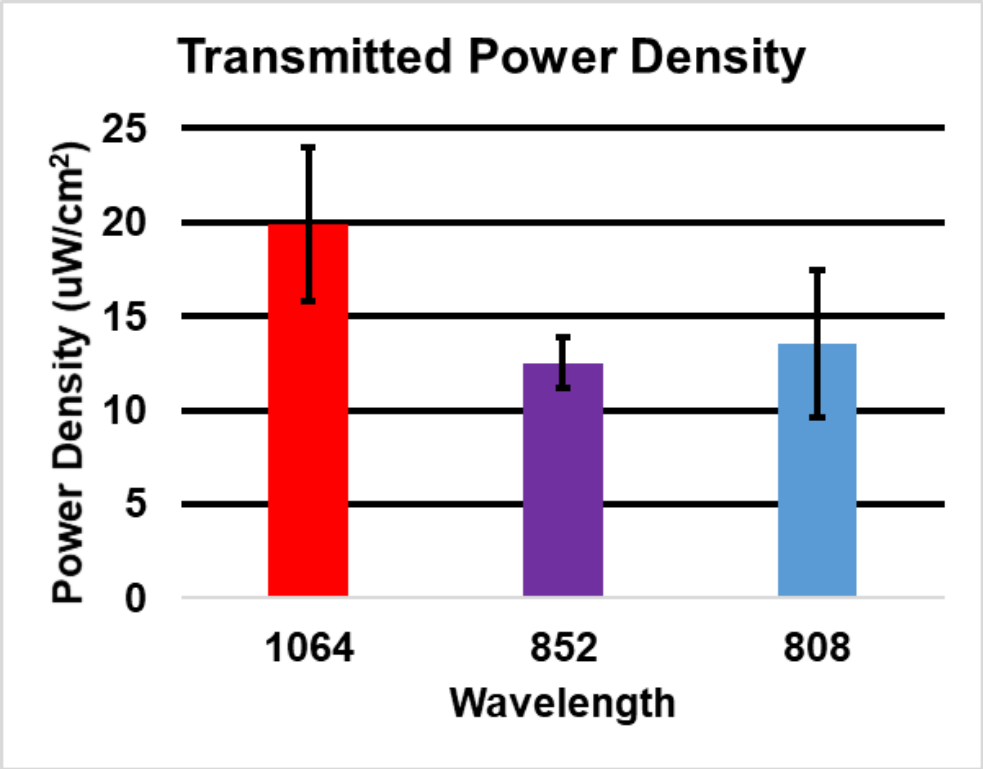

Figure 14 *Acquired transmitted power through the arm for 1064-nm (red), 852-nm (purple), and 808-nm (blue). The data is represented in power density with standard error displayed.*

4.3.3 Skin temperature increase

Thermal data collected on the skin of (n=4) participants shows no significant ($p<0.05$) difference between the three groups in temperature increase induced

on the skin between the 3 laser groups. This indicates that the thermal effect induced by each laser at 250 mW/cm^2 is roughly the same between all three wavelengths. Any changes seen in chromophore concentrations can be seen as independent from temperature increase, at least on the surface.

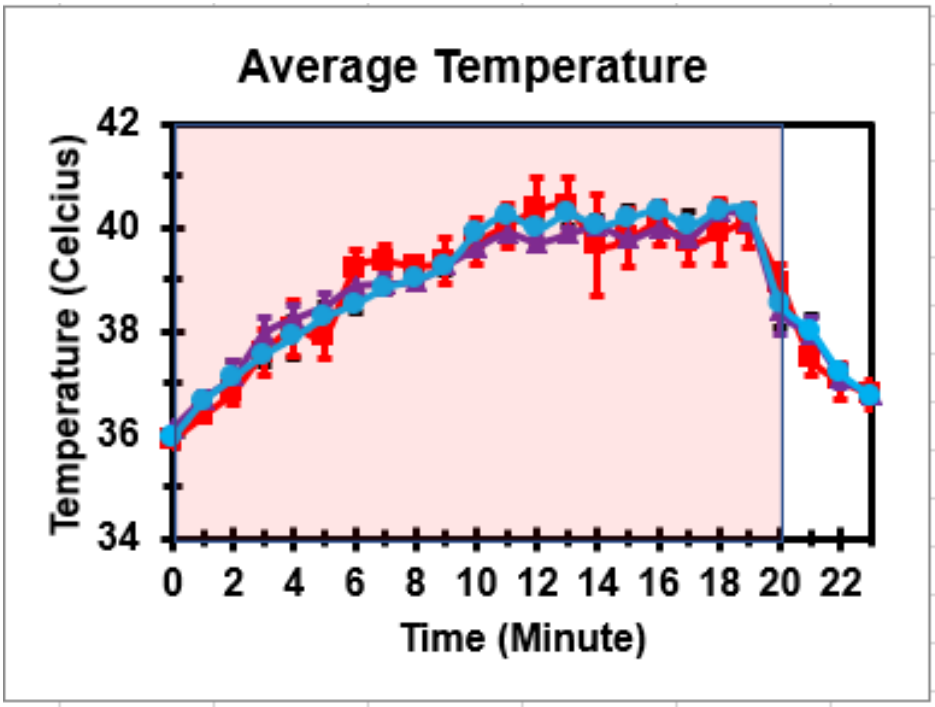

Figure 15 *Acquired skin temperature data for 1064-nm (red), 852-nm (purple), and 808-nm (blue) laser PBM. The stimulation period is indicated by the transparent red box overlaying the graph. Initial baseline is indicated by timepoint 0 and recovery temperature readings are indicated as the timepoints outside of the stimulation period.*

4.3.4 Comparison of previously acquired data to newly acquired data

The newly acquired and previously acquired data reported in Wang et al, presented below in Fig. 16, shows there is very little difference between the two datasets. Although these datasets were collected at different times, with different spectrometers, and with different subject populations there are no significant ($p<0.0\text{-}5$) differences in 1064-nm PBM stimulation or placebo groups when compared with repeated measures ANOVA.

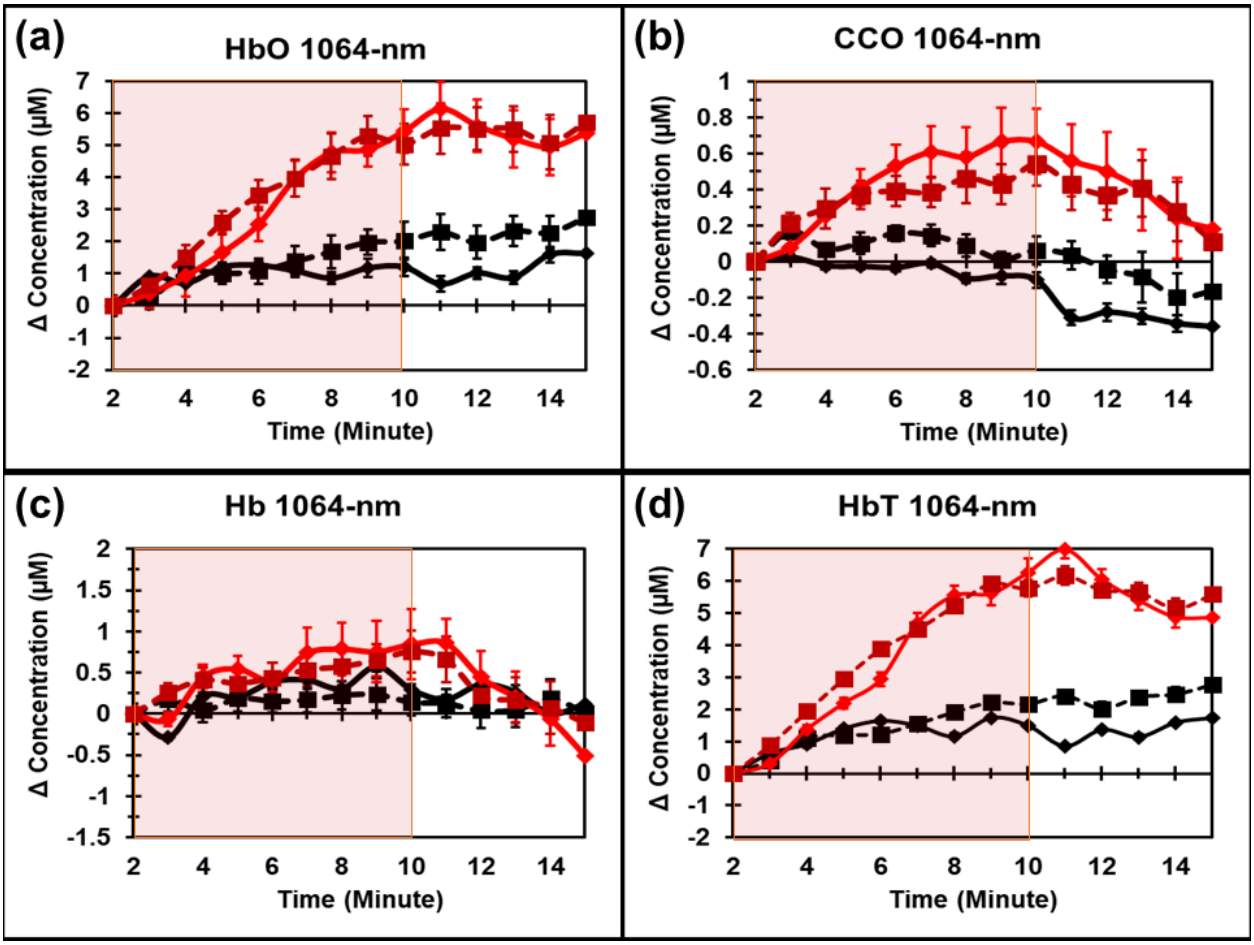

Figure 16 *Previously acquired data from Wang et. Al (dashed lines) and newly acquired data (solid lines) for the change in the chromophores of [HbO] (a), [CCO] (b), [Hb] (c), and [HbT]. 1064-nm Stimulation (red) and sham (black) protocol groups are shown with error bars.*

4.3.5 Chromophore concentration changes under three different wavelengths

4.3.5.1 1064-nm

Figure 17 below shows the results of comparing chromophore concentration changes of both the sham treatment group and the 1064-nm PBM treatment group. [HbO] (a) increases significantly ($p<0.05$) in the stimulation epoch and remains significantly elevated post-stimulation when compared to sham. [CCO] (b) increases during stimulation and remains significantly ($p<0.05$) elevated during the post-stimulation epoch when compared to sham as well. [Hb] (c) does not significantly differ from sham during stimulation or post-stimulation epochs. [HbT] (d) significantly ($p<0.05$) increases in both stimulation and remains significantly elevated post-stimulation.

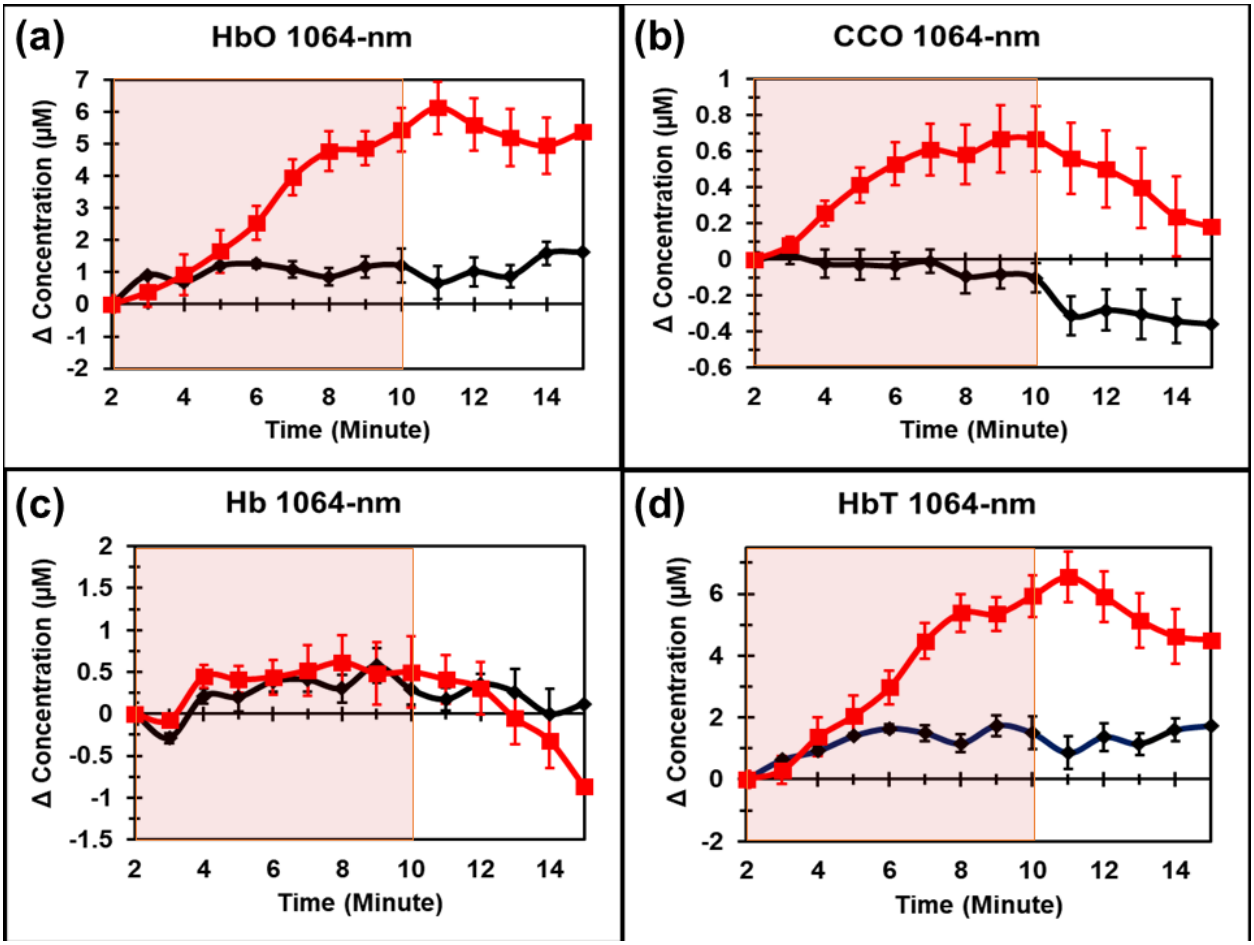

Figure 17 *Protocol group-wise averaged data for sham (black) and 1064-nm (red), Stimulation epoch is indicated with red shading while post-stimulation epoch remains unshaded. Lines displayed are the change in the concentration of the chromophores of [HbO] (a), [CCO] (b), [Hb] (c), and [HbT] (d).*

4.3.5.2 852-nm

Figure 18 below shows the results of comparing chromophore concentration changes of both the placebo treatment group and the 852-nm PBM treatment group. [HbO] (a) does not significantly ($p<0.05$) increase in either the stimulation or post stimulation epochs. [CCO] (b) significantly decreases during stimulation and remains reduced during the post-stimulation epoch when compared to sham as well. [Hb] is significantly ($p<0.05$) increased significantly differ from placebo during stimulation or post-stimulation epochs. [HbT] (d) significantly ($p<0.05$) increases during both stimulation and post-stimulation epochs.

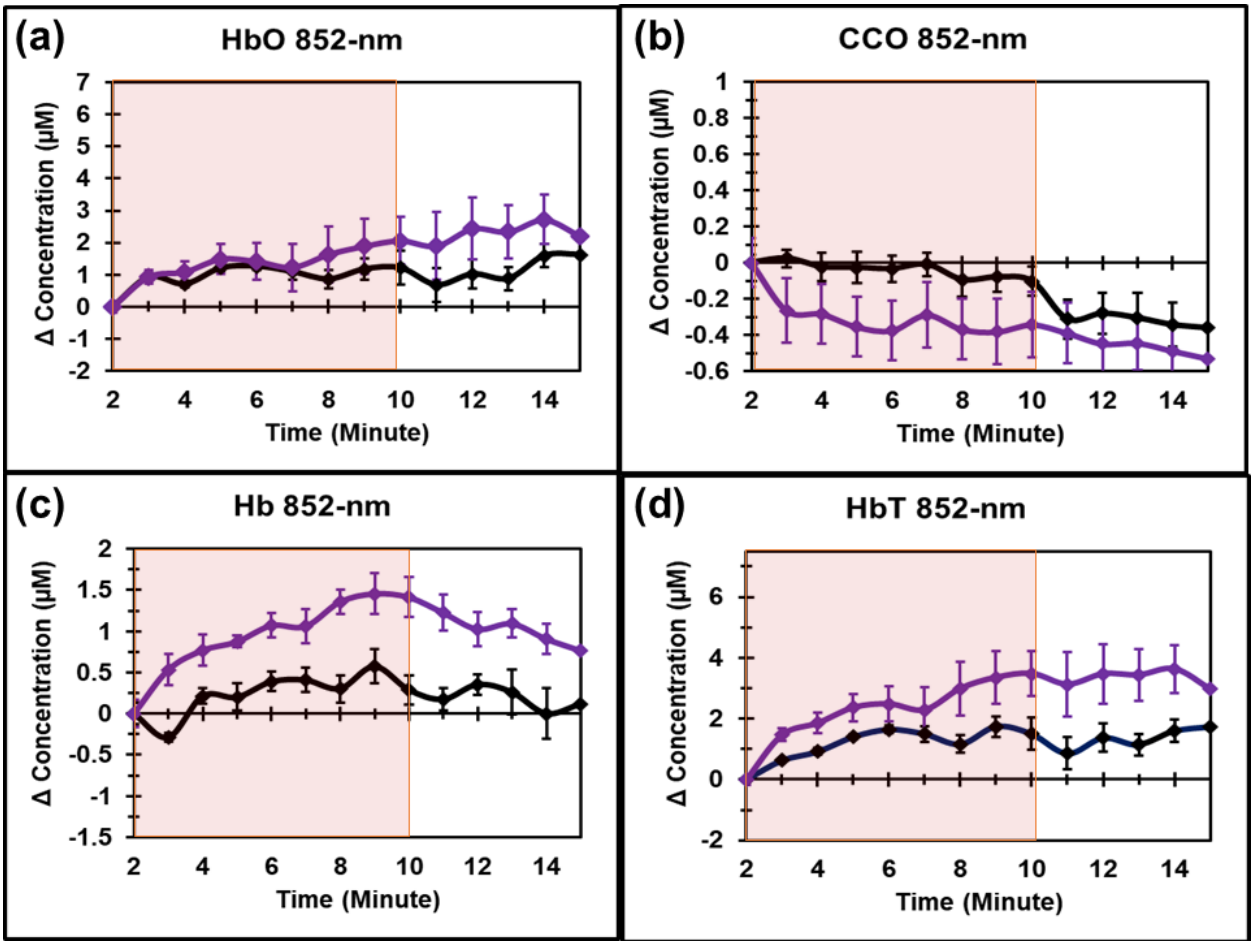

Figure 18 *Protocol group-wise averaged data for sham (black) and 852-nm (purple), Stimulation epoch is indicated with red shading while post-stimulation epoch remains unshaded. Lines displayed are the change in the concentration of the chromophores of [HbO] (a), [CCO] (b), [Hb] (c), and [HbT] (d).*

4.3.5.3 808-nm

Figure 19 below shows the results of comparing chromophore concentration changes of both the placebo treatment group and the 808-nm PBM treatment group. [HbO] (a) decreases significantly ($p<0.05$) in the post treatment epoch when compared to placebo. [CCO] (b) increases during stimulation and continues increasing significantly ($p<0.05$) during the post-stimulation epoch when compared to placebo as well. [Hb] (c) does not significantly differ from placebo during the post-stimulation epoch. [HbT] (d) significantly decreases during

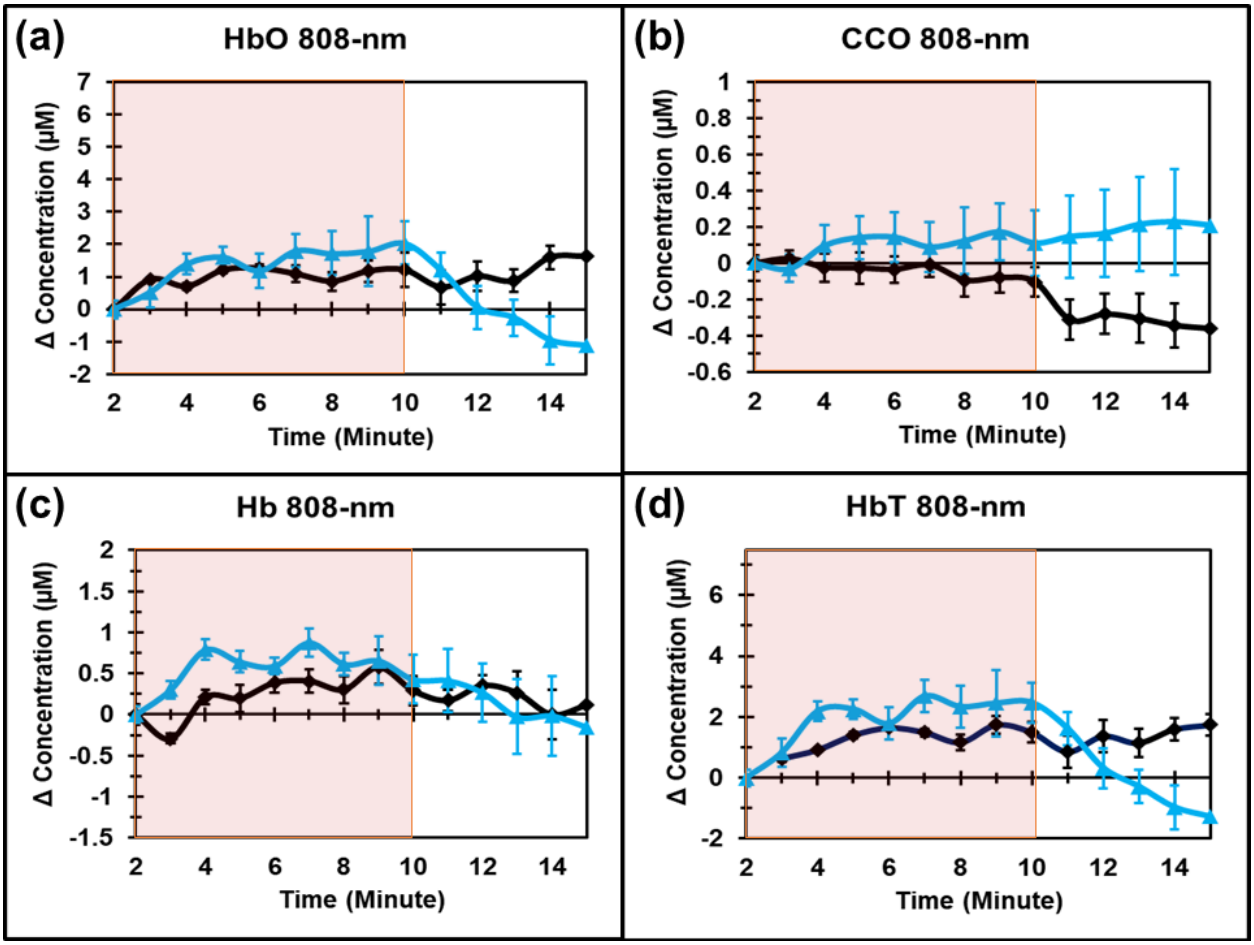

Figure 19 *Protocol group-wise averaged data for sham (black) and 808-nm (blue), Stimulation epoch is indicated with red shading while post-stimulation epoch remains unshaded. Lines displayed are the change in the concentration of the chromophores of [HbO] (a), [CCO] (b), [Hb] (c), and [HbT] (d).*

4.3.6 Epoch averaged data

Figure 20 below represents the epoch averaged concentration change in chromophores for [HbO] (a), [CCO] (b), [Hb] (c), and [HbT] (d). Sham stimulation data is fairly consistent for all 4 chromophores over time, but the PBM stimulation protocol groups present unique trends. 1064-nm presents a constant increase in [HbO] and [HbT], while CCO increases during stimulation and begins to slowly return to baseline. 852-nm presents a consistent increase in [HbO], [Hb], and [HbT] while also showing a consistent decrease in oxidized [CCO] concentration. 808-nm has an initial increase in [HbO], [Hb], and [HbT] with a decrease after stimulation ends. However, 808-nm stimulation causes a consistent increase in [CCO] during and post stimulation suggesting a slower [CCO] oxidation mechanism.

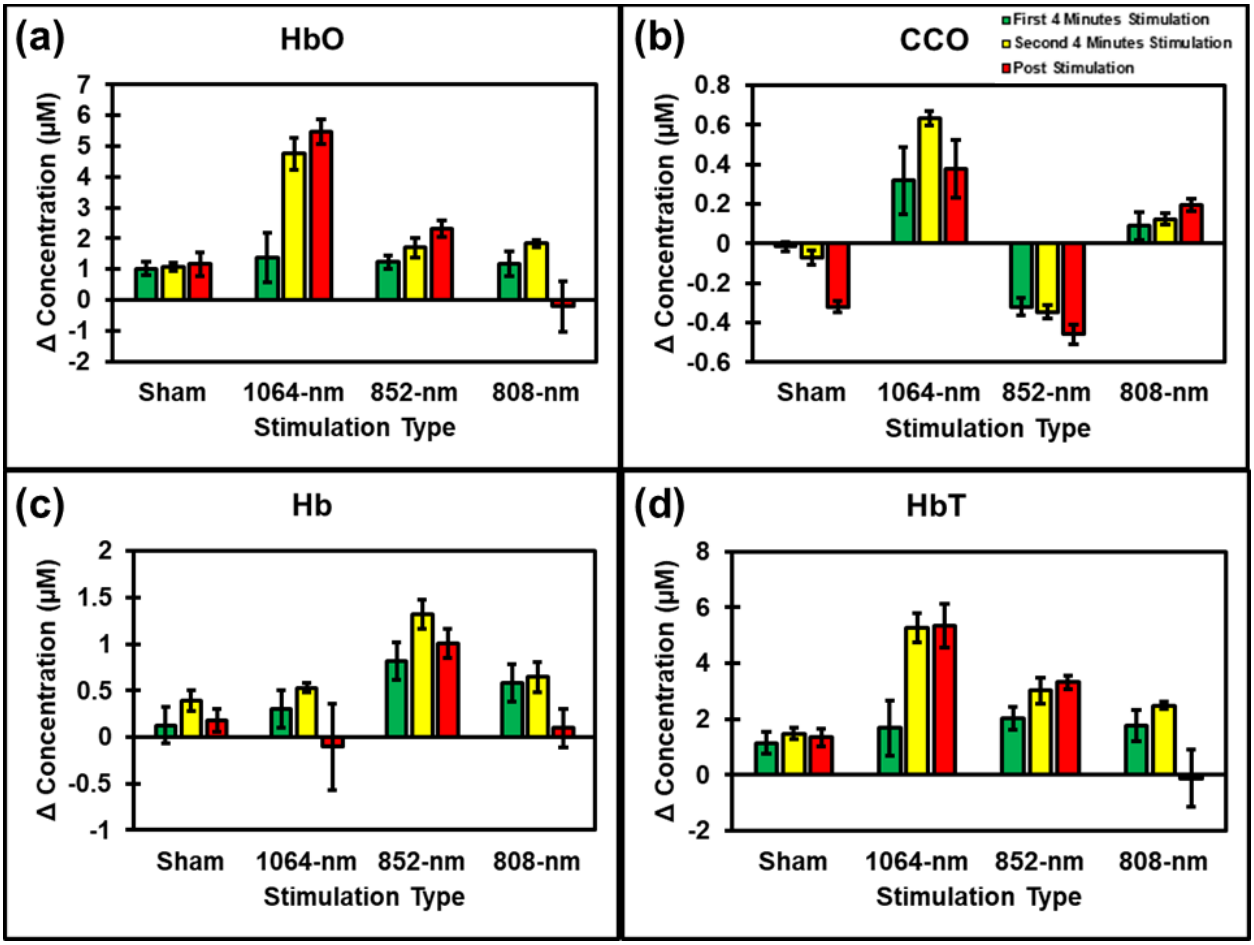

Figure 20 *Protocol group-wise averaged data for sham, 808-nm, 852-nm, and 1064-nm data for the first 4 minutes of stimulation (green), second 4 minutes of stimulation (yellow), and post stimulation (red). Bars displayed are the change in the concentration of the chromophores of [HbO] (a), [CCO] (b), [Hb] (c), and [HbT] (d). Standard deviation is represented by the error bars present above each bar graph.*

4.3.7 Repeated measures ANOVA analysis

Repeated measures ANOVA was used to determine significant interactions between various independent variables in the collected datasets. Table 1 below provides p-value information about the 1064, 852, and 808-nm wavelengths when compared to the sham stimulation protocol using this repeated measures ANOVA for both stimulation (a) and post-stimulation (b) epochs. 1064-nm light was found to be significantly ($p<0.05$) higher than sham in all measured chromophores except [Hb] in both stimulation and post-stimulation. 852-nm light significantly increased [Hb] and [HbT] during and post-stimulation but was also found to significantly decrease [CCO] concentration during both epochs. 808-nm significantly decreased [HbO] and [HbT] while significantly increasing [CCO] concentration post-stimulation. During stimulation 808-nm significantly increased [Hb] and [HbT] concentration.

Chromophore	1064-nm	852-nm	808-nm (a)
HbO	0.02	0.81	0.23
CCO	0.00	0.00	0.29
Hb	0.52	0.00	0.00
HbT	0.00	0.00	0.04
Chromophore	**1064-nm**	**852-nm**	**808-nm (b)**
HbO	0.01	0.12	0.02
CCO	0.00	0.00	0.01
Hb	0.12	0.00	0.46
HbT	0.00	0.01	0.01

Table 1 *Repeated measures ANOVA data for the change in concentration of [HbO], [CCO], [Hb], and [HbT] when compared to sham stimulation during stimulation (a) and post-stimulation (b). p-values in red are significantly higher than sham while p-values in blue are significantly lower. Non-significant (p>0.05) values are indicated in black.*

4.4 Discussion

4.4.1 Non-wavelength dependent effects

Careful steps were taken to ensure only wavelength dependent effects were inducing different effects seen in chromophore dependent effects between wavelengths. Laser spectrums were determined to be compact and consistent over time (Fig. 13) meaning laser effect is predominantly only the desired wavelength. It has also been speculated that temperature is the main driver for 1064-nm PBM's effects [(Hamblin 2018)]. However, our temperature data between the three wavelengths (Fig. 20 (b)) shows no significant difference between groups. This indicates that any effect seen between wavelength groups is purely reliant on the wavelength of light itself and not the temperature effects. One key difference between wavelengths is the transmitted power (Fig. 14) that shows 1064-nm data is significantly higher than the other two wavelengths.

4.4.2 1064-nm data is highly reproducible when comparing previously collected data to newly collected data

Previously collected data by Wang et al.[(Wang, Tian et al. 2016)] was compared to the new collected data from this study to prove reproducibility (Fig. 16). Though the data was collected at different times with different equipment, the 1064-nm treatment groups were found to have no significant ($p < 0.05$) difference in the change in concentration for [HbO], [Hb], [CCO], or

[HbT]. These data are consistent with previously published data using tPBM results as well [(Pruitt, Wang et al. 2020)]. The data were also subjected to repeated measures ANOVA and found to have no significant difference when using this more rigorous test as well. This indicates that the effects of PBM are highly consistent in subject populations regardless of equipment sensitivity or operator data collection variance.

4.4.3 1064-nm provides the strongest increase in the concentration of both [HbO] and [CCO]

1064-nm's increase of [HbO], [HbT], and [CCO] are well documented [(Holmes, Barrett et al. 2019)], but similar effects are also seen in many studies involving 850 and 810-nm light stimulation [(de Oliveira, Vanin et al. 2017)]. What these studies lack is the direct comparison between these wavelengths at the same power density, which we have accomplished in this study. 1064-nm laser is shown to have the highest increase in the concentration of [HbO] as well as [CCO] (Fig. 17) when compared to these other wavelengths at the same power density. This is possibly due to 1064-nm increased power transmittance through tissue (Fig. 14), however the bb-NIRS probe used in this study can only detect a depth of 1 cm making deep tissue effects unlikely.

4.4.4 Proposed Mechanistic Pathway of Multi-Wavelength Photobiomodulation

Throughout various cellular PBM studies there are 2 membrane proteins that are often discussed as possibly contributing to the effects produced by the most popular wavelengths, transient receptor potential cation channel subfamily V member 1 (TRPV1) [(Pigatto, Silva et al. 2019)] and CCO [(Hamblin 2018)]. TRPV1 is often used in the body's heat regulation and the sensing of heat [(Tominaga and Tominaga 2005)] but it was also found to also react to various other stimuli such as capsaicin [(Shuba 2020)] which are known to generate a sense of warmth. These TRPV1 channels have also been called photothermal channels, however, skin temperature for all 3 wavelengths was on average 39 to 41 degrees Celsius (Fig. 4-4) which is below the supposed 43 degrees Celsius activation threshold [(Smutzer and Devassy 2016)]. 810-nm light was also found to not induce calcium influx into cells [(Wang, Huang et al. 2017)]. These findings suggest that 808-nm light does not activate these supposed photothermal channels even though the same amount of heat is generated when compared to other wavelengths.

CCO drives the electron transport chain to its final complex ATPase to generate ATP. During this process it generates ROS, ADP, and water by accepting either Cytochrome C or nitric oxide (NO) [(Taylor and Moncada 2010)]. Nitric oxide is used as the rate limiting molecule in this scenario due to the ion gradient between the inner and outer membrane that drives the process forward [(Aguirre, Rodríguez-Juárez et al. 2010)]. Although within the range of CCO's absorbance spectrum 900-nm light inhibits CCO function [(Sanderson, Wider et al. 2018)]. With the CCO inhibition seen by this study as well as those seen by other studies as well [(Wang, Huang et al. 2017)] it is reasonable to hypothesis that 852-nm also exhibits this inhibition effect rather than activation.

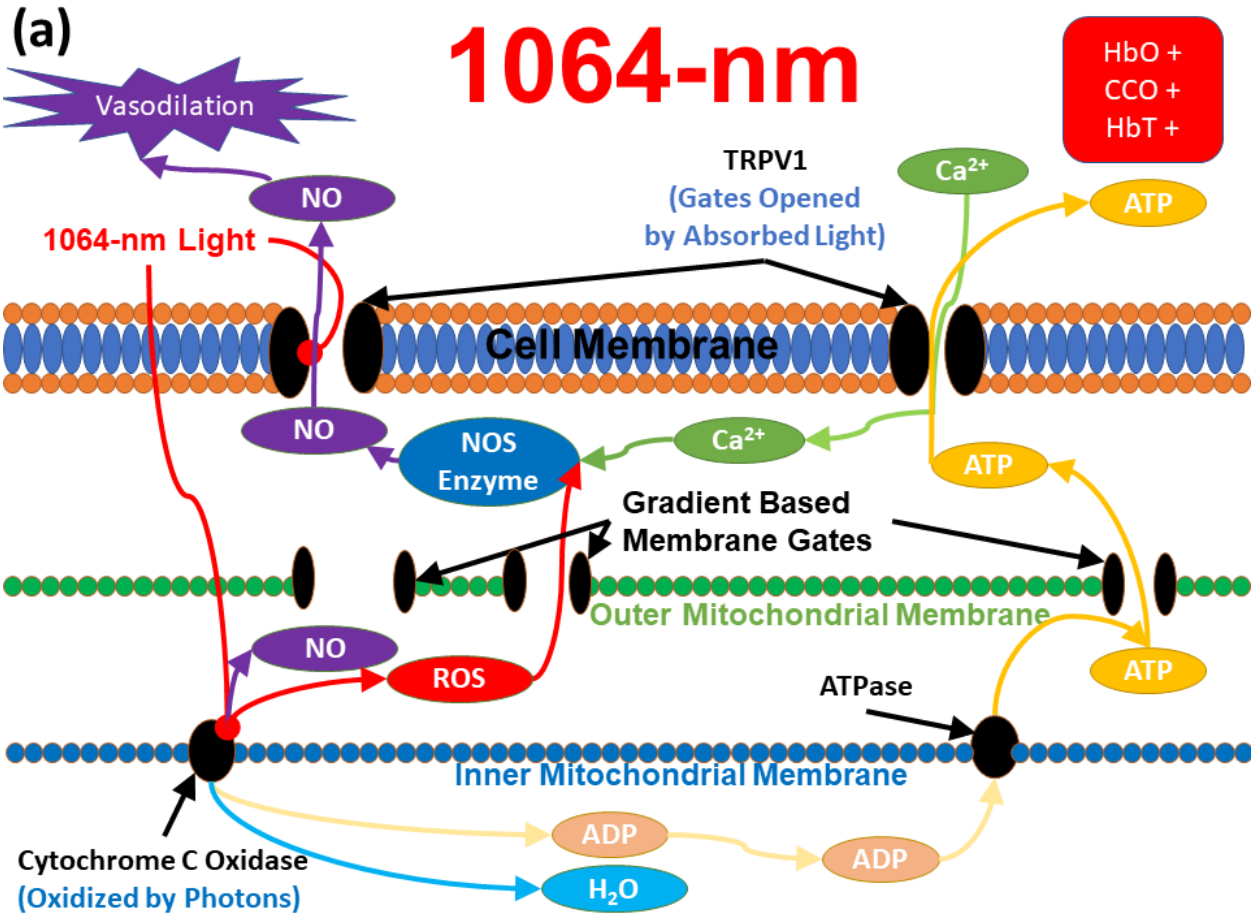

Figure 21 *Mechanistic diagram of the hypothesized cellular action of 1064-nm PBM on an endothelial cell. The endothelial PBM mechanism featured here would be the main driving force behind PBM effects measured during and after light stimulation. All cellular gates and enzymes are colored black for simplicity. Important molecules are color coded: NOS (blue), Ca^{2+} (green), ROS (red), NO (purple), ADP (orange), and ATP (yellow). Arrows are color coded with their respective molecule to indicate their path through the cell or an interaction.*

1064-nm PBM exhibits both NO release and CCO oxidation effects when measured with bb-NIRS in this study and in others [(Usumez, Cengiz et al.

2014)]. Due to this repeatably measured phenomenon it is a reasonable assumption to conclude both TRPV1 and CCO have strong absorbance interactions with this wavelength. With this basic assumption we can generate a mechanistic model for 1064-nm that accounts for the major signaling molecules in the body Ca^{2+}, NO, and ATP (Fig. 21). While both TRPV1 is open and CCO is oxidizing this will create a negative ion gradient within the cell pulling in more extracellular Ca^{2+}. Due to increased demand for oxygen consumption NO will also be pulled into the inner mitochondrial membrane to act as a substitute for Cytochrome C [(Brown 2001)]. This, in turn, will generate more ROS which will make their way into the cytosol via ion gradient gated channels around the outer mitochondrial membrane. When both Ca^{2+} and ROS are present in the cytosol there are multiple nitric oxide synthase enzymes that can convert the positive charge from the calcium onto the reactive oxygen species present in the cytosol to create NO. This NO can then leave the cell to signal vasodilation or continue the cycle of creating more ADP and ROS by returning to CCO in the inner mitochondrial membrane. This series of events ensure vasodilation occurs, but a neutral ion gradient is maintained within the cell due to the influx of ROS and Ca^{2+} into the cytosol which prevents a significant amount of O_2 from hemoglobin to be absorbed by the cell. The culmination of this pathway is an increase in extracellular [HbO] and [HbT], while increasing the rate at which CCO is oxidized.

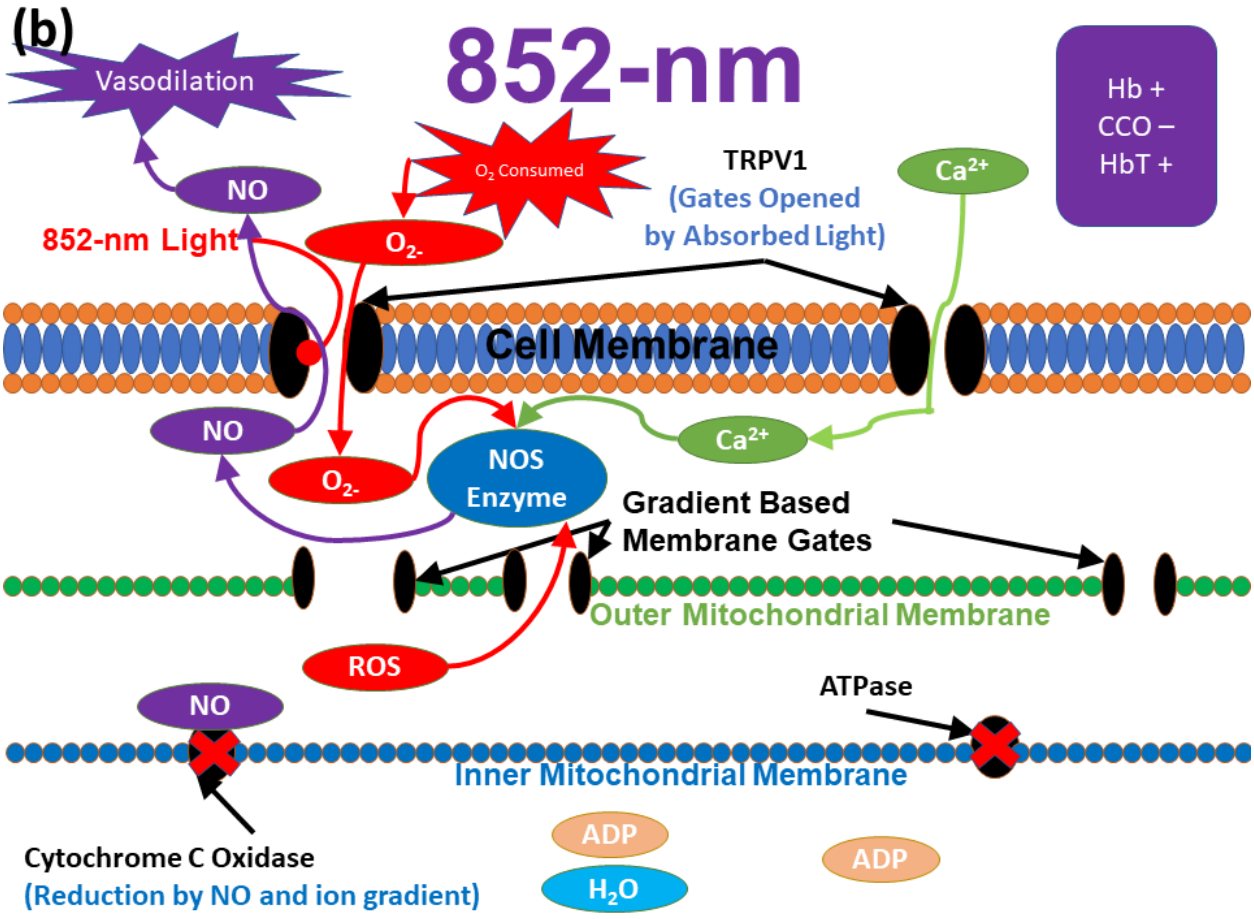

Figure 22 *Mechanistic diagram of the hypothesized cellular action of 852-nm PBM on an endothelial cell. The endothelial PBM mechanism featured here would be the main driving force behind PBM effects measured during and after light stimulation. All cellular gates and enzymes are colored black for simplicity. Important molecules are color coded: NOS (blue), Ca^{2+} (green), ROS (red), NO (purple), ADP (orange), and ATP (yellow). Arrows are color coded with their respective molecule to indicate their path through the cell or an interaction.*

Assuming 852-nm light has strong interaction with TRPV1 and inhibitory effects on CCO we can also hypothesize a pathway that accommodates Ca^{2+}, NO, and ATP (Fig. 20(b)). With TRPV1 activated and CCO inhibited NO would begin building up in the cell along with Ca^{2+} [(Tarasov, Griffiths et al. 2012)]. With this positive gradient in the cytosol ROS will be pulled from the mitochondria, which will further inhibit CCO. NO escaping the cell due to its inability to be metabolized will cause vasodilation in the surrounding endothelial cells[(Oishi, De Moraes et al. 2017)]. This ultimately increases blood flow but will quickly utilize the O_{2^-} ROS from circulated HbO to produce more NO due to CCO's inhibition.

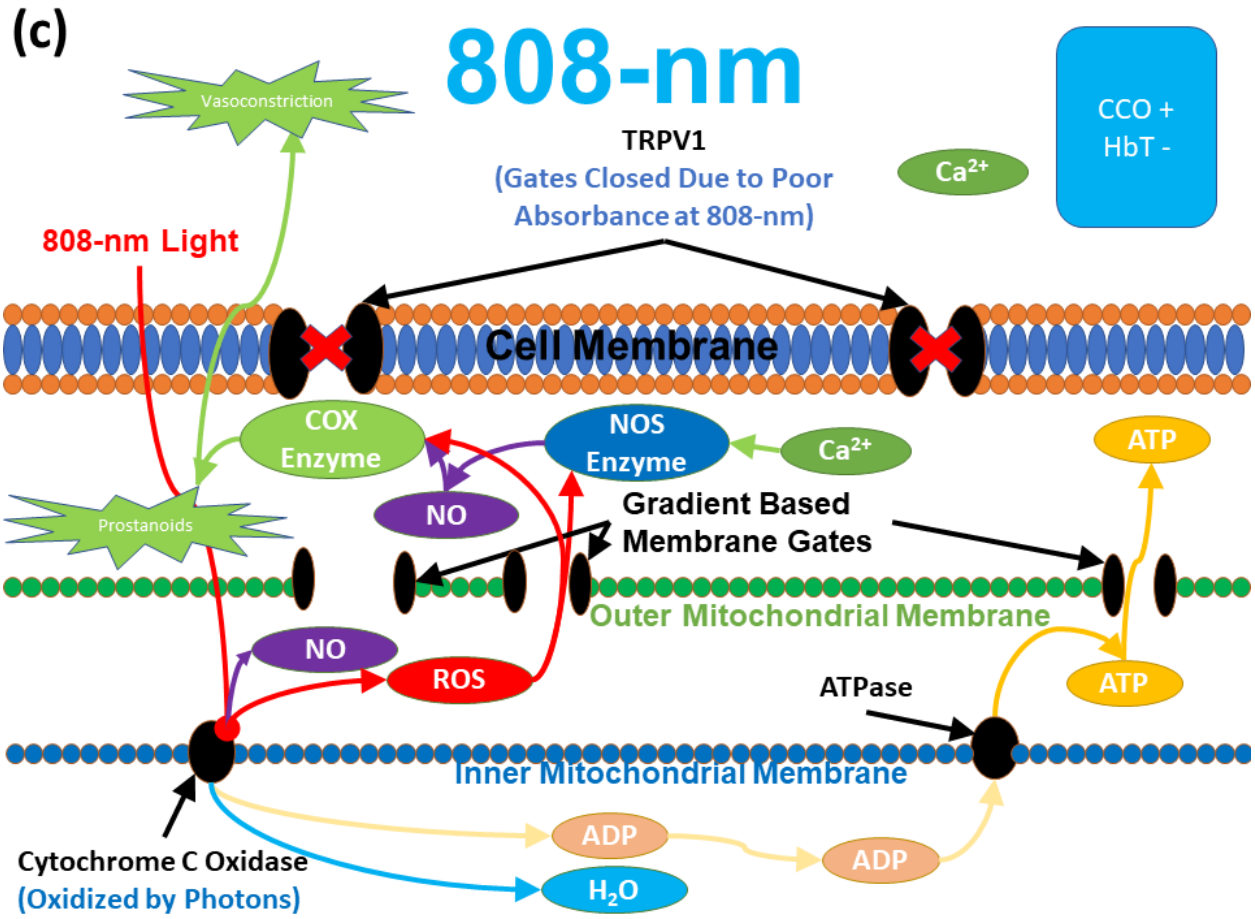

Figure 23 *Mechanistic diagram of the hypothesized cellular action of 808-nm PBM on an endothelial cell. The endothelial PBM mechanism featured here would be the main driving force behind PBM effects measured during and after light stimulation. All cellular gates and enzymes are colored black for simplicity. Important molecules are color coded: NOS (blue), Ca^{2+} (green), ROS (red), NO (purple), ADP (orange), and ATP (yellow). Arrows are color coded with their respective molecule to indicate their path through the cell or an interaction.*

The peak absorption range of CCO is thought to be from 600 to 810-nm from red to just inside the near infrared range. However, due to the absorption properties of red light outside of cellular studies the 810-nm end of the

spectrum is preferred for *in vivo* studies [(Rupel, Zupin et al. 2018)]. This wavelength is just within the range thought to activate TRVP1, but in practice has been found to exhibit little evidence to support this in measured biomarkers [(Wang, Huang et al. 2017)]. So, if we reasonably assume only CCO is oxidized by 810-nm light a third pathway can be visualized to account for Ca^{2+}, NO, ATP, as well as the chromophore concentration changes (Fig. 20 (c)). With CCO in a constantly oxidized state NO will be metabolized as before, but due to TRPV1 channels not being open to the extracellular space intracellular Ca^{2+} and ROS will be used at an increased rate with only slower cell membrane channels [(Duchen 2000)] to fulfill the growing metabolic demand. With this buildup of ROS and NO within the cytosol, cyclooxygenase (COX) enzymes will be activated to produce constrictive prostaglandins and materials for ATP production [(Silva, Pernomian et al. 2017)]. This would lead to the lagged response in CCO seen in our data (Fig. 19) due to insufficient materials to perform ADP creation during the start of PBM stimulation as well as the lower [HbT] concentration due to increased extracellular NO consumption causing vasoconstriction [(Yu, Shahid et al. 2010)] as well as COX producing constrictive prostaglandins known to constrict blood vessels [(Silva, Pernomian et al. 2017)]. Due to the short length of time, we are actually recording the subject and the constant increase of [CCO] oxidation even after stimulation it is probable that this mechanism of solely 808-nm stimulation requires some time

to take effect. 808-nm light has been proven in cellular studies to generate ROS and prostaglandins during the initial stimulation period and shortly after. However, at the 1-hour timepoint and beyond 808-nm stimulation was found to have the inverse effect with a dramatic increase in NOS concentration as well as NO production [(Amaroli, Ravera et al. 2019)]. This starting ROS and COX stimulation likely leads to the increase in NOS activity later due to the sudden oxidative stressors within the cell being removed but NOS concentration increase. As the *in vivo* data we collected is most likely during this initial oxidative stress phase the vasoconstriction see would not be unusual.

4.4.5 Limitations and future work

While this study was able to prove data reproducibility with previously collected data and collect some meaningful results our sample size was quite small due to COVID-19 restrictions on continuing human subject data collection (n=10). Temperature data was collected on an even smaller population (n=4) albeit for multiple measurements. With more individuals' data certain trends might change, especially in the sham stimulation group where variance is almost purely random or movement noise.

Also, with only a 1 cm penetration depth with a 2 cm probe we cannot detect deeper effects where 1064-nm light may be more effective due to its deeper penetration depth. Bb-NIRS is also extremely affected by movement noise which due to the smaller sample size may exacerbate variance between individuals.

4.5 Conclusions

The data collected in this study has reinforced the reproducibility of bb-NIRS data collection by providing a stringent statistical analysis of newly versus previously collected data. This as well as other studies using bb-NIRS to examine transcranial PBM effects on the head firmly cement bb-NIRS as a both reliable and effective tool for measuring chromophore concentration change in the future.

This study has also examined multi-wavelength PBM effects *in vivo* on a level not seen before in other studies making the novelty and value of the collected data high. With vascular and intracellular data collected (*** correct?) in tandem the distinct difference between the effects of even slight changes in wavelength can influence the effects of PBM. With these subtle differences examined in detail the intracellular mechanisms behind the effects can be

hypothesized with greater certainty. I have proposed 3 semi-novel pathways to distinguish PBM's effects caused by different wavelengths. Namely, based on previously proposed mechanisms of PBM thought to be under two separate umbrellas of either CCO-oxidized or heat-regulated pathways, I considered both pathways being enabled concurrently by light activation partially because of varied absorbance spectra at respective wavelengths. Accordingly, a more complete model can be created that accounts for the great variance among PBM-induced outcomes and further to enable quantitative prediction of PBM-based treatments for clinical applications in the future.

4.6 Disclosures

No conflicts of interest, financial or otherwise, are declared by all the authors.

4.7 Acknowledgements

This work was supported in part by the National Institute of Mental Health/National Institutes of Health under the BRAIN Initiative (RF1MH114285). We also acknowledge the support in part from the STARS program by the University of Texas System. The authors would like to thank

Nahiyan Mahbub, Meet Bhat, and Aliya Anil for their assistance with human data collection.

Chapter 5 : Investigation of 1064-nm laser fluence in tissue phantoms for quantitative analysis of photobiomodulation

Tyrell Pruitt, Xinlong Wang, Hasan Parvez, and Hanli Liu

(This chapter is a manuscript that will be submitted soon)

5.1 Introduction

Transcranial Photobiomodulation is a growing area of interest in the fields of both neuroscience [(Passarella and Karu 2014)] and clinical treatment of neurodegenerative diseases [(Eells, Henry et al. 2003)]. Photobiomodulation, put simply, is the altering of both cellular and tissue level function of the body by using specific wavelengths of light to interact with photosensitive structures such as cytochrome C oxidase [(Poyton and Ball 2011)]. One of the most commonly used wavelengths of light used for these purposes is 1064 nm [(Peplow, Chung et al. 2011)], which has been shown in many studies to produce a significant change in the functionality of neuronal tissue [(Wang, Reddy et al. 2018)]. However, the mechanisms behind this altered function and the exact

dosage of light needed to generate a significant change have been largely overlooked in favor of more clinical human studies [(Cassano, Petrie et al. 2016)].

These mechanistic details, although not important for overall treatment effect, could be very important in creating a dosing schedule for applications requiring repeated treatments such as the treatment of major depressive disorder [(Salehpour and Rasta 2017)]. This application could greatly benefit from the knowledge of fluence generated by a light source in order to sufficiently "dose" areas of the brain often associated with neurological disorders [(Hamblin 2016)].

Neuronal disorders, such as Alzheimer's disease, are often linked back to a loss of electron transport chain function in the mitochondria of otherwise healthy cells due to the buildup of harmful substances such as Aβ plaques [(Manczak, Anekonda et al. 2006)]. In fact, one of the earliest detectable symptoms linked to early-stage neurological disorders is impairment or loss of mitochondrial function [(Du, Guo et al. 2010)]. With the application of proper light dosage in photobiomodulation, light-based therapy has been found to significantly reduce the toxic burden of cytochrome C oxidase in cellular cultures and restore healthy mitochondrial function [(Wong-Riley, Liang et al. 2005)]. With proper research into the many factors that affect light propagation throughout the brain,

photobiomodulation could become an invaluable tool in combatting numerous age-related neuronal disorders.

5.2 Materials and methods

5.2.1 Instrumentation and experimental setup

The primary goal of this experiment was to examine the fluence of 1064 nm light under both different optical conditions as well as with different power variations of the laser device itself. To accomplish these goals a liquid tissue phantom was used to simulate organic media consisting of different optical properties and 3D-printed lens apertures were created to control the power density of the 1064 nm laser. A 20% intralipid solution was diluted to varying concentrations to act as the photon scattering agent in this tissue phantom, and either ink or horse blood was used as the photon-absorbing agent in the phantom.

In order to accurately determine the optical properties of the tissue phantom, an ISS Oximeter was used to measure both the mean scattering coefficient, μ_s', and the absorption coefficient, μ_a, at the wavelength of 750 nm. This particular wavelength was chosen due to its fairly distinct absorption in water, oxygenated hemoglobin, and deoxygenated hemoglobin which allows for a fairly stable value

to be determined for these optical properties regardless of the photon-absorbing agent used. Using this methodology, the various different optical conditions of the tissue phantom can be replicated any number of times to allow for consistent and comparable results.

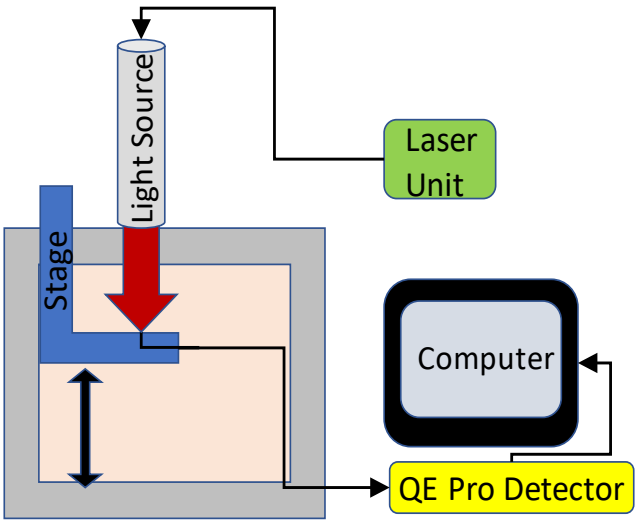

Figure 21 *Schematic of the overall experimental setup. This experimental setup was used as the base for every experiment regardless of the change in aperture size or laser wavelength. Pictured are the laser unit that powered the light source, the light source itself, the liquid tissue phantom with an attached 1-D translational stage, the detector fiber attached to the QE Pro spectrometer, and the computer that the acquired QE Pro spectrometer data is eventually stored.*

Regardless of the phantom or aperture used in each experiment, the laser source was suspended 2cm above the surface of the tissue phantom using a clamping system and a 400 μm optical fiber was suspended 1mm under the surface of the tissue phantom on a movable one-dimensional translation stage (Fig. 24) The detector fiber was then adjusted to the desired depth and connected to a QE Pro charge-coupled device(CCD) spectrometer to allow photon counts to be collected at various depths in the tissue phantom. This data was then imported into MATLAB and processed using various methods for each experiment that will be specified in their respective sections.

5.2.2 Investigation of the effect of varying power density on optical fluence

Table 2 . Power density investigation experimental variables

Light source	Calibrated power (W)	Aperture diameter	Depth in phantom (cm)	Photon absorbing agent
1064nm columnated laser	0.5 to 4.5 increased	1.0, 2.0, 3.0, 4.0, and 4.2	Fixed at 1.7	Ink; horse blood

	in steps of 0.5	(no aperture)		

In order to investigate the effect of varying laser power density on 1064 nm laser fluence in various optical conditions, all other experimental variables were fixed. The optical properties of the tissue phantom were adjusted to values of 10 cm^{-1} for μ_s' and 0.10 cm^{-1} for μ_a measured by the ISS Oximeter at 750 nm for both ink and horse blood. The 1-dimensional translational stage was then used to fix the detector fiber at a depth of 1.7 cm below the surface of the tissue phantom. After these variables had been fixed, both the calibrated power and aperture size were varied independently in order to determine the relationship of power density to the measured fluence of the 1064 nm laser (Table 2.)

Apertures of 1, 2, 3, 4, and 4.2 cm diameter were used to vary the area of the 1064 nm laser beam and the calibrated power of the laser was varied from 0.5 to 4.5 W in 0.5 W steps for each separate aperture. Photon count data from each test was collected using the QE Pro CCD spectrometer and imported to MATLAB. The power density for each aperture diameter and calibrated power variation was determined by dividing calculated power by the empty aperture area. These calculated values were then compared to the collected fluence data to determine the relationship between the two datasets.

5.2.3 Investigation of the effect of varying aperture diameter on optical fluence

Table 3 *Aperture diameter investigation experimental variables*

Light source	Calibrated power (W)	Aperture diameter	Depth in phantom (cm)	Photon absorbing agent
1064 nm columnated laser	3.4	1.0, 1.5, 2.0, 2.5, 3.0, 3.5, 4.0, and 4.2 (no aperture)	1.6 to 4.0 with a step size of 0.1	Ink; horse blood

For this experiment the calibrated power of the laser was fixed at 3.4 W. The optical properties of both the ink and horse blood phantoms were again fixed at μ_s'=10 cm^{-1} and μ_a = 0.10 cm^{-1} at 750 nm, which was verified using the ISS Oximeter. By only varying the aperture diameter, photon count data can be collected by the QE Pro CCD spectrometer at varying depths as well to determine

if the effect of changing the beam diameter is altered in any significant way by the depth of the detector.

Apertures of diameter 1.0, 1.5, 2.0, 2.5, 3.0, 3.5, 4.0, and 4.2 cm were used to examine the relationship between aperture diameter and fluence. For each aperture, photon counts were recorded using the QE Pro CCD spectrometer every 0.1 cm from a depth of 1.6 to 4.0 cm (Table 3.) This entire process was performed using a tissue phantom with ink as the photon-absorbing agent and repeated in its entirety for a tissue phantom with horse blood as the photon-absorbing agent.

5.2.4 Investigation of light source wavelength on optical fluence

Table 4 *Wavelength investigation experimental variables*

Light source	Calibrated power (W)	Aperture diameter	Depth in phantom (cm)	Photon absorbing agent

1064 nm columnated laser, 810 nm laser, 850 nm LED	3.4	1.0, 2.0, no aperture	0.6 to 7.0 with a step size of 0.1	Horse blood

Wavelength has a significant effect on the absorption profile of light in numerous organic materials such as hemoglobin and water. The type of light sources, such as a focused laser or broad LED, can affect penetration depth in a significant manner as well. To determine the extent of these effects experimentally three separate light sources were selected: A 1064 nm columnated laser, an 810 nm laser, and an 850 nm LED.

Three aperture diameters were used for each light source 1.0, 2.0, and no aperture which varies depending on the diameter of the light source. Photon counts were then collected using the detector fiber and QE Pro CCD spectrometer for the entire depth of the container, which in this case was 7 cm. Due to the sensitivity of the spectrometer, data above a count of 200000 photons is considered full saturation by the QE Pro CCD spectrometer and was not accurately recorded. To correct this issue data collected from this

experiment was exported to MATLAB and normalized to accurately compare the rates of decay for each light source and aperture diameter.

5.2.5 Derivation of analytical solutions from Green's equation

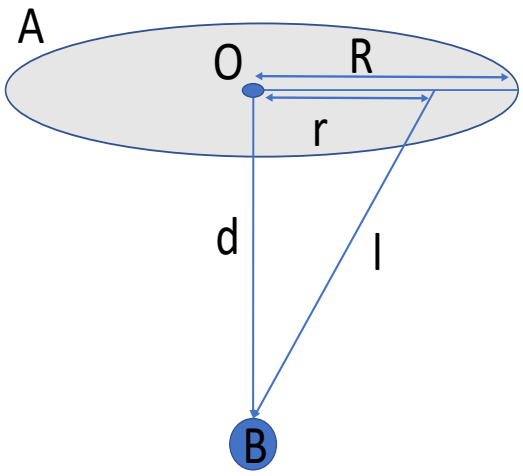

Figure 22 *Diagram of a disk light source and point detector. A represents the total fluence delivered by the disk source, while B represents the fluence measured by the point detector. d represents the distance from O, the central point of the disk source, and the detector.*

$$\Psi(d) = \frac{3\ \mu s\prime}{4\pi} * [\ e^{-(\mu eff * d)}/d] \qquad (1)$$

Theoretical solutions were also derived from Green's equation (Equation 1) to determine the validity of the results and to determine whether there is any significant deviation from the theoretically calculated result. Green's equation is

a general equation for calculating photon energy decay as light passes through media with fixed μ_a and $\mu_{s'}$ values. μ_{eff} is also easily calculated from this equation as it is a representation of the combined attenuation effect of both the scattering and absorbing properties of the media.

$$\mu_{eff} = \sqrt{3 * \mu s' * \mu a} \qquad (2)$$

However, this version of Green's equation (Equation 1) assumes both a point source and point detector. In figure 26, this would represent only the fluence from point O to point B. Although the detector fiber is small enough to be considered a point detector, the large diameter apertures used for the light sources cannot be safely assumed to be a point source. For these purposes, a modified equation is needed to account for flux received from other points along the disk source.

$$\Psi(r) = \frac{3\ \mu s'}{4\pi} * \left(\frac{e^{-(\mu eff * l)}}{\sqrt{r^2 + d^2}}\right) r\ dr\ d\theta \qquad (3)$$

Equation 3 allows for the optical fluence of point C (fig. 25) to be calculated analytically by adding l into the equation, where l is the distance from point C to detector B. l can be represented as $\sqrt{r^2 + d^2}$ as l is analogous to the hypotenuse of a right triangle formed between points O, B, and C. However, in order to calculate the total fluence from the disk source A to detector B every point inside the disk source must undergo this calculation. A simple way to do this is to represent the calculation as an integral from 0 to 2π:

$$\Psi(1,A) = \frac{3\ \mu s\prime}{4л} * \int_0^{2\pi} d\,\theta \int_{area} \left(\frac{e^{-\left(\mu eff*\sqrt{r^2+d^2}\right)}}{\sqrt{r^2+d^2}}\right) r\ dr \qquad (4)$$

This integral (Equation 4) represents the previous equation (Equation 3) for the entire radius of every possible angle inside the circular disk light source. Thankfully, after performing the integration this equation can be simplified to a single expression:

$$\Psi_B = \frac{3\ \mu s\prime}{2\mu eff} * \left[e^{-(\mu eff*d)} - e^{-\left(\mu eff*\frac{\sqrt{R^2+d^2}}{1}\right)}\right] \qquad (5)$$

Equation 5 can, therefore, be used as an accurate representation of fluence detected by a point detector with many alterable variables such as aperture size, R, and source-detector spacing d. This equation was used to calculate all presented analytical solutions used to compare to the collected experimental data.

5.2.6 Data analysis

The QE Pro spectrometer was used to collect all photon counts for each experiment over a spectrum from 700 to 1100 nm. Photon counts were then summed from wavelengths 30 nm below the desired wavelength to 30 nm above. As an example, photon counts collected for the 1064 nm laser source

would be summed from 1034 nm to 1094 nm to ensure all possible optical fluence generated by the light source is accurately represented.

5.3 Results

5.3.1 Differing aperture size vs depth results

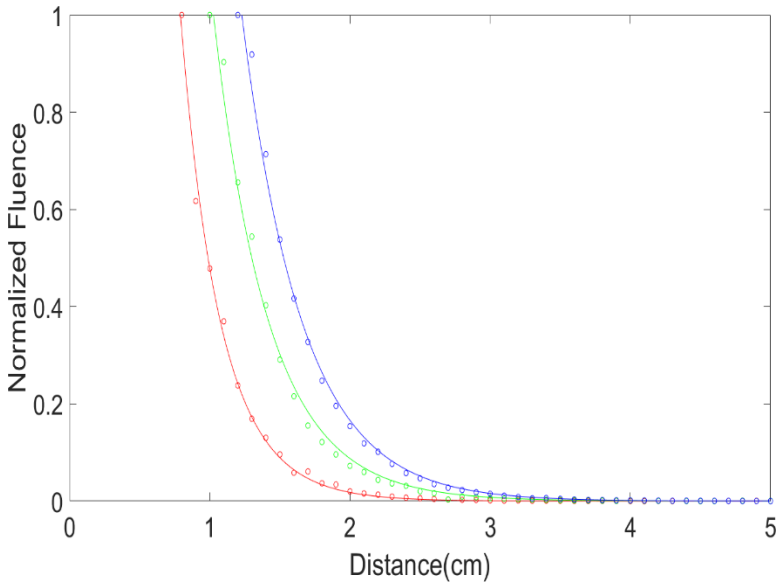

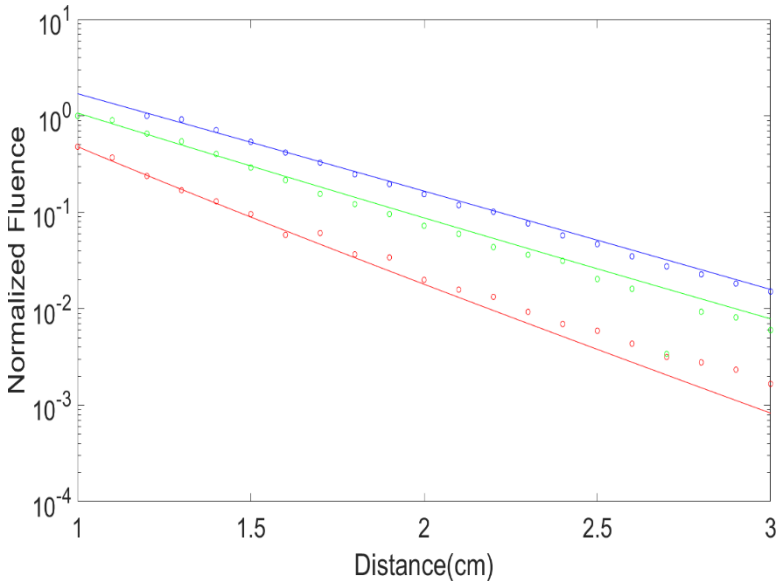

Figure 23 *Pictured are graphs depicting all experimentally acquired data for each aperture size plotted against their analytically derived curves (Eq. 5) with respect to normalized optical fluence for 1 cm diameter aperture (Red), 2 cm diameter aperture (Green), and no aperture(blue). The y-axis represents normalized fluence in both a linear(top) and logarithmic(bottom) scale, while the x-axis represents depth from the surface of the tissue phantom measured in centimeters.*

The above graphs (Fig. 26) depict the experimentally collected and analytically derived (eq. 5) fluence data with relation to penetration depth. Three different aperture diameters of 1,2, and 4.2 cm are shown with their respective fluence measurements after normalization. Due to the linear scale plot's exponential decay trend, the information can also be depicted in a logarithmic scale to better predict this trend. No matter the aperture size, the 1064nm laser does not appear to penetrate more than 4 cm into the tissue phantom media.

5.3.1 Power density-based investigation results

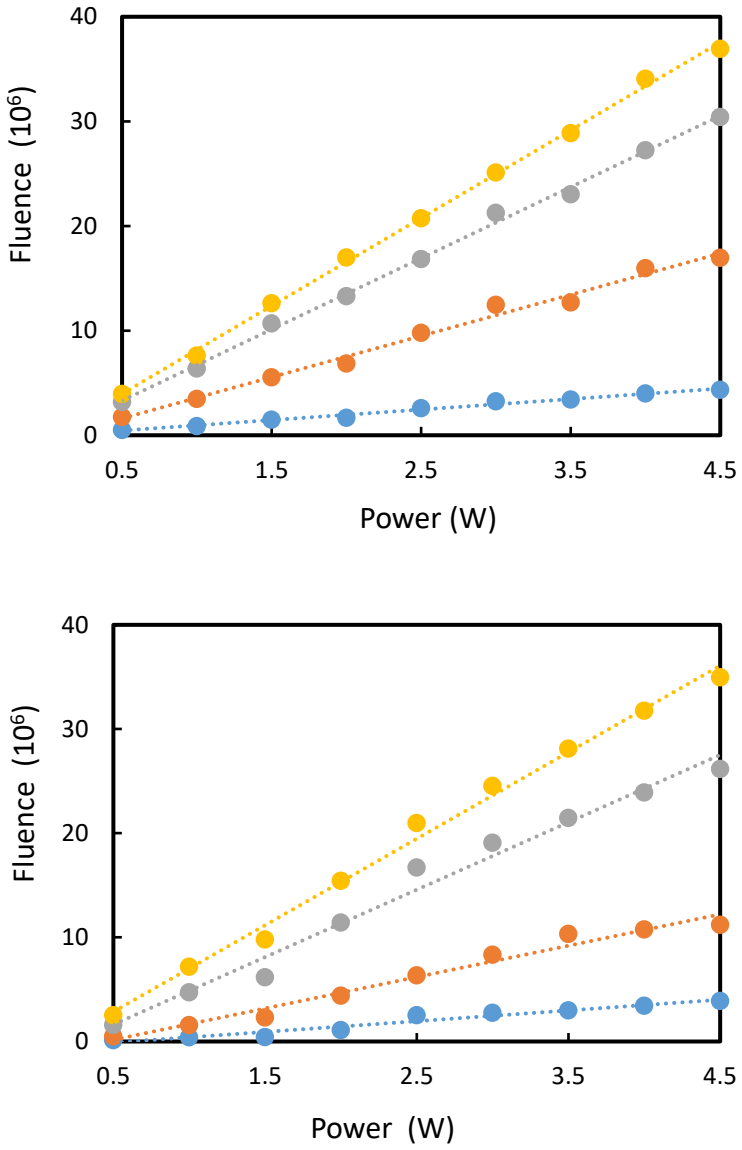

Figure 24 *Ink phantom based optical fluence to power relationship(top), as well as the same for a horse blood-based phantom(bottom). Shown are optical fluence measurements for 2 cm(yellow), 1.5 cm(gray), 1 cm(orange), and 0.5 cm(blue) diameter apertures.*

Pictured above (Fig 27) are the results of the power density related optical fluence measured by the QE Pro spectrometer for both the ink and horse blood tissue phantoms. When fluence is plotted with respect to power a linear trend can be observed regardless of aperture size or absorber type.

5.3.3 Aperture size variation result

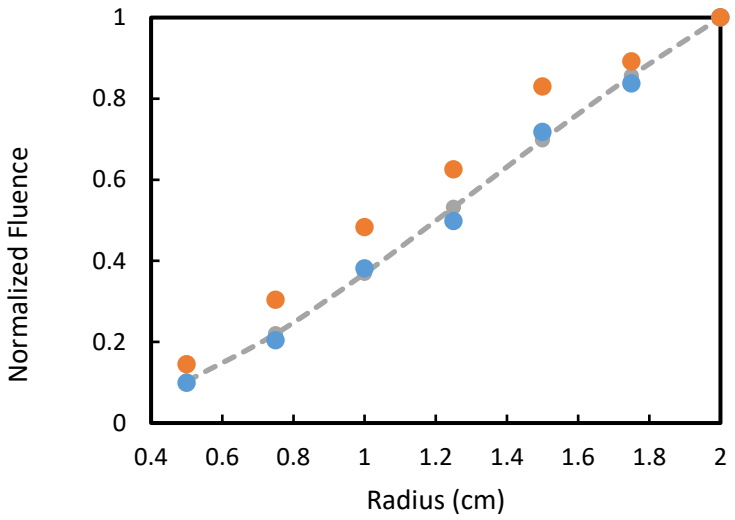

Figure 25 *Normalized optical fluence in both ink(blue) and horse blood(orange) plotted in relation to radius at a fixed depth d = 3.2 cm. The analytical result generated from equation 5 is also shown (gray) to compare the experimental results to the expected analytical trend.*

After normalization, optical fluence follows a fairly linear trend when examined with relation to aperture size. The analytical solution was also calculated using equation 5 mentioned previously to determine if the experimental results were reasonable. Both ink and blood follow this calculated trend, with ink showing the least amount of deviation from the curve.

5.4 Discussion

5.4.1 The linearity of power density to optical fluence

The observed linearity of the relationship between light source power density and optical fluence at increasing depths is quite important. These findings have numerous applications in both human and cell culture studies where exact dosage can multiply positive results [(Brondon, Stadler et al. 2005)]. It has even been suggested that lighter dosages of near-infrared laser light can have similar but distinctly different effects to high power stimulation [(Anders, Lanzafame et al. 2015)]. Also, much like a drug low-level light therapy has been suggested to have a biphasic dose-response curve which further reinforces the need to accurately measure light dosage properly to stay within the therapeutic range [(Huang, Chen et al. 2009, de Freitas and Hamblin 2016)].

Similar integration methods to those used in this paper to calculate disk source fluence have been used in the past to simulate photon propagation onto meshes using Monte Carlo simulations [(Arridge and Schweiger 1995, Fukui, Ajichi et al. 2003)]. Previous studies involving both animal and cellular studies have found similar results related to increasing light source power density, and have found similar trends in effectiveness of treatment like the optical fluence trends we have found in our experimental phantom study [(Peplow, Chung et al. 2010, Peplow, Chung et al. 2010)]

5.4.2 1064 nm laser fluence vs. other wavelengths

1064 nm light was observed to have a shallower penetration depth than the 810 nm laser in our experimental findings, which is consistent with previous findings [(Firbank, Hiraoka et al. 1993)]. This has the implication of suggesting 700-900 nm range light may be more optimal in reaching the deeper portions of the brain for photobiomodulation. Cellular and animal cadaver studies previously conducted support this assumption [(Pitzschke, Lovisa et al. 2015)]. However, 1064 light nm may have an enhanced therapeutic effect due to its high absorption coefficient with water as interaction with cytochrome C oxidase may not be the only mechanism altering cellular function [(Santana-Blank, Rodríguez-Santana et al. 2010)].

As for the penetration depth measurements undertaken for every aperture size and wavelength, the larger aperture size allows photons to travel further into the tissue phantom media regardless of wavelength and of the wavelengths, 810 nm penetrates deeper into the media than 1064 nm of 850 nm. These experimental depth related optical fluence measurements, when combined with measurements taken from previous measurements dealing with skull and brain matter optical properties measurements [(Okada and Delpy 2003)] could allow for far more advanced models of photon propagation in 3D space throughout the skull in the future.

5.5 Conclusions

Although more research and calculations are most certainly needed to expand upon the findings of this experiment, many valuable trends were discovered in the data. Effectively modulating a laser source power using aperture variations presents a measured and reproducible method to control laser fluence in organic media. The findings related to penetration depth and fluence of the 810 nm laser also opens the door to numerous other avenues of research related to other wavelengths along the absorption spectrum as well. With further experimental data collection as well as in vivo testing, an accurate model for optical fluence

regardless of wavelength or power may be possible to create in the future which would almost certainly revolutionize the field of dose-dependent light therapy.

Chapter 6 : Summary of the dissertation and future work

6.1 Summary

The main objectives of my dissertation work were to **(1)** determine the reproducibility of bb-NIRS tPBM pilot studies and ascertain if age plays an important role in tPBM effects **(2)** examine EEG electrical signals using Granger causality and source localization to determine if there were significant differences between tPBM cortical information flow when compared to sham **(3)** compare the metabolic effects of PBM at 3 separate wavelengths to determine differences in effect as well as providing more detailed information so that a mechanistic pathway for all 3 can be proposed.

The first objective was accomplished in chapter 2 by comparing the data collected previously with different operators, equipment, and environment to newly collected data using the same bb-NIRS system. It was determined in this study that there was no significant difference between datasets at any timepoint, which strongly validates both the bb-NIRS and 1064-nm tPBM methodology as producing reliably consistent results for use in further studies. When data from older (55+) participants was compared to the data collected from younger individuals tPBM was determined to have no significant

differences between populations. This indicated that the mechanisms responsible for tPBM's effects are not diminished by an individual's age.

The second objective was accomplished in chapter 3 by analyzing previously collected tPBM-EEG datasets using both source localization and Granger causality directionality calculations. Source localization had not been performed on tPBM-EEG datasets previously and tPBM was found to reliably induce changes in the cortex when compared to sham. This confirms the ability of tPBM to reach the outer cortex through the skull in a dosage high enough to induce the PBM effect which had been a source of debate earlier. The Granger causality directional analysis provided a consistent pattern across individuals from the site of stimulation in the right frontal region, to the right midbrain region, and finally the right occipital.

The third objective was accomplished in chapter 4 by conducting a series of repeated measurements using sham, 1064-nm, 852-nm, 808-nm laser PBM stimulation. When the chromophore concentration changes of [HbO], [Hb], [HbT], and [CCO] were compared to sham for all 3 wavelengths instead of one uniform trend becoming apparent 3 separate trends revealed themselves in the data. Using these chromophore trends combined with extensive repeated

ANOVA analysis revealed subtle significant differences in chromophore changes during stimulation and after stimulation.

6.2 Future Work

In order to validate these hypothesized pathways in the future, there must be an in vitro investigation utilizing various pathway blockers and assays to confirm channel activation. Blocking CCO directly is problematic as PBM has proven itself effective in detaching CCO inhibitors, such as Cyanide and carbon-monoxide, by donating the needed energy via photons in a manner the normal cellular machinery is unable to do [(Liang, Whelan et al. 2006)]. However, inhibiting NOS via a molecule such as L-NMMA (Cotter, Kaluski et al. 2000) would not be subject to any direct interference from the photobiomodulation and would determine NOS significance in the PBM pathway. Performing photobiomodulation on an astrocyte cell culture with the 808 and 852-nm wavelengths while also inhibiting NOS with L-NMMA would provide a definitive answer to its activation via PBM. Imaging the cell culture with an NO and general ROS assay such as OxiSelect™ would provide insights into the production of NO over time and answers on whether this effect is gradual like the proposed 808-nm PBM effect.

Similarly, in order to determine if TRPV1 plays a role in the PBM effect induced by various wavelengths, a TRPV1 channel blocker such as Capsazepine (CPV) can be used to prevent activation via light/heat activation[(Bevan, Hothi et al. 1992) (Walker, Urban et al. 2003)]. If the initial activation is based entirely on CCO activation without TRPV1 activation, the TRPV1 channel blocker should have little to no effect on inhibiting the pathway nor chromophore concentration results. To quantify this effect, a calcium assay would be performed at various time points to reveal if calcium levels are modulated by PBM with and without the inhibition. If TRPV1 does play a vital role in the 852-nm pathway, intracellular calcium levels will be significantly affected by CPV induced inhibition while 808-nm calcium levels will not be significantly altered. A schematic flow chart is shown in Fig. 26 to suggest in vitro experimental steps.

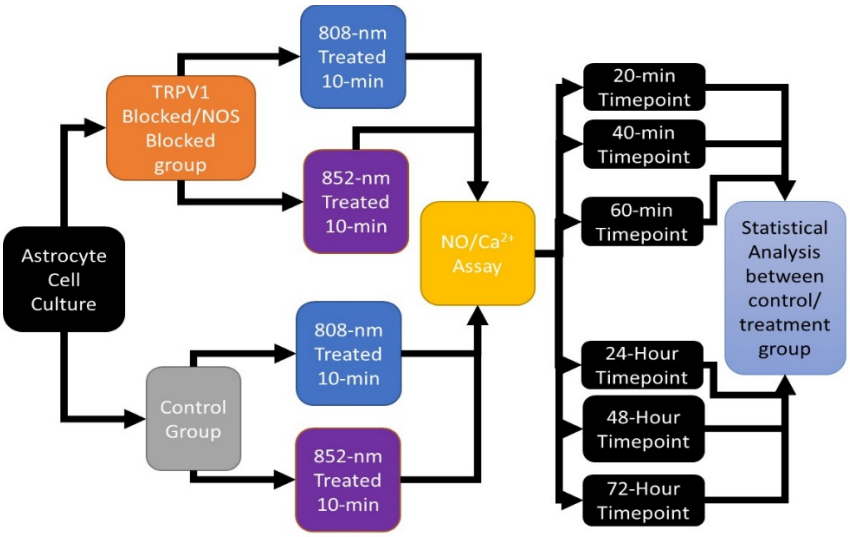

Figure 26 Flowchart of proposed TRPV1 and NOS inhibiting in vitro studies to determine hypothesized pathway correctness.

7. References

Aguirre, E., et al. (2010). "Kinetic model of the inhibition of respiration by endogenous nitric oxide in intact cells." Biochimica et Biophysica Acta (BBA)-Bioenergetics **1797**(5): 557-565.

Amaroli, A., et al. (2015). "Paramecium: a promising non-animal bioassay to study the effect of 808 nm infrared diode laser photobiomodulation." Photomedicine and laser surgery **33**(1): 35-40.

Amaroli, A., et al. (2019). "Photobiomodulation with 808-nm diode laser light promotes wound healing of human endothelial cells through increased reactive oxygen species production stimulating mitochondrial oxidative phosphorylation." Lasers in medical science **34**(3): 495-504.

Amaroli, A., et al. (2016). "808-nm laser therapy with a flat-top handpiece photobiomodulates mitochondria activities of Paramecium primaurelia (Protozoa)." Lasers in medical science **31**(4): 741-747.

Anders, J. J., et al. (2015). Low-level light/laser therapy versus photobiomodulation therapy, Mary Ann Liebert, Inc. 140 Huguenot Street, 3rd Floor New Rochelle, NY 10801 USA.

Anderson, C. and J. A. Horne (2003). "Prefrontal cortex: links between low frequency delta EEG in sleep and neuropsychological performance in healthy, older people." Psychophysiology **40**(3): 349-357.

Anderson, P. G., et al. (2015). "Broadband optical mammography: chromophore concentration and hemoglobin saturation contrast in breast cancer." PloS one **10**(3): e0117322.

Arany, P. (2016). "Craniofacial wound healing with photobiomodulation therapy: new insights and current challenges." Journal of dental research **95**(9): 977-984.

Argenta, P. A., et al. (2017). "The effect of photobiomodulation on chemotherapy-induced peripheral neuropathy: A randomized, sham-controlled clinical trial." Gynecologic Oncology **144**(1): 159-166.

Argibay, B., et al. (2019). "Light-emitting diode photobiomodulation after cerebral ischemia." Frontiers in neurology **10**: 911.

Arridge, S. R. and M. Schweiger (1995). "Photon-measurement density functions. Part 2: Finite-element-method calculations." Applied Optics **34**(34): 8026-8037.

Bainbridge, A., et al. (2014). "Brain mitochondrial oxidative metabolism during and after cerebral hypoxia–ischemia studied by simultaneous phosphorus magnetic-resonance and broadband near-infrared spectroscopy." Neuroimage **102**: 173-183.

Bale, G., et al. (2016). Interrelationship between broadband nirs measurements of cerebral cytochrome c oxidase and systemic changes indicates injury severity in neonatal encephalopathy. Oxygen Transport to Tissue XXXVIII, Springer**:** 181-186.

Barrett, D. W. and F. Gonzalez-Lima (2013). "Transcranial infrared laser stimulation produces beneficial cognitive and emotional effects in humans." Neuroscience **230**: 13-23.

Beltrame, T., et al. (2018). "Light-emitting diode therapy (photobiomodulation) effects on oxygen uptake and cardiac output dynamics during moderate exercise transitions: a randomized, crossover, double-blind, and placebo-controlled study." Lasers in medical science **33**(5): 1065-1071.

Berman, M. H., et al. (2017). "Photobiomodulation with near infrared light helmet in a pilot, placebo controlled clinical trial in dementia patients testing memory and cognition." Journal of neurology and neuroscience **8**(1).

Blanco, N. J., et al. (2017). "Improving executive function using transcranial infrared laser stimulation." J Neuropsychol **11**(1): 14-25.

Blinowska, K. J., et al. (2004). "Granger causality and information flow in multivariate processes." Physical Review E **70**(5): 050902.

Brondon, P., et al. (2005). "A study of the effects of phototherapy dose interval on photobiomodulation of cell cultures." Lasers in Surgery and Medicine: The Official Journal of the American Society for Laser Medicine and Surgery **36**(5): 409-413.

Brown, G. C. (2001). "Regulation of mitochondrial respiration by nitric oxide inhibition of cytochrome c oxidase." Biochimica et Biophysica Acta (BBA)-Bioenergetics **1504**(1): 46-57.

Byrnes, K. R., et al. (2004). "Photobiomodulation improves cutaneous wound healing in an animal model of type II diabetes." Photomedicine and Laser Therapy **22**(4): 281-290.

Cajochen, C., et al. (1999). "Frontal predominance of a relative increase in sleep delta and theta EEG activity after sleep loss in humans." Sleep Res Online **2**(3): 65-69.

Caldieraro, M. A. and P. Cassano (2019). "Transcranial and systemic photobiomodulation for major depressive disorder: A systematic review of efficacy, tolerability and biological mechanisms." Journal of affective disorders **243**: 262-273.

Campbell, I. G., et al. (2011). "Adolescent changes in homeostatic regulation of EEG activity in the delta and theta frequency bands during NREM sleep." Sleep **34**(1): 83-91.

Carus-Cadavieco, M., et al. (2017). "Gamma oscillations organize top-down signalling to hypothalamus and enable food seeking." Nature **542**(7640): 232-236.

Cassano, P., et al. (2016). "Review of transcranial photobiomodulation for major depressive disorder: targeting brain metabolism, inflammation, oxidative stress, and neurogenesis." Neurophotonics **3**(3): 031404.

Cassano, P., et al. (2018). "Transcranial photobiomodulation for the treatment of major depressive disorder. The ELATED-2 pilot trial." Photomedicine and laser surgery **36**(12): 634-646.

Chan, A. S., et al. (2019). "Photobiomodulation improves the frontal cognitive function of older adults." International journal of geriatric psychiatry **34**(2): 369-377.

Chang, S.-Y., et al. (2019). "Enhanced mitochondrial membrane potential and ATP synthesis by photobiomodulation increases viability of the auditory cell line after gentamicin-induced intrinsic apoptosis." Scientific reports **9**(1): 1-11.

Collman, J. P., et al. (2007). "A cytochrome C oxidase model catalyzes oxygen to water reduction under rate-limiting electron flux." Science **315**(5818): 1565-1568.

Cooley, J. W., et al. (1969). "The fast fourier transform and its applications." IEEE Transactions on Education **12**(1): 27-34.

da Silva, M. M., et al. (2018). "Randomized, blinded, controlled trial on effectiveness of photobiomodulation therapy and exercise training in the fibromyalgia treatment." Lasers in medical science **33**(2): 343-351.

Dai, Y., et al. (2012). "Source connectivity analysis from MEG and its application to epilepsy source localization." Brain topography **25**(2): 157-166.

de Andrade, A. L. M., et al. (2017). "Effect of photobiomodulation therapy (808 nm) in the control of neuropathic pain in mice." Lasers in medical science **32**(4): 865-872.

de Freitas, L. F. and M. R. Hamblin (2016). "Proposed mechanisms of photobiomodulation or low-level light therapy." IEEE Journal of selected topics in quantum electronics **22**(3): 348-364.

De Freitas, L. F. and M. R. Hamblin (2016). "Proposed Mechanisms of Photobiomodulation or Low-Level Light Therapy." IEEE Journal of Selected Topics in Quantum Electronics **22** 7000417.

de Oliveira, A. R., et al. (2017). "Pre-exercise infrared photobiomodulation therapy (810 nm) in skeletal muscle performance and postexercise recovery in humans: what is the optimal power output?" Photomedicine and laser surgery **35**(11): 595-603.

de Paula Gomes, C. A., et al. (2018). "Incorporation of photobiomodulation therapy into a therapeutic exercise program for knee osteoarthritis: A placebo-controlled, randomized, clinical trial." Lasers in Surgery and Medicine **50**(8): 819-828.

de Sousa, M. V. P., et al. (2018). "Pain management using photobiomodulation: mechanisms, location, and repeatability quantified by pain threshold and neural biomarkers in mice." Journal of biophotonics **11**(7): e201700370.

De Tommaso, M., et al. (2013). "Functional and effective connectivity in EEG alpha and beta bands during intermittent flash stimulation in migraine with and without aura." Cephalalgia **33**(11): 938-947.

Delorme, A. and S. Makeig (2004). "EEGLAB: an open source toolbox for analysis of single-trial EEG dynamics including independent component analysis." Journal of neuroscience methods **134**(1): 9-21.

Du, H., et al. (2010). "Early deficits in synaptic mitochondria in an Alzheimer's disease mouse model." Proceedings of the National Academy of Sciences **107**(43): 18670-18675.

Duchen, M. R. (2000). "Mitochondria and calcium: from cell signalling to cell death." The Journal of physiology **529**(1): 57-68.

Eells, J. T., et al. (2003). "Therapeutic photobiomodulation for methanol-induced retinal toxicity." Proceedings of the National Academy of Sciences **100**(6): 3439-3444.

Egner, T. and J. H. Gruzelier (2004). "EEG biofeedback of low beta band components: frequency-specific effects on variables of attention and event-related brain potentials." Clinical neurophysiology **115**(1): 131-139.

Ergenoglu, T., et al. (2004). "Alpha rhythm of the EEG modulates visual detection performance in humans." Cognitive Brain Research **20**(3): 376-383.

Farkas, E. and P. G. Luiten (2001). "Cerebral microvascular pathology in aging and Alzheimer's disease." Prog Neurobiol **64**(6): 575-611.

Firbank, M., et al. (1993). "Measurement of the optical properties of the skull in the wavelength range 650-950 nm." Physics in Medicine & Biology **38**(4): 503.

Foresti, P. (2006). "Testing for Granger causality between stock prices and economic growth."

Fukui, Y., et al. (2003). "Monte Carlo prediction of near-infrared light propagation in realistic adult and neonatal head models." Applied Optics **42**(16): 2881-2887.

García-Delaney, C., et al. (2017). "Evaluation of the effectiveness of the photobiomodulation in the treatment of dentin hypersensitivity after basic therapy. A randomized clinical trial." Journal of clinical and experimental dentistry **9**(5): e694.

Gonzalez-Lima, F., et al. (2014). "Mitochondrial respiration as a target for neuroprotection and cognitive enhancement." Biochem Pharmacol **88**(4): 584-593.

Gonzalez-Lima, F., et al. (1998). Brain cytochrome oxidase activity and how it relates to the pathophysiology of memory and Alzheimer's disease. Free Radicals, Oxidative Stress and Antioxidants: Pathological and Physiological Significance. T. Ozben. New York, Plenum Press. **296:** 205-227.

Gow Jr, D. W., et al. (2009). "Parallel versus serial processing dependencies in the perisylvian speech network: a Granger analysis of intracranial EEG data." Brain and language **110**(1): 43-48.

Gow Jr, D. W., et al. (2008). "Lexical influences on speech perception: a Granger causality analysis of MEG and EEG source estimates." Neuroimage **43**(3): 614-623.

Grech, R., et al. (2008). "Review on solving the inverse problem in EEG source analysis." Journal of neuroengineering and rehabilitation **5**(1): 25.

Hamblin, M. R. (2016). "Shining light on the head: Photobiomodulation for brain disorders." BBA Clin **6**: 113-124.

Hamblin, M. R. (2016). "Shining light on the head: photobiomodulation for brain disorders." BBA clinical **6**: 113-124.

Hamblin, M. R. (2017). "Mechanisms and applications of the anti-inflammatory effects of photobiomodulation." AIMS biophysics **4**(3): 337.

Hamblin, M. R. (2018). "Mechanisms and mitochondrial redox signaling in photobiomodulation." Photochemistry and photobiology **94**(2): 199-212.

Hamblin, M. R. (2018). "Photobiomodulation for traumatic brain injury and stroke." Journal of neuroscience research **96**(4): 731-743.

He, B., et al. (2011). "eConnectome: A MATLAB toolbox for mapping and imaging of brain functional connectivity." Journal of neuroscience methods **195**(2): 261-269.

Headley, D. B. and D. Paré (2013). "In sync: gamma oscillations and emotional memory." Frontiers in behavioral neuroscience **7**: 170.

Hedrich, T., et al. (2017). "Comparison of the spatial resolution of source imaging techniques in high-density EEG and MEG." Neuroimage **157**: 531-544.

Hesse, W., et al. (2003). "The use of time-variant EEG Granger causality for inspecting directed interdependencies of neural assemblies." Journal of neuroscience methods **124**(1): 27-44.

Hill, S. and H. Van Remmen (2014). "Mitochondrial stress signaling in longevity: a new role for mitochondrial function in aging." Redox Biol **2**: 936-944.

Hillebrand, A., et al. (2016). "Direction of information flow in large-scale resting-state networks is frequency-dependent." Proceedings of the National Academy of Sciences **113**(14): 3867-3872.

Holmes, E., et al. (2019). "Cognitive enhancement by transcranial photobiomodulation is associated with cerebrovascular oxygenation of the prefrontal cortex." Frontiers in neuroscience **13**: 1129.

Huang, Y.-Y., et al. (2009). "Biphasic dose response in low level light therapy." Dose-response **7**(4): dose-response. 09-027. Hamblin.

Huang, Y. Y., et al. (2012). "Transcranial low level laser (light) therapy for traumatic brain injury." J Biophotonics **5**(11-12): 827-837.

Jahan, A., et al. (2019). "Transcranial near-infrared photobiomodulation could modulate brain electrophysiological features and attentional performance in healthy young adults." Lasers in medical science **34**(6): 1193-1200.

Kadenbach, B., et al. (2009). "Degenerative diseases, oxidative stress and cytochrome c oxidase function." Trends Mol Med **15**(4): 139-147.

Kamiński, J., et al. (2012). "Beta band oscillations engagement in human alertness process." International Journal of psychophysiology **85**(1): 125-128.

Kanta, V., et al. (2019). "Closed-loop control of gamma oscillations in the amygdala demonstrates their role in spatial memory consolidation." Nature communications **10**(1): 1-14.

Karu, T. (2010). Mitochondrial mechanisms of photobiomodulation in context of new data about multiple roles of ATP, Mary Ann Liebert, Inc. 140 Huguenot Street, 3rd Floor New Rochelle, NY 10801 USA.

Karu, T. I. (2013). "Cellular and molecular mechanisms of photobiomodulation (low-power laser therapy)." IEEE Journal of selected topics in quantum electronics **20**(2): 143-148.

Kashyap, D. (2008). "Development of a broadband multi-channel NIRS system for quantifying absolute concentrations of hemoglobin derivatives and reduced scattering coefficients."

Kau, C. H., et al. (2013). "Photobiomodulation accelerates orthodontic alignment in the early phase of treatment." Progress in orthodontics **14**(1): 30.

Kawauchi, S., et al. (2008). "Simultaneous measurement of changes in light absorption due to the reduction of cytochrome c oxidase and light scattering in rat brains during loss of tissue viability." Appl Opt **47**(22): 4164-4176.

Khakh, B. S., et al. (2003). "ATP modulation of excitatory synapses onto interneurons." J Neurosci **23**(19): 7426-7437.

Klamer, S., et al. (2015). "Differences between MEG and high-density EEG source localizations using a distributed source model in comparison to fMRI." Brain topography **28**(1): 87-94.

Klimesch, W. (1997). "EEG-alpha rhythms and memory processes." International Journal of psychophysiology **26**(1-3): 319-340.

Klimesch, W., et al. (1998). "Induced alpha band power changes in the human EEG and attention." Neuroscience letters **244**(2): 73-76.

Klostermann, F., et al. (2007). "Task-related differential dynamics of EEG alpha-and beta-band synchronization in cortico-basal motor structures." European journal of Neuroscience **25**(5): 1604-1615.

Kong, W., et al. (2015). "Investigating driver fatigue versus alertness using the granger causality network." Sensors **15**(8): 19181-19198.

Laibow, R. E., et al. (2002). "EEG-neurobiofeedback treatment of patients with brain injury: Part 2: Changes in EEG parameters versus rehabilitation." Journal of Neurotherapy **5**(4): 45-71.

Lakatta, E. G. and D. Levy (2003). "Arterial and cardiac aging: major shareholders in cardiovascular disease enterprises: Part II: the aging heart in health: links to heart disease." Circulation **107**(2): 346-354.

Leutner, S., et al. (2001). "ROS generation, lipid peroxidation and antioxidant enzyme activities in the aging brain." J Neural Transm (Vienna) **108**(8-9): 955-967.

Liang, C.-C., et al. (2013). "Reexamining the relationships between stock prices and exchange rates in ASEAN-5 using panel Granger causality approach." Economic Modelling **32**: 560-563.

Lim, J., et al. (2008). "Attenuation of TCDD-induced oxidative stress by 670 nm photobiomodulation in developmental chicken kidney." Journal of biochemical and molecular toxicology **22**(4): 230-239.

Liu, T. C., et al. (2009). "Homeostatic photobiomodulation." Frontiers of Optoelectronics in China **2**(1): 1-8.

Manczak, M., et al. (2006). "Mitochondria are a direct site of Aβ accumulation in Alzheimer's disease neurons: implications for free radical generation and oxidative damage in disease progression." Human molecular genetics **15**(9): 1437-1449.

Marinazzo, D., et al. (2011). "Nonlinear connectivity by Granger causality." Neuroimage **58**(2): 330-338.

McColloch, A., et al. (2020). "Alterted Adipogenesis of Human Mesenchymal Stem Cells by Photobiomodulation Using 1064 nm Laser Light." Lasers in Surgery and Medicine.

Medrado, A. P., et al. (2008). "Influence of laser photobiomodulation upon connective tissue remodeling during wound healing." Journal of Photochemistry and Photobiology B: Biology **92**(3): 144-152.

Michels, L., et al. (2013). "Developmental changes of functional and directed resting-state connectivities associated with neuronal oscillations in EEG." Neuroimage **81**: 231-242.

Mitrofanis, J. and L. A. Henderson (2020). "How and why does photobiomodulation change brain activity?" Neural Regeneration Research **15**(12): 2243.

Musatov, A. and N. C. Robinson (2012). "Susceptibility of mitochondrial electron-transport complexes to oxidative damage. Focus on cytochrome c oxidase." Free Radic Res **46**(11): 1313-1326.

Naeser, M. A., et al. (2019). "Increased Functional Connectivity Within Intrinsic Neural Networks in Chronic Stroke Following Treatment With Red/Near-Infrared Transcranial

Photobiomodulation: Case Series With Improved Naming in Aphasia." Photobiomodul Photomed Laser Surg.

Naeser, M. A., et al. (2016). "Transcranial, Red/Near-Infrared Light-Emitting Diode Therapy to Improve Cognition in Chronic Traumatic Brain Injury." Photomed Laser Surg **34**(12): 610-626.

Nakamura, S., et al. (1999). "Analysis of music–brain interaction with simultaneous measurement of regional cerebral blood flow and electroencephalogram beta rhythm in human subjects." Neuroscience letters **275**(3): 222-226.

Neves, L. M., et al. (2018). "Photobiomodulation therapy improves acute inflammatory response in mice: the role of cannabinoid receptors/ATP-sensitive K+ channel/p38-MAPK signalling pathway." Molecular neurobiology **55**(7): 5580-5593.

Nicolaou, N., et al. (2012). "EEG-based automatic classification of 'awake'versus 'anesthetized'state in general anesthesia using Granger causality." PloS one **7**(3).

Nuwer, M. R., et al. (2005). "Routine and quantitative EEG in mild traumatic brain injury." Clinical neurophysiology **116**(9): 2001-2025.

Odinokov, D. and M. R. Hamblin (2018). "Aging of lymphoid organs: Can photobiomodulation reverse age-associated thymic involution via stimulation of extrapineal melatonin synthesis and bone marrow stem cells?" Journal of biophotonics **11**(8): e201700282.

Oishi, J., et al. (2017). "Hypotensive acute effect of photobiomodulation therapy on hypertensive rats." Life sciences **178**: 56-60.

Okada, E. and D. T. Delpy (2003). "Near-infrared light propagation in an adult head model. II. Effect of superficial tissue thickness on the sensitivity of the near-infrared spectroscopy signal." Applied Optics **42**(16): 2915-2921.

Oron, U., et al. (2007). "Ga-As (808 nm) laser irradiation enhances ATP production in human neuronal cells in culture." Photomedicine and laser surgery **25**(3): 180-182.

Pascual-Marqui, R. D. (1999). "Review of methods for solving the EEG inverse problem." International journal of bioelectromagnetism **1**(1): 75-86.

Passarella, S. and T. Karu (2014). "Absorption of monochromatic and narrow band radiation in the visible and near IR by both mitochondrial and non-mitochondrial photoacceptors results in photobiomodulation." Journal of Photochemistry and Photobiology B: Biology **140**: 344-358.

Peplow, P. V., et al. (2010). "Laser photobiomodulation of proliferation of cells in culture: a review of human and animal studies." Photomedicine and laser surgery **28**(S1): S-3-S-40.

Peplow, P. V., et al. (2010). "Laser photobiomodulation of wound healing: a review of experimental studies in mouse and rat animal models." Photomedicine and laser surgery **28**(3): 291-325.

Peplow, P. V., et al. (2011). "Laser photobiomodulation of gene expression and release of growth factors and cytokines from cells in culture: a review of human and animal studies." Photomedicine and laser surgery **29**(5): 285-304.

Petrov, Y., et al. (2014). "Ultra-dense EEG sampling results in two-fold increase of functional brain information." Neuroimage **90**: 140-145.

Pigatto, G. R., et al. (2019). "Photobiomodulation therapy reduces acute pain and inflammation in mice." Journal of Photochemistry and Photobiology B: Biology **196**: 111513.

Pinti, P., et al. (2021). "An analysis framework for the integration of broadband NIRS and EEG to assess neurovascular and neurometabolic coupling." Scientific reports **11**(1): 1-20.

Pitzschke, A., et al. (2015). "Red and NIR light dosimetry in the human deep brain." Physics in Medicine & Biology **60**(7): 2921.

Poyton, R. O. and K. A. Ball (2011). "Therapeutic photobiomodulation: nitric oxide and a novel function of mitochondrial cytochrome c oxidase." Discovery medicine **11**(57): 154-159.

Pruitt, T., et al. (2020). "Transcranial photobiomodulation (tPBM) with 1,064-nm laser to improve cerebral metabolism of the human brain in vivo." Lasers in Surgery and Medicine **52**(9): 807-813.

Pruitt, T., et al. (2020). "Transcranial photobiomodulation (tPBM) with 1,064-nm laser to improve cerebral metabolism of the human brain in vivo." Lasers in Surgery and Medicine.

Rashid, A. (2007). "Stock prices and trading volume: An assessment for linear and nonlinear Granger causality." Journal of Asian Economics **18**(4): 595-612.

Rhee, Y.-H., et al. (2019). "Effect of photobiomodulation therapy on neuronal injuries by ouabain: the regulation of Na, K-ATPase; Src; and mitogen-activated protein kinase signaling pathway." BMC neuroscience **20**(1): 1-11.

Rojas, J. C. and F. Gonzalez-Lima (2011). "Low-level light therapy of the eye and brain." Eye Brain **3**: 49-67.

Rupel, K., et al. (2018). "Photobiomodulation at multiple wavelengths differentially modulates oxidative stress in vitro and in vivo." Oxidative medicine and cellular longevity **2018**.

Salehpour, F., et al. (2019). "Near-infrared photobiomodulation combined with coenzyme Q10 for depression in a mouse model of restraint stress: reduction in oxidative stress, neuroinflammation, and apoptosis." Brain research bulletin **144**: 213-222.

Salehpour, F., et al. (2019). "Photobiomodulation and coenzyme Q10 treatments attenuate cognitive impairment associated with model of transient global brain ischemia in artificially aged mice." Frontiers in cellular neuroscience **13**: 74.

Salehpour, F., et al. (2018). "Brain photobiomodulation therapy: a narrative review." Molecular neurobiology **55**(8): 6601-6636.

Salehpour, F. and S. H. Rasta (2017). "The potential of transcranial photobiomodulation therapy for treatment of major depressive disorder." Reviews in the Neurosciences **28**(4): 441-453.

Sanderson, T. H., et al. (2018). "Inhibitory modulation of cytochrome c oxidase activity with specific near-infrared light wavelengths attenuates brain ischemia/reperfusion injury." Scientific reports **8**(1): 1-12.

Santana-Blank, L., et al. (2010). "Theoretic, experimental, clinical bases of the water oscillator hypothesis in near-infrared photobiomodulation." Photomedicine and laser surgery **28**(S1): S-41-S-52.

Santana-Blank, L., et al. (2015). "Water's many roles in laser photobiomodulation." J Cancer Res Treat **3**: 1-5.

Sauseng, P., et al. (2005). "EEG alpha synchronization and functional coupling during top-down processing in a working memory task." Human brain mapping **26**(2): 148-155.

Sauseng, P., et al. (2005). "A shift of visual spatial attention is selectively associated with human EEG alpha activity." European journal of Neuroscience **22**(11): 2917-2926.

Serrage, H., et al. (2019). "Under the spotlight: mechanisms of photobiomodulation concentrating on blue and green light." Photochemical & Photobiological Sciences **18**(8): 1877-1909.

Shuba, Y. M. (2020). "Beyond neuronal heat sensing: diversity of TRPV1 heat-capsaicin receptor-channel functions." Frontiers in cellular neuroscience **14**.

Silva, B., et al. (2017). "Endothelial nitric oxide synthase and cyclooxygenase are activated by hydrogen peroxide in renal hypertensive rat aorta." European journal of pharmacology **814**: 87-94.

Simon, H. U., et al. (2000). "Role of reactive oxygen species (ROS) in apoptosis induction." Apoptosis **5**(5): 415-418.

Smutzer, G. and R. K. Devassy (2016). "Integrating TRPV1 receptor function with capsaicin psychophysics." Advances in pharmacological sciences **2016**.

Sohrabpour, A., et al. (2016). "Noninvasive electromagnetic source imaging and granger causality analysis: an electrophysiological connectome (eConnectome) approach." IEEE Transactions on Biomedical Engineering **63**(12): 2474-2487.

Talakoub, O., et al. (2017). "Lateral hypothalamic activity indicates hunger and satiety states in humans." Annals of clinical and translational neurology **4**(12): 897-901.

Tang, A. C., et al. (2007). Top-down versus bottom-up processing in the human brain: distinct directional influences revealed by integrating SOBI and granger causality. International Conference on Independent Component Analysis and Signal Separation, Springer.

Tarasov, A. I., et al. (2012). "Regulation of ATP production by mitochondrial Ca2+." Cell calcium **52**(1): 28-35.

Tatmatsu-Rocha, J. C., et al. (2018). "Mitochondrial dynamics (fission and fusion) and collagen production in a rat model of diabetic wound healing treated by photobiomodulation: comparison of 904 nm laser and 850 nm light-emitting diode (LED)." Journal of Photochemistry and Photobiology B: Biology **187**: 41-47.

Taylor, C. T. and S. Moncada (2010). "Nitric oxide, cytochrome C oxidase, and the cellular response to hypoxia." Arteriosclerosis, thrombosis, and vascular biology **30**(4): 643-647.

Thatcher, R., et al. (2016). "Intelligence and eeg measures of information flow: efficiency and homeostatic neuroplasticity." Scientific reports **6**(1): 1-10.

Tominaga, M. and T. Tominaga (2005). "Structure and function of TRPV1." Pflügers Archiv **451**(1): 143-150.

Usumez, A., et al. (2014). "Effects of laser irradiation at different wavelengths (660, 810, 980, and 1,064 nm) on mucositis in an animal model of wound healing." Lasers in medical science **29**(6): 1807-1813.

Vargas, E., et al. (2017). "Beneficial neurocognitive effects of transcranial laser in older adults." Lasers Med Sci **32**(5): 1153-1162.

Von Euler, C. and U. Söderberg (1957). "The influence of hypothalamic thermoceptive structures on the electroencephalogram and gamma motor activity." Electroencephalography and clinical neurophysiology **9**(3): 391-408.

Wang, R., et al. (2019). "Photobiomodulation for global cerebral ischemia: targeting mitochondrial dynamics and functions." Molecular neurobiology **56**(3): 1852-1869.

Wang, X., et al. (2019). "Transcranial photobiomodulation with infrared laser increases power of brain oscillations." BioRxiv: 535757.

Wang, X., et al. (2019). "Transcranial photobiomodulation with 1064-nm laser modulates brain electroencephalogram rhythms." Neurophotonics **6**(2): 025013.

Wang, X., et al. (2018). Mechanistic Understanding of Transcranial Photobiomodulation Stimulated by Infrared Laser on the Human Forehead. Microscopy Histopathology and Analytics, Optical Society of America.

Wang, X., et al. (2017). "Impact of heat on metabolic and hemodynamic changes in transcranial infrared laser stimulation measured by broadband near-infrared spectroscopy." Neurophotonics **5**(1): 011004.

Wang, X., et al. (2016). Improved Oxygen Metabolism in Human Tissues in vivo by Low-Level Laser Therapy. Clinical and Translational Biophotonics, Optical Society of America.

Wang, X., et al. (2017). "Up-regulation of cerebral cytochrome-c-oxidase and hemodynamics by transcranial infrared laser stimulation: a broadband near-infrared spectroscopy study." Journal of Cerebral Blood Flow & Metabolism **37**(12): 3789-3802.

Wang, X., et al. (2017). "Up-regulation of cerebral cytochrome-c-oxidase and hemodynamics by transcranial infrared laser stimulation: A broadband near-infrared spectroscopy study." J Cereb Blood Flow Metab **37**(12): 3789-3802.

Wang, X., et al. (2016). "Interplay between up-regulation of cytochrome-c-oxidase and hemoglobin oxygenation induced by near-infrared laser." Scientific reports **6**: 30540.

Wang, X., et al. (2016). "Interplay between up-regulation of cytochrome-c-oxidase and hemoglobin oxygenation induced by near-infrared laser." Scientific reports **6**(1): 1-10.

Wang, X., et al. (2016). "Interplay between up-regulation of cytochrome-c-oxidase and hemoglobin oxygenation induced by near-infrared laser." Sci Rep **6**: 30540.

Wang, Y., et al. (2017). "Photobiomodulation of human adipose-derived stem cells using 810 nm and 980 nm lasers operates via different mechanisms of action." Biochimica et Biophysica Acta (BBA)-General Subjects **1861**(2): 441-449.

Wanniarachchi, H. I., et al. (2020). Topography of alpha rhythms evoked by transcranial laser neuromodulation and thermal stimulation. Clinical and Translational Biophotonics, Optical Society of America.

Welch, P. (1967). "The use of fast Fourier transform for the estimation of power spectra: a method based on time averaging over short, modified periodograms." IEEE Transactions on audio and electroacoustics **15**(2): 70-73.

Welch, P. D. (1987). On the relationship between batch means, overlapping means and spectral estimation. Proceedings of the 19th conference on Winter simulation.

White, N. E. (1999). T{White, 1999 #101}heories of the effectiveness of alpha-theta training for multiple disorders. Introduction to quantitative EEG and neurofeedback, Elsevier**:** 341-367.

Wong-Riley, M. T., et al. (2005). "Photobiomodulation directly benefits primary neurons functionally inactivated by toxins role of cytochrome c oxidase." Journal of Biological Chemistry **280**(6): 4761-4771.

Wong-Riley, M. T., et al. (2005). "Photobiomodulation directly benefits primary neurons functionally inactivated by toxins: role of cytochrome c oxidase." Journal of Biological Chemistry **280**(6): 4761-4771.

Yang, L., et al. (2018). "Photobiomodulation therapy promotes neurogenesis by improving post-stroke local microenvironment and stimulating neuroprogenitor cells." Experimental neurology **299**: 86-96.

Yu, B., et al. (2010). "Endothelial dysfunction enhances vasoconstriction due to scavenging of nitric oxide by a hemoglobin-based oxygen carrier." The Journal of the American Society of Anesthesiologists **112**(3): 586-594.

Zhang, H., et al. (2018). "Electrophysiological mechanisms of human memory consolidation." Nature communications **9**(1): 1-11.

Zomorrodi, R., et al. (2019). "Modulation of neural oscillation power spectral density with transcranial photobiomodulation." Brain Stimul **12**: 457-458.

Zomorrodi, R., et al. (2019). "Pulsed Near Infrared Transcranial and Intranasal Photobiomodulation Significantly Modulates Neural Oscillations: a pilot exploratory study." Sci Rep **9**(1): 6309.

Zomorrodi, R., et al. (2019). "Pulsed near infrared transcranial and intranasal photobiomodulation significantly modulates neural oscillations: a pilot exploratory study." Scientific reports **9**(1): 1-11.

Zomorrodi, R., et al. (2017). Complementary EEG evidence for a significantly improved Alzheimer's disease case after photobiomodulation treatment. 26th Annual Scientific Conference, Canadian Academy of Geriatric Psychiatry Toronto.

Biographical Information

Tyrell Pruitt was born and brought up in central Texas. He earned her bachelor's degree from Tarleton State University in Pre-Med Biology, Stephenville, TX, USA. She joined the graduate program in the Department of Bioengineering, the University of Texas at Arlington in 2015. His research focused on a collaborative project with professors from the University of Texas Southwestern Medical Center on an NIH-funded project to investigate transcranial photobiomodulation in humans. He has given 3 research presentations BMES and OSA Biomedical Optics

topical meetings. His areas of research interests include experimental design, bb-NIRS and EEG data collection, statistical analysis, and optical instrumentation.

Appendix

Appendix 1: Spectrum Analysis

Figure 27 (a) below shows a detailed spectrum of chromophores relevant to the hypothesized pathways based on various previously collected datasets from a research article [(Kolyva, Tachtsidis et al. 2012)] that is congruent with other studies [(Bakker, Smith et al. 2012) (Van Gastel, Stuijk et al. 2018) (Sordillo, Pratavieira et al. 2014)]. There is a peak in CCO absorption between 800 and 900 nm, but water absorption steadily increases between 800 and 980-nm. This relationship is better represented in figure 27 (b) that displays the relative absorbance of CCO when compared to water. At 810 nm there is an acute peak where CCO absorbs twice as much as at 852 nm relative to water absorption. Water absorption is particularly important in creating or transmitting heat from light through tissue, so 852 nm would likely waste twice as much expended energy heating water in tissue than 810 nm laser light. In other words, water would absorb twice as much of the energy from 852-nm light than 810-nm light. This trend is broken at 1064-nm where there is another dip

in water absorbance as seen in Figure 27 (c) (Sordillo, Pu et al. 2014). Values displayed are present in supplementary table 5.

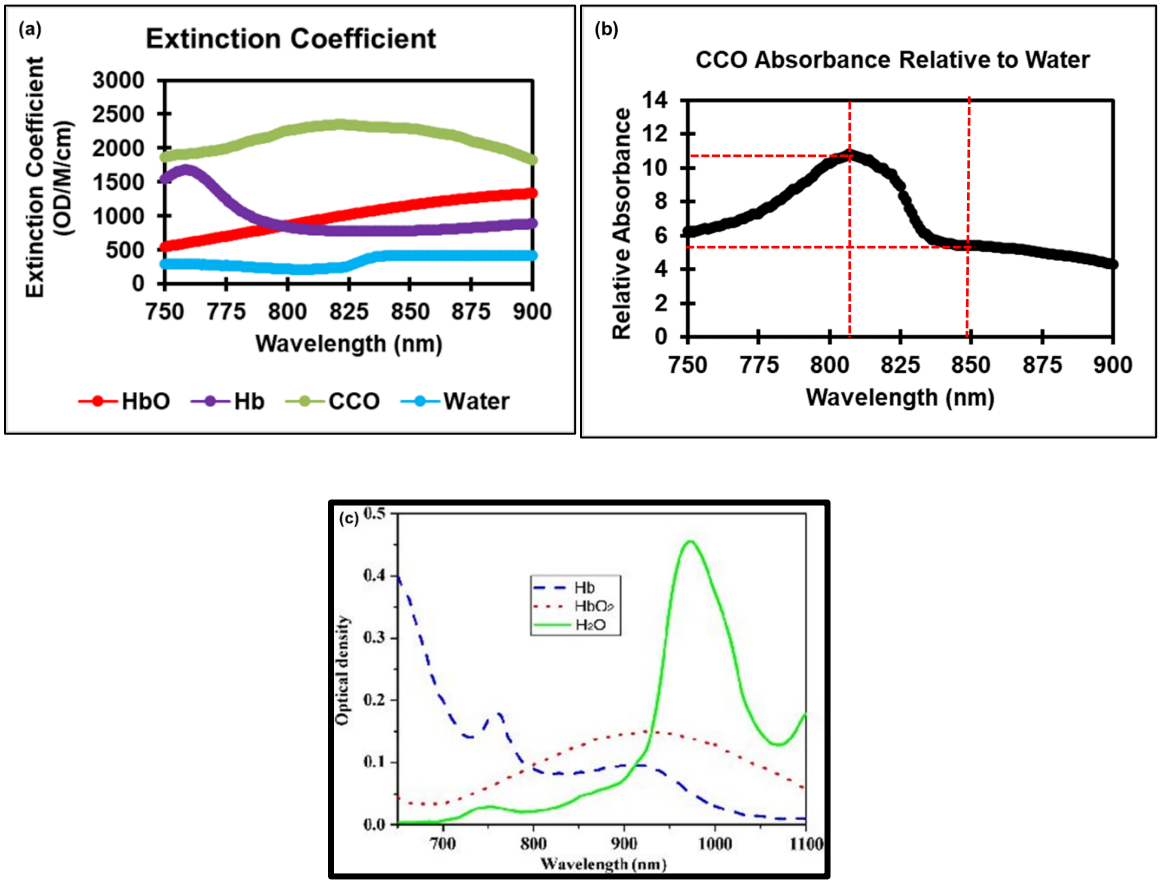

Figure 27 (a) Known extinction coefficient spectra for Hb (purple), CCO (green), HbO (red), and water (blue) from 750 to 900 nm. Note that the unit of water absorbance is %. (b) It displays a ratio between CCO absorbance and water absorbance from 750 to 900 nm; the unit for y axis is OD/M/10^4 or (OD/M)10^{-4}. (c) displays optical density spectra acquired from 650-nm to 1100-nm for Hb (blue), HbO (red), and water (green).

Table 5 Table of extinction coefficients from 650 to 900 nm for HbO, Hb, oxi-CCO, water, and the ratio between oxi-CCO and water extinction coefficients that are plotted above

Lambda (λ)	HbO OD/M/cm	Hb OD/M/cm	Oxi-CCO OD/M/cm	Water 10^4/cm	Ratio of CCO to water (OD/M 10^{-4})
650	386.8	3734.15	4929.24	32.0117	153.98
651	379.2	3702.97	4892.33	32.242	151.74
652	372.1	3671.79	4855.41	33.3935	145.40
653	365.81	3640.47	4806.77	33.1632	144.94
654	360.01	3611.68	4758.13	33.8541	140.55
655	354.41	3583.19	4702.97	32.4723	144.83
656	349.41	3554.61	4648.25	33.1632	140.16
657	345.01	3525.99	4587.89	32.7026	140.29
658	340.91	3497.33	4527.95	36.6177	123.65
659	337.52	3468.62	4463.68	35.2359	126.68
660	334.52	3439.92	4399.84	38.2298	115.09
661	331.71	3405.35	4332	38.2298	113.31
662	329.32	3370.86	4263.9	37.5389	113.59
663	327.52	3336.25	4191.72	37.7692	110.98
664	325.92	3298.16	4119.54	36.6177	112.50
665	324.42	3257.38	4044.58	37.7692	107.09
666	323.32	3216.6	3969.5	37.7692	105.10
667	322.62	3175.39	3897.32	37.7692	103.19
668	321.92	3131.91	3825.14	37.0783	103.16
669	321.52	3088.31	3751.96	38.4601	97.55
670	321.22	3044.71	3678.78	38.2298	96.23
671	321.12	2998.54	3606.38	37.3086	96.66
672	321.12	2951.16	3533.98	38.6904	91.34
673	321.32	2903.78	3462.63	39.3813	87.93
674	321.32	2856.18	3391.23	40.9934	82.73
675	321.02	2807.97	3321.57	38.2298	86.88
676	320.72	2759.9	3251.87	38.2298	85.06
677	320.52	2711.69	3183.29	39.3813	80.83
678	320.42	2664.53	3114.8	39.6116	78.63
679	320.02	2617.62	3055.44	39.6116	77.13
680	319.32	2570.63	2996.02	40.7631	73.50
681	318.52	2524.16	2948.86	42.1449	69.97
682	318.02	2478.17	2901.65	43.757	66.31
683	317.22	2432.27	2861.57	42.1449	67.90
684	316.22	2386.4	2821.57	41.6843	67.69

685	315.62	2343.02	2785.17	43.2964	64.33
686	315.02	2299.81	2748.69	44.4479	61.84
687	313.92	2256.64	2717.29	46.06	58.99
688	313.42	2215.64	2685.94	46.9812	57.17
689	312.52	2176.64	2659.01	48.8236	54.46
690	312.22	2137.64	2632.13	47.2115	55.75
691	312.12	2099.16	2608.63	50.666	51.49
692	312.12	2065.07	2585.05	51.8175	49.89
693	312.22	2030.98	2565.55	51.5872	49.73
694	312.42	1996.89	2546.14	52.5084	48.49
695	312.92	1966.01	2523.34	54.8114	46.04
696	313.92	1936.52	2500.67	58.0356	43.09
697	314.72	1907.12	2479.95	59.1871	41.90
698	316.32	1878.63	2459.28	59.878	41.07
699	318.02	1852.53	2437	64.0234	38.06
700	319.82	1826.56	2414.81	65.6355	36.79
701	321.82	1800.54	2391.57	64.484	37.09
702	324.22	1777.26	2368.38	65.1749	36.34
703	326.82	1754.33	2343.19	68.1688	34.37
704	329.52	1731.45	2317.92	69.3203	33.44
705	332.21	1709.47	2294.9	70.2415	32.67
706	335.11	1688.28	2271.92	72.5445	31.32
707	338.52	1667.08	2244.04	77.8414	28.83
708	341.71	1645.98	2216.12	79.2232	27.97
709	344.91	1626.3	2188.32	79.9141	27.38
710	348.41	1606.59	2160.66	84.0595	25.70
711	352.31	1586.91	2135.64	89.3564	23.90
712	356.31	1567.28	2110.67	90.9685	23.20
713	360.11	1547.7	2081.57	95.5745	21.78
714	363.81	1528.11	2052.48	100.1805	20.49
715	367.91	1508.91	2024.98	105.2471	19.24
716	372.3	1490.32	1997.49	109.3925	18.26
717	376.4	1471.74	1973.09	113.7682	17.34
718	380.6	1453.15	1948.72	120.2166	16.21
719	385.3	1436.12	1926.92	127.1256	15.16
720	389.8	1419.32	1905.03	129.1983	14.75
721	394.2	1402.55	1887.4	136.3376	13.84
722	398.7	1387.14	1869.81	143.2466	13.05
723	403.4	1372.94	1857.35	149.9253	12.39
724	408.2	1358.86	1844.84	153.3798	12.03
725	413.2	1345.27	1835.24	162.8221	11.27

726	418	1334.85	1825.64	170.1917	10.73
727	422.89	1324.55	1817.52	180.0946	10.09
728	427.99	1314.26	1809.44	188.846	9.58
729	433.09	1307.75	1805.36	198.2883	9.10
730	438.16	1302.58	1801.24	209.8033	8.59
731	443.37	1297.28	1800.54	223.1607	8.07
732	448.67	1294.28	1799.93	236.0575	7.62
733	453.88	1294.68	1799.46	250.3361	7.19
734	459.18	1294.98	1798.93	261.8511	6.87
735	464.48	1295.59	1800.54	272.2146	6.61
736	469.86	1302.45	1802.15	280.966	6.41
737	475.25	1309.27	1804.06	287.875	6.27
738	480.94	1316.09	1805.93	293.4022	6.16
739	486.37	1327.38	1810.23	297.087	6.09
740	491.84	1340.75	1814.53	302.6142	6.00
741	497.44	1354.17	1820.82	301.693	6.04
742	503.04	1369.33	1827.03	302.8445	6.03
743	508.73	1388.35	1833.24	303.996	6.03
744	514.55	1407.46	1839.41	305.1475	6.03
745	520.15	1426.44	1844.62	302.1536	6.10
746	525.76	1449.72	1849.75	301.9233	6.13
747	531.58	1473.21	1853.83	301.2324	6.15
748	537.48	1496.71	1858.04	300.3112	6.19
749	543.48	1520.81	1863.04	302.1536	6.17
750	549.34	1545.39	1868.03	298.4688	6.26
751	555.25	1569.89	1876.33	300.7718	6.24
752	561.15	1593.38	1884.62	300.7718	6.27
753	567.06	1613.79	1891.22	301.0021	6.28
754	572.96	1634.16	1897.82	300.3112	6.32
755	578.96	1654.49	1901.43	298.6991	6.37
756	585.47	1664.17	1905.03	296.6264	6.42
757	591.03	1672.86	1908.12	298.4688	6.39
758	597.24	1681.59	1911.2	296.8567	6.44
759	602.93	1681.15	1914.33	294.3234	6.50
760	609.45	1674.07	1917.32	293.6325	6.53
761	615.53	1667	1920.1	294.0931	6.53
762	621.74	1656.18	1923.01	290.4083	6.62
763	628.12	1633.9	1928.01	288.3356	6.69
764	634.33	1611.71	1933	288.1053	6.71
765	640.54	1589.39	1938.6	286.7235	6.76
766	646.75	1557.81	1944.12	287.6447	6.76

767	653.35	1525.5	1949.29	285.3417	6.83
768	659.43	1493.1	1954.41	282.5781	6.92
769	665.64	1458.62	1959.71	280.2751	6.99
770	671.81	1422.53	1965.1	280.5054	7.01
771	678.32	1386.53	1970	278.2024	7.08
772	684.71	1350.96	1974.91	276.5903	7.14
773	690.92	1316.56	1980.51	272.9055	7.26
774	697.22	1282.17	1986.2	272.4449	7.29
775	703.6	1247.77	1994.71	274.2873	7.27
776	709.94	1217.2	2003.18	269.451	7.43
777	716.41	1186.71	2015	265.7662	7.58
778	722.71	1156.31	2026.77	264.6147	7.66
779	729.53	1129.51	2038.19	264.845	7.70
780	735.83	1104.71	2049.48	263.0026	7.79
781	741.99	1080.05	2060.68	259.5481	7.94
782	748.29	1056.81	2071.89	257.4754	8.05
783	754.72	1036.92	2084.57	257.2451	8.10
784	761.1	1017.03	2097.38	253.0997	8.29
785	767.92	997.23	2107.54	250.3361	8.42
786	774.09	981.94	2117.75	246.8816	8.58
787	780.6	966.57	2126.57	242.9665	8.75
788	787.2	951.28	2135.47	244.3483	8.74
789	793.89	938.25	2142.77	242.5059	8.84
790	800.32	926.18	2150.06	238.5908	9.01
791	806.79	914.06	2156.66	235.8272	9.15
792	813.17	903.16	2163.26	235.3666	9.19
793	819.47	893.69	2175.73	233.0636	9.34
794	826.2	884.18	2188.15	231.4515	9.45
795	832.8	874.97	2200.96	226.3849	9.72
796	838.97	867.37	2213.64	224.3122	9.87
797	845.57	859.77	2227.32	223.1607	9.98
798	852.17	852.17	2241.05	222.0092	10.09
799	858.6	845.88	2251.21	219.0153	10.28
800	865.07	839.66	2261.33	220.1668	10.27
801	871.37	833.58	2266.02	219.0153	10.35
802	877.8	828.29	2270.71	215.5608	10.53
803	884.27	823.51	2275.62	216.2517	10.52
804	890.69	818.78	2280.61	215.3305	10.59
805	897.08	814.39	2286.43	214.6396	10.65
806	903.55	810.91	2292.12	213.7184	10.72
807	909.98	807.31	2298.5	212.5669	10.81

808	916.19	803.79	2304.93	213.9487	10.77
809	922.48	801.19	2310.79	216.0214	10.70
810	928.87	798.49	2316.61	216.9426	10.68
811	935.17	795.89	2320.61	219.2456	10.58
812	941.38	793.89	2324.69	220.6274	10.54
813	947.54	791.98	2327.51	223.1607	10.43
814	953.67	790.2	2330.29	222.0092	10.50
815	960.05	788.59	2332.9	226.6152	10.29
816	966.35	787.2	2335.51	229.1485	10.19
817	972.56	785.9	2338.2	232.8333	10.04
818	978.64	784.68	2340.89	235.1363	9.96
819	984.55	783.99	2343.58	234.6757	9.99
820	990.84	783.21	2346.32	241.1241	9.73
821	997.05	782.51	2347.19	243.1968	9.65
822	1002.96	781.99	2348.01	244.118	9.62
823	1008.82	781.51	2346.49	251.7179	9.32
824	1015.03	780.99	2344.89	258.6269	9.07
825	1020.85	780.69	2342.32	263.4632	8.89
826	1027.02	780.6	2339.72	280.5054	8.34
827	1033.06	780.38	2336.29	290.178	8.05
828	1039.05	780.3	2332.9	306.9899	7.60
829	1044.65	780.21	2329.43	318.7352	7.31
830	1050.43	780.21	2325.91	336.0077	6.92
831	1056.12	780.21	2322.69	347.753	6.68
832	1061.85	780.21	2319.39	365.2558	6.35
833	1067.71	780.21	2316.83	377.2314	6.14
834	1073.62	780.3	2314.23	381.3768	6.07
835	1079.44	780.3	2312.53	391.2797	5.91
836	1084.82	780.38	2310.71	400.722	5.77
837	1090.43	780.51	2310.01	400.722	5.76
838	1095.94	780.69	2309.23	404.8674	5.70
839	1101.5	780.99	2308.41	408.3219	5.65
840	1106.93	781.3	2307.49	413.3885	5.58
841	1112.53	781.51	2305.63	417.5339	5.52
842	1117.92	781.82	2303.72	415.6915	5.54
843	1123	782.12	2301.33	417.7642	5.51
844	1128.3	782.51	2298.89	419.6066	5.48
845	1133.6	783.12	2296.64	422.6005	5.43
846	1138.81	783.68	2294.2	422.6005	5.43
847	1143.89	784.29	2292.81	422.6005	5.43
848	1149.1	784.81	2291.34	422.6005	5.42

849	1154.4	785.42	2290.6	422.6005	5.42
850	1159.31	785.9	2289.9	422.6005	5.42
851	1164.21	786.9	2287.3	422.6005	5.41
852	1169.12	787.81	2284.74	422.6005	5.41
853	1173.9	788.81	2279.92	422.6005	5.39
854	1178.72	789.89	2275.14	422.6005	5.38
855	1183.89	790.98	2267.93	422.6005	5.37
856	1188.19	792.11	2260.72	422.6005	5.35
857	1193.09	793.28	2252.12	422.6005	5.33
858	1197.7	794.72	2243.61	422.6005	5.31
859	1202.3	796.11	2236.75	422.6005	5.29
860	1206.77	797.49	2229.75	422.6005	5.28
861	1211.07	799.1	2225.32	422.6005	5.27
862	1215.29	800.71	2220.85	422.6005	5.26
863	1219.67	802.32	2216.42	422.6005	5.24
864	1224.19	804.18	2212.12	422.6005	5.23
865	1228.27	806.09	2206.35	422.6005	5.22
866	1232.18	808	2200.44	422.6005	5.21
867	1236.39	810	2193.53	422.6005	5.19
868	1240.39	812	2186.63	422.6005	5.17
869	1244.6	814.09	2176.73	422.6005	5.15
870	1248.68	816.39	2166.87	422.6005	5.13
871	1252.59	818.69	2152.36	422.6005	5.09
872	1256.2	821.08	2137.86	422.6005	5.06
873	1259.8	823.51	2125.05	422.6005	5.03
874	1263.8	825.9	2112.28	422.6005	5.00
875	1267.49	828.29	2102.38	422.6005	4.97
876	1270.66	830.81	2092.47	422.6005	4.95
877	1274.26	833.37	2084.05	422.6005	4.93
878	1277.78	835.89	2075.75	422.6005	4.91
879	1281.08	838.49	2067.89	422.6005	4.89
880	1284.25	840.97	2060.08	422.6005	4.87
881	1287.47	843.57	2052.48	422.6005	4.86
882	1290.38	846.09	2044.88	422.6005	4.84
883	1293.46	848.7	2035.36	422.6005	4.82
884	1296.76	851.39	2025.98	422.6005	4.79
885	1299.67	854	2015.91	422.6005	4.77
886	1302.36	856.6	2005.79	422.6005	4.75
887	1305.49	859.16	1995.41	422.6005	4.72
888	1308.05	861.77	1984.99	422.6005	4.70
889	1310.48	864.29	1972	422.6005	4.67

890	1313.35	866.76	1958.89	422.6005	4.64
891	1316.17	869.2	1946.2	422.6005	4.61
892	1318.56	871.59	1933.52	422.6005	4.58
893	1320.65	873.97	1919.8	422.6005	4.54
894	1323.16	876.28	1906.12	422.6005	4.51
895	1325.86	878.49	1891.14	422.6005	4.48
896	1327.94	880.49	1876.11	422.6005	4.44
897	1330.07	882.49	1861.43	422.6005	4.40
898	1331.98	884.35	1846.75	422.6005	4.37
899	1333.76	886.09	1833.85	422.6005	4.34
900	1336.15	887.78	1820.82	422.6005	4.31

Appendix 2: bb-NIRS stability experiment

An experimental study to determine the stability and accuracy of the bb-NIRS equipment was conducted using a raw chicken breast to mimic tissue, but this chicken breast should hypothetically not show any change in chromophore data from baseline as the cells are no longer alive. Figure 28 (a) below demonstrates the experimental setup used for this experiment where all experimental parameters such as laser power density were kept identical to those in chapters 2 and 4. Figure 28 (b) below demonstrates the protocol of a 2-minute reference baseline, 8 minutes of stimulation, and 5 minutes of post stimulation readings once again identical to chapters 2 and 4 to provide an accurate comparison.

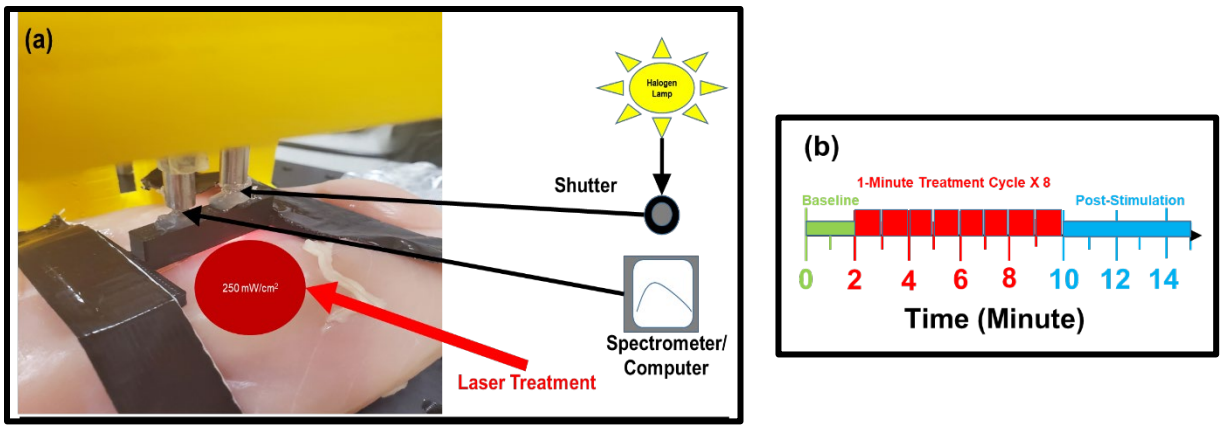

Figure 28 Presents (a) an image of the experimental setup with additional schematic drawings for clarity as well as (b) a block diagram of the experimental protocol

Figure 29 below displays chromophore changes of a raw uncooked chicken breast measured by a bb-NIRS system. Fig. 29(a) HbO, (b) CCO, (c) Hb, and (d) HbT all show very little deviation from zero during the entire experiment for every wavelength tested: 1064-nm, 852-m, 808-nm, and sham. Regardless of what wavelength laser was used to stimulate the chicken breast, there was no significant difference between any of the groups when a repeated measures ANOVA was performed. All groups were also not significantly different from zero when a paired t-test was performed. This set of results are expected for a well functional bb-NIRS, also indicating that the bb-NIRS system is very stable with little drift. This adds further validity to data reported in this study and others using bb-NIRS.

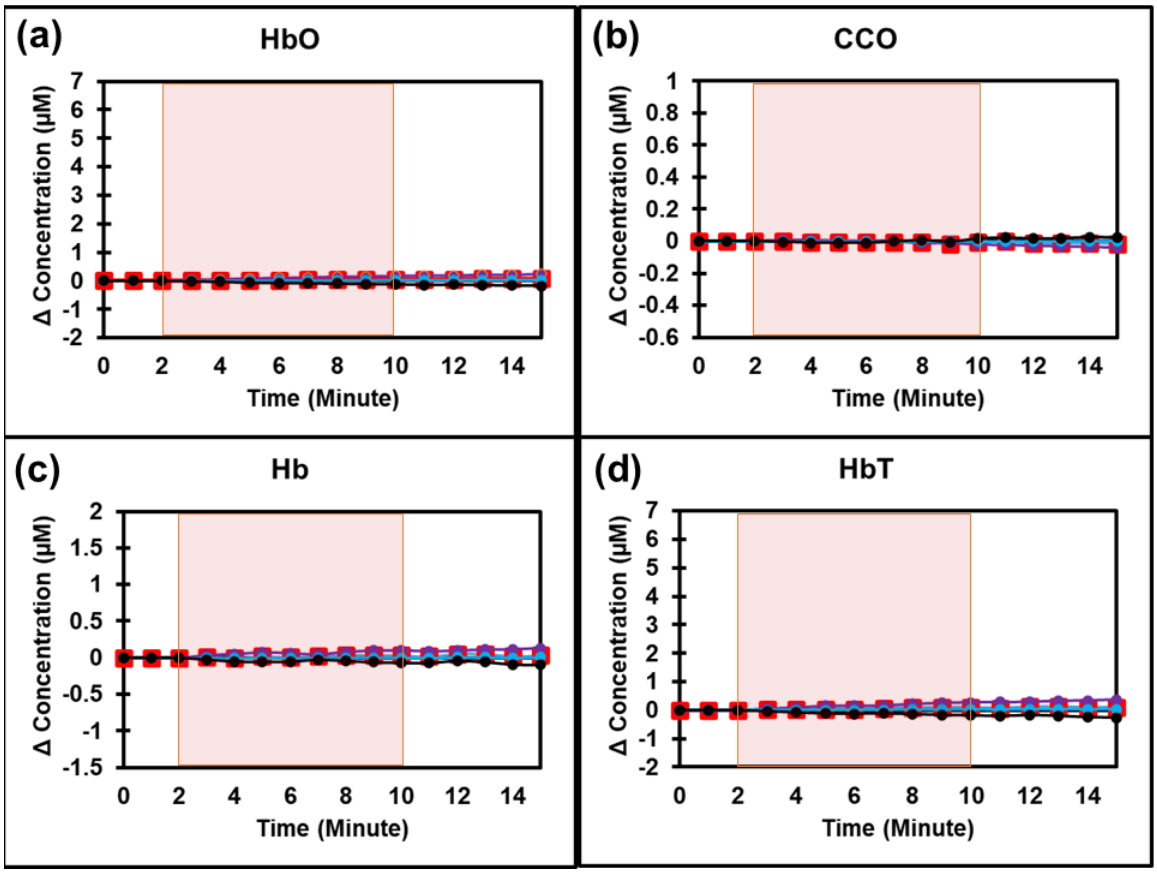

Figure 29 Protocol group-wise averaged data for sham (black), 808-nm (blue), 852-nm (purple), and 1064-nm (red). Stimulation epoch is indicated with red shading while post-stimulation epoch remains unshaded. Lines displayed are the change in the concentration of the chromophores of [HbO] (a), [CCO] (b), [Hb] (c), and [HbT] (d).